TIMING AND FREQUENCY SYNCHRONIZATION FOR ORTHOGONAL FREQUENCY DIVISION MULTIPLE-ACCESS SYSTEMS

A Thesis
Presented to
The Academic Faculty

by

Malik M. U. Gul

In Partial Fulfillment
of the Requirements for the Degree
Doctor of Philosophy in the
School of Electrical and Computer Engineering

Georgia Institute of Technology
August 2014

TIMING AND FREQUENCY SYNCHRONIZATION FOR ORTHOGONAL FREQUENCY DIVISION MULTIPLE-ACCESS SYSTEMS

Approved by:

Professor Xiaoli Ma, Advisor
School of Electrical and Computer Engineering
Georgia Institute of Technology

Professor Gee-Kung Chang
School of Electrical and Computer Engineering
Georgia Institute of Technology

Professor Edward Coyle
School of Electrical and Computer Engineering
Georgia Institute of Technology

Dr. Brett Walkenhorst
Systems Technology and Analysis Division
Georgia Tech Research Institute

Professor David Goldsman
School of Industrial and Systems Engineering
Georgia Institute of Technology

Date Approved: 25 June 2014

To my family,

ACKNOWLEDGEMENTS

I thank Almighty for giving me the health and the perseverance to carry out my doctoral studies at Georgia Tech. Besides, there are a number of people I am indebted to, who have played a significant role in my success. Specially, I would like to thank my advisor Prof. Xiaoli Ma for her continuous support and guidance throughout my research work. She will be a role model for me throughout my life in a number of aspects including the ways to effectively conduct and publish my research. I would also like to thank Dr. Sungeun Lee who advised me as a post-doctoral researcher for a better part of my stay in Georgia Tech. He was always very eager to help, and his useful insights and suggestions have really improved the quality of my work. My stay as an intern during summers of 2011 and 2012 in National Instruments has played a significant part in shaping and guiding my dissertation and research statement, for which I am indebted to the team of RF communications group at National Instruments. In particular, I would like to thank my mentor Ahsan Aziz whose continuous support and encouragement have always been by my side. Also, I would like to thank Yong Rao whose expertise have really helped me achieve my goals in rapid prototyping of my research work, and his insightful explanations have taught me a great deal. I would like to thank my committee members Prof. Gee-Kung Chang, Prof. Edward Coyle, Prof. David Goldsman, and Dr. Brett Walkenhorst for serving on my committee and providing useful comments to improve my work.

I would like to acknowledge the financial support provided by United States Educational Foundation in Pakistan (USEFP) and Higher Education Commission (HEC) of Pakistan as part of the Fulbright scholarship. I would also like to thank National Instruments for their equipment donations, which have enabled prototyping of my

research work.

I would also like to thank all my group members and collaborators in Georgia Tech for their support. Apart from my research group, I have enjoyed the company of some wonderful friends during my stay at Georgia Tech, which really made all these years very pleasant and memorable. Among all friends and colleagues, I would specially like to mention Faisal Kakar, Samiullah Kashif, and Amal Ekbal. I would not have met these wonderful persons if I was not a graduate student at Georgia Tech. I am also lucky that I have friends like Abdul Rahman, Shafiq-ur-Rahman, and Fahd Khan who have a great influence in my decision of pursuing doctoral studies. I would also like to thank Mr. Muhammad Azam from Renzym whose guidance, perseverance, and personality I will always admire.

In the end, I would like to thank my family including my parents, my wife, and my children. I have no doubt that my mother's prayers have the most important role for my health and success throughout my life. My wife has been very helpful and supportive throughout my Ph.D. studies. She has played a significant role in the upbringing of our children while I have been busy in my work. I would like to thank my princesses, my daughters Umber and Aemen, who are a source of sheer bliss.

TABLE OF CONTENTS

LIST OF TABLES

LIST OF FIGURES

LIST OF SYMBOLS OR ABBREVIATIONS

AP Access-Point.

API Applications Programming Interface.

AWGN Additive White Gaussian Noise.

BER Bit Error Rate.

BS Base-Station.

BW Bandwidth.

CAZAC Constant Amplitude Zero Autocorrelation.

CFO Carrier Frequency Offset.

CIR Channel Impulse Response.

CoMP Coordinated Multi-Point.

CP Cyclic-Prefix.

DFT Discrete Fourier Transform.

DL Downlink.

ESPRIT Estimation of Signal Parameters via Rotational Invariance Technique.

EVM Error Vector Magnitude.

FFT Fast Fourier Transform.

FPGA Field Programmable Gate Array.

GSAS Generalized Sub-carrier Allocation Scheme.

IBI Inter-Basestation Interference.

ICI Inter-Carrier Interference.

IDFT Inverse Discrete Fourier Transform.

IEEE Institute of Electrical and Electronics Engineers.

IIC Iterative Interference Cancelation.

ISAS Interleaved Sub-carrier Allocation Scheme.

ISI Inter-Symbol Interference.

LNS Left Null Space.

LS Least Squares.

LTE Long Term Evolution.

MMSE Minimum Mean Square Error.

MSE Mean Square Error.

MU Mobile User.

MUI Multi-User Interference.

MUSIC MUltiple SIgnal Classification.

NI National Instruments.

NP Neyman-Pearson.

OFDM Orthogonal Frequency Division Multiplexing.

OFDMA Orthogonal Frequency Division Multiple-Access.

PAPR Peak-to-Average Power Ratio.

PARAFAC PARAllel FACtor.

PCI Peripheral Component Interconnect.

PDP Power Delay Profile.

PSS Primary Synchronization Signal.

PXI PCI eXtensions for Instrumentation.

QAM Quadrature Amplitude Modulation.

QPSK Quadrature Phase Shift Keying.

RF Radio Frequency.

Rx Receiver.

SC-FDMA Single Carrier Frequency Division Multiple-Access.

SFBC Space Frequency Block Coding.

SI Self Interference.

SNR Signal-to-Noise Ratio.

SSAS Sub-band Sub-carrier Allocation Scheme.

TO Timing Offset.

Tx Transmitter.

UL Uplink.

WiMAX Worldwide Interoperability for Microwave Access.

WLAN Wireless Local Area Network.

ZC Zadoff-Chu.

SUMMARY

Orthogonal Frequency Division Multiplexing (OFDM) is an efficient multi-carrier transmission scheme, which is prevalent in numerous wireless communication system nowadays. The widespread usage of OFDM can be attributed to its following two advantages over single-carrier transmissions schemes: (i) As the bandwidth of communication systems is increasing steadily to satisfy the explosive growth in mobile data traffic, the wireless channel is becoming increasingly frequency selective. OFDM transforms a frequency selective channel into a flat fading channel enabling low-complexity channel equalization. (ii) The orthogonal nature of the sub-carriers in OFDM provides means for efficient resource management as the bandwidth resources in the time-frequency grid can be flexibly allocated to different users based on their channel conditions and bandwidth requirements. These advantages have led to the use of OFDM in all major broad-band communications systems including IEEE 802.11 wireless local area networks (WLAN), IEEE 802.16 worldwide interoperability for microwave access (WiMAX), long term evolution (LTE)-Advanced, and digital video broadcasting standards.

However, achieving reliable timing and frequency synchronization is one of the major challenges in implementation of an OFDM system. Timing synchronization deals with the estimation of the starting index of the received symbols, and improper timing synchronization leads to inter-symbol interference (ISI) due to multipath channel, which degrades the system performance. However, the presence of cyclic-prefix relaxes the sensitivity of OFDM systems to timing synchronization erros, as compared to single-carrier schemes. Frequency synchronization deals with the estimation and the

compensation of carrier frequency offsets (CFO). As the transmitter (Tx) and the receiver (Rx) use independent local oscillators for frequency modulation/demodulation, CFO can exist between the Tx-Rx pair. Also, the mobility of users in a wireless systems can lead to Doppler spread, which introduces CFO. OFDM systems are much more sensitive to CFOs as compared to single-carrier schemes as CFOs invalidate the orthogonality of OFDM sub-carriers introducing inter-carrier interference (ICI), which severely compromises the overall system performance.

This dissertation presents the design, analysis, and implementation of timing and frequency synchronization schemes for various scenarios in downlink (DL) and uplink (UL) OFDM transmissions. DL refers to the transmission from the base-station (BS) or access-point (AP)to the mobile users (MU), and DL synchronization is required whenever an MU tries to connect to the BS. Recently, cooperative DL transmissions have also gained attention for mitigation of co-channel interference in cellular systems. In cooperative DL transmissions, also termed as coordinated multi-point (CoMP) transmissions, several BSs transmit simultaneously to the MUs while sharing frequency resources, and estimation of synchronization parameters corresponding to multiple BSs is required to avoid inter-BS interference and enable DL CoMP transmissions. We have developed training-assisted BS detection, timing, and frequency synchronization schemes for both conventional and cooperative DL OFDM transmissions. The proposed schemes involve the design of training signals as well as the synchronization algorithms, which simplify the overall DL synchronization architecture making it conducive for hardware implementation. We have also implemented the proposed algorithms in hardware to perform real-time performance measurements.

In UL transmissions, multiple MUs transmit simultaneously to the BS, where each MU transmits on its allocated sub-carriers. Sub-carrier allocations schemes can be classified into three different types: grouped, interleaved and generalized sub-carrier allocation. As the received signal at the BS is the sum of all active MUs' signals,

and different MUs have independent CFOs, UL transmissions suffer from multi-user interference (MUI) in addition to ICI making UL transmissions even more sensitive to CFOs. Thus, UL frequency synchronization entails estimation and compensation of CFO at the BS corresponding to each MU. We have developed two frequency synchronization schemes for UL OFDM transmissions. A null sub-carrier-based frequency synchronization algorithm has been devised, which supports both sub-band and generalized sub-carrier allocations. Also, a low-complexity semi-blind CFO estimation and compensation scheme has been proposed for interleaved sub-carrier allocation using the parallel factor analysis method.

The proposed techniques enable efficient and reliable timing and frequency synchronization for DL and UL OFDM transmissions.

CHAPTER I

INTRODUCTION

Orthogonal frequency division multiplexing (OFDM) [60] is a multi-carrier transmission technique, which is the core technology used in numerous wireless communication systems nowadays. Examples include IEEE 802.11 wireless local area networks (WLAN) [1], IEEE 802.16m worldwide interoperability for microwave access (WiMAX) [2], long term evolution (LTE) [40], and digital video broadcasting [62]. Compared to the single-carrier transmission techniques, OFDM offers a number of advantages, specially for broad-band communications. For example, efficient resource allocation is realized by the orthogonal nature of OFDM sub-carriers as resources in the time-frequency grid can be flexibly allocated to different users based on the requested bandwidth and channel conditions. Moreover, one-tap channel equalization in OFDM reduces the complexity of broad-band transmissions as compared to single-carrier schemes.

OFDM is employed in both downlink (DL) and uplink (UL) transmissions supporting data, voice, and multi-media applications. In DL transmissions, a base-station (BS) or an access-point (AP) transmits signals to multiple mobile users (MU) in its operation region or the cell, while in UL transmissions, multiple MUs transmit simultaneously to a BS using exclusive sub-carriers. Multi-user UL OFDM transmissions are often referred as orthogonal frequency division multiple-access (OFDMA) transmissions [51]. Different sub-carrier allocation strategies have been proposed in the literature for OFDMA UL transmissions like sub-band, interleaved and generalized allocation [51]. In sub-band sub-carrier allocation scheme (SSAS), each user is allocated a group or sub-band of adjacent sub-carriers, while in interleaved sub-carrier

allocation scheme (ISAS), the sub-carriers of different users are interleaved into each other. The generalized sub-carrier allocations scheme (GSAS) is a hybrid of SSAS and ISAS as each user is allocated several small sub-bands, also called tiles. The BS controls the sub-carrier allocation to the MUs based on the requested bandwidth and the channel conditions.

However, a major challenge in an OFDM system is to achieve reliable timing and frequency synchronization at the receiver (denoted as Rx; an MU in DL transmissions or a BS in UL transmissions) as synchronization errors can result in inter-symbol-interference (ISI) and inter-carrier-interference (ICI) in the received signal, which severely degrade system performance [72]. Synchronization in OFDM systems is a two-fold process. Timing synchronization deals with the estimation of timing-offsets (TO) caused by random propagation delays and/or a sampling frequency mismatch between the transmitter (denoted as Tx) and the Rx. In addition, frequency synchronization deals with the estimation and the compensation of carrier frequency offset (CFO) caused by the Doppler effect and/or an oscillator mismatch between the Tx and the Rx. Both timing and frequency synchronization are usually performed in two phases: coarse and fine [49]. Coarse timing synchronization generates an initial estimate of the starting index of the OFDM symbol, while fine timing improves the estimate to a difference of a few samples from the ideal starting point. Similarly, coarse frequency synchronization generates a rough CFO estimate, while fine frequency synchronization deals with the estimation of the residual CFO. We discuss the challenges and requirements of DL and UL synchronization in the following sections.

1.1 Downlink Synchronization

In cellular communications, synchronization begins on the DL, when a MU starts up and tries to synchronizes itself to a BS, or when a MU hands-off from one BS to another BS. As the MU has no prior synchronization information, CFOs on the

DL can be large. In particular, CFOs that are fractional or integer multiples of the sub-carrier spacing can be expected. For example, in LTE, which uses OFDM with sub-carrier spacing of 15 kHz, an MU with a clock accuracy of ± 10 ppm (parts per million) can experience a maximum CFO of ± 20 kHz (1.33 sub-carrier spacings) at 2 GHz carrier frequency. Thus, for DL coarse frequency synchronization, the MU must be able to estimate and compensate integer CFOs.

As DL timing synchronization usually precedes frequency synchronization, timing synchronization should also be robust to integer CFOs. To enable low-complexity channel equalization and simplify timing synchronization, a cyclic prefix (CP) is appended in the beginning of each OFDM symbol [85]. As CP is always longer than the maximum excess delay of the channel, some samples towards the end of CP are free of ISI, and it is sufficient to estimate the start of the OFDM symbol within the ISI-free sample region [72].

Although a BS transmits to multiple MUs in DL transmissions, each MU performs synchronization individually. Thus, conventional DL synchronization can be thought of as the synchronization in single-user or point-to-point OFDM links. However, this assumption may not be true in cooperative OFDM systems. As full frequency reuse is employed nowadays to maximize the capacity of cellular networks, it leads to strong co-channel interference at the cell-edges, which limits the performance of cellular networks. In order to minimize the co-channel interference, various BS cooperation techniques have been proposed. An example of such techniques is coordinated multi-point (CoMP) transmission [48], which is a part of LTE-Advanced standard [41]. In CoMP, simultaneous transmissions from multiple BSs over same sub-carriers are employed to serve multiple MUs at the cell-edge to mitigate co-channel interference [48]. As the received signal at the MU is the sum of multiple BSs' signals, synchronization in DL CoMP transmissions is no longer equivalent to conventional DL synchronization. In terms of timing synchronization, the difference in time of arrival of BSs'

signals at the MU should be less than the length of the ISI-free region to avoid inter-BS interference (IBI). This requirement indirectly defines the geographical radius of CoMP transmissions [34]. As each BS uses its own local oscillator, CFOs between BSs lead to IBI, which degrades system performance. Thus, frequency synchronization for DL CoMP transmissions involves estimation and compensation of the CFO corresponding to each BS from the composite received signal at the MU.

1.2 Uplink Synchronization

UL transmissions initiate after DL synchronization. As the MU already estimates the CFO between itself and the BS in DL synchronization, CFOs on the UL are only caused by residual synchronization errors and/or Doppler spread. However, the contribution of Doppler frequency to the CFO is usually very small. As an example, a MU moving with a speed of 100 Km/hr can result in a maximum Doppler frequency of about 185 Hz at 2 GHz carrier frequency, which is only 1.2% of the sub-carrier spacing in LTE. Thus, it is safe to assume that the UL CFOs are only a fraction of the sub-carrier spacing [51]. However, in UL transmissions, multiple MUs transmit simultaneously to the BS using their allocated sub-carriers, and each MU has an independent CFO. The signal received at the BS is the sum of the signals transmitted by all the users, and multiple CFOs introduce multi-user-interference (MUI) in addition to the ICI. Thus, UL CFO estimation is a multi-parameter estimation problem as the BS needs to estimate the CFO of each MU from the composite received signal. As MUs transmit on exclusive sub-carriers, UL CFO estimation is different than CFO estimation for DL CoMP transmissions where BSs share the sub-carriers. As OFDMA allows different sub-carrier allocations schemes outlined in the beginning of this Chapter, the CFO estimation algorithm must support the corresponding sub-carrier allocation scheme.

The presence of the CP in the OFDM symbol can help in UL timing synchronization. If the length of the CP is greater than the round-trip delay, i.e., the time when the BS transmits the signal to the time when it receives the signals from all MUs, the TOs of the MUs can be incorporated in their effective channels [51]. Such a system is termed as quasi-synchronous system [51]. In quasi-synchronous systems, all MUs' signals arrive within the ISI-free region, and MUI due to timing a-synchronicity can be avoided. Once, the BS estimates the TOs of all MUs, it feedbacks this information to the corresponding MUs. The MUs can advance their timing based on the feedback from the BS, and the length of CP for the following symbols can be shortened to improve the spectral efficiency.

Apart from synchronization, high peak-to-average-power ratio (PAPR) is another concern in OFDM systems. High PAPR forces the power amplifier at the Tx to operate with a back-off, reducing the energy efficiency of the system. Energy efficiency is a major concern in UL transmissions for battery-operated MUs due to limited power resources. To resolve the high PAPR issue, a variant of OFDMA termed as single-carrier frequency division multiple-access (SC-FDMA) has been proposed [54], which employs extra discrete Fourier transform (DFT) precoding at the Tx to reduce the PAPR of the transmitted signal. Having the advantage of lower PAPR, SC-FDMA is employed in LTE UL transmissions as opposed to OFDMA [40]. However, the reduction in PAPR is also influenced by the choice of sub-carrier allocation scheme in UL transmissions [53]. Among the three sub-carrier allocation schemes described above, ISAS provides the lowest PAPR [53], which motivates the use of ISAS in SC-FDMA UL transmissions. However, being a variant of OFDMA, SC-FDMA transmissions are also sensitive to CFOs and require frequency synchronization at the BS. Although ISAS provides lowest PAPR, it is most sensitive to CFOs as the interleaved sub-carriers of different MUs generate more MUI for non-zero CFOs, compared to SSAS or GSAS.

1.3 Thesis Contributions

Motivated by the sensitivity of OFDM to synchronization impairments, in this thesis, we have developed, analyzed, and implemented timing and frequency synchronization techniques for various scenarios in both DL and UL OFDM transmissions. Important contributions of this thesis are enlisted below:

- Timing and frequency synchronization algorithms have been developed for DL OFDM transmissions. The proposed timing synchronization is robust to integer CFOs, while both timing and frequency synchronization schemes require similar hardware architecture, resulting in efficient hardware implementation.

- Frequency synchronization algorithm has been developed for DL CoMP transmissions, which can decouple different BSs and estimate multiple CFOs corresponding to different BSs from the composite received signal at the MU.

- A CFO estimation algorithm has been developed for UL OFDMA transmissions, which supports sub-band and generalized sub-carrier allocations schemes. The uniqueness of the CFO estimation has been proved along with the acquisition range.

- CFO estimation and compensation algorithms for UL SC-FDMA transmissions with interleaved sub-carrier allocation have been developed.

- A hardware testbed has been implemented to carryout real-time performance evaluation of the proposed synchronization algorithms.

1.4 Thesis Organization

The rest of the dissertation is organized as follows. In Chapter 2, a background of timing and frequency synchronization in OFDM systems is provided along with a literature survey of the existing algorithms and the contributions of our research

work. Chapter 3 presents a symbol detection, timing and frequency synchronization scheme for DL OFDM transmissions using training symbols. The design of the training symbols along with the performance evaluation of the proposed algorithms is presented in detail. A frequency synchronization scheme for multiple CFO estimation in DL CoMP transmissions is presented in Chapter 4 along with its hardware implementation and results of real-time performance measurements. Dealing with UL transmissions, Chapter 5 presents a frequency synchronization algorithm for OFDMA transmissions supporting SSAS and GSAS, while Chapter 6 presents a CFO estimation and compensation algorithm for SC-FDMA transmissions with ISAS. Chapter 7 provides the conclusions of this dissertation along with potential future research directions.

Notations Lower case boldface letters represent column vectors containing entries in time domain, while upper case boldface letters represent matrices or column vectors containing entries in frequency domain, depending on the context. $(\cdot)^H$ represents Hermitian and $(\cdot)^T$ represents transpose. $\mathbf{D}_N(\mathbf{h})$ with a vector argument represents an $N \times N$ diagonal matrix with vector $\boldsymbol{h}$ containing the diagonal entries. $\mathbf{D}_N(f)$ with a scalar argument represents an $N \times N$ diagonal matrix with $[\mathbf{D}_N(f)]_{nn} = e^{j\frac{2\pi}{N}fn}$ and $j = \sqrt{-1}$. $\mathbf{I}_N$ represents an $N \times N$ identity matrix, $\mathbf{0}_N$ denotes an $N \times 1$ zero vector, and $\mathbf{F}_N$ represents an $N \times N$ unitary Discrete Fourier Transform (DFT) matrix . We define $\mathbf{f}_N(f)$ as the $N \times 1$ normalized Fourier vector given as $\mathbf{f}_N(i) = N^{-1/2}[1, e^{j\frac{2\pi}{N}i}, e^{j\frac{2\pi}{N}2i}, \ldots, e^{j\frac{2\pi}{N}(N-1)i}]^T$. ϕ denotes the empty set, $\bigcup$ denotes the union, $\bigcap$ denotes the intersection, and $\setminus$ denotes the relative complement of sets. $|\cdot|$ represents the cardinality of a set, and $E[\cdot]$ represents the expected value. $(\cdot)_N$ represents the modulo-N operation. 'MU' or simply 'user' are used interchangeably in the dissertation.

CHAPTER II

BACKGROUND

As the objective of this dissertation is to develop timing and frequency synchronization techniques for DL and UL OFDM transmissions, this chapter presents the background of synchronization in OFDM systems including the system model and the effect of synchronization impairments on OFDM transmissions. In addition, a literature survey of the existing approaches for synchronization is provided along with the details of the important contributions of the dissertation.

2.1 Synchronization in DL OFDM Transmissions

In this section, we provide the system model and signal description of DL OFDM transmissions along with the role of timing and frequency synchronization.

2.1.1 System Model and Signal Description

We consider a base-band equivalent model of an OFDM system with the block diagram shown in Figure 1. Total number of sub-carriers in each OFDM symbol are denoted as N while the number of non-zero sub-carriers are denoted as $R \leq N$. The rest of the sub-carriers are zero or null sub-carriers comprising the guard band. The indices of modulated sub-carriers are collected in a set denoted as $\mathcal{I}$ with $|\mathcal{I}| = R$. The information bit stream at the transmitter is mapped to constellation symbols based on the modulation scheme employed in the system. The constellation symbols are then mapped to the R non-zero sub-carriers. The sub-carrier mapping operation can be expressed in matrix form as

$$\mathbf{X} = \mathbf{TS}, \tag{1}$$

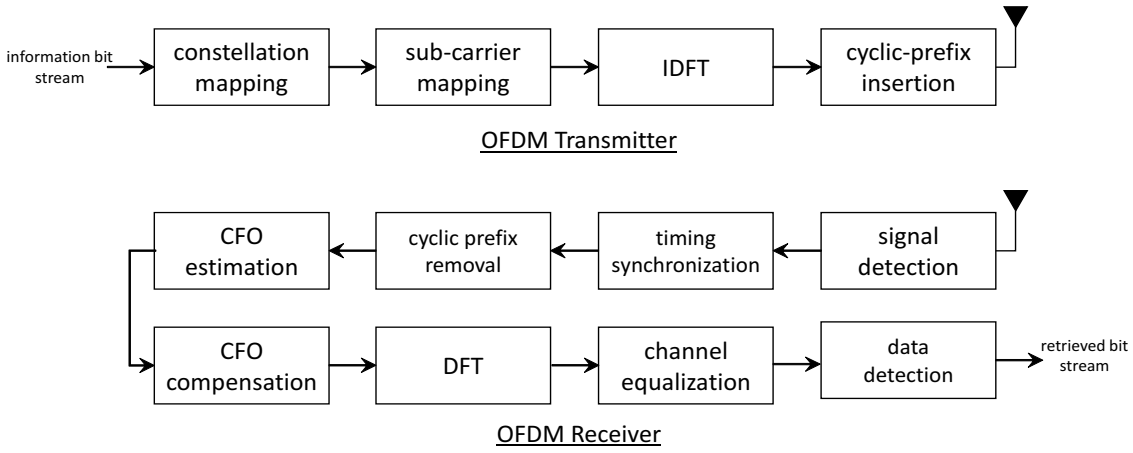

Figure 1: Block diagram of an OFDM system.

where $\mathbf{S}$ is the $R \times 1$ vector containing the constellation symbols, $\mathbf{T}$ is the $N \times R$ sub-carrier mapping matrix given as $\mathbf{T} = \left[\mathbf{e}_{x_0}, \mathbf{e}_{x_1}, \ldots, \mathbf{e}_{x_{R-1}}\right]$, where $\mathbf{e}_x$ is the x^{th} column of the $N \times N$ identity matrix, and $x_r \in \mathcal{I}, 0 \leq r \leq R-1$. $\mathbf{X}$ is the $N \times 1$ vector containing the constellation symbols on the specified sub-carriers. An N point inverse discrete Fourier transform (IDFT) of $\mathbf{X}$ is performed to modulate the sub-carriers and generate the OFDM symbol in time domain given as

$$\mathbf{x} = \mathbf{F}_N^H \mathbf{X}. \tag{2}$$

A CP of N_g samples is then appended in the beginning of each OFDM symbol, which is a repetition of the last N_g samples of $\mathbf{x}$.

The received signal is sampled at a sampling frequency of $F_\mathrm{s} = N\Delta f$, where Δf is the sub-carrier spacing. Assuming that the CFO between the Tx and the Rx is f_H Hz, and the signal is received with a TO of d samples as shown in Figure 2, the n^{th} sample of the received OFDM symbol can be expressed as

$$y[n] = e^{j\frac{2\pi}{N}fn} \sum_{p=0}^{P-1} h[p]x[n-d-p] + w[n], \tag{3}$$

where $f = \frac{f_H}{\Delta f}$ is the CFO normalized by sub-carrier spacing, d is the TO in units of sample period ($\frac{1}{F_\mathrm{s}}$), $h[p]$ $0 \leq p \leq P-1$ is the base-band equivalent channel impulse

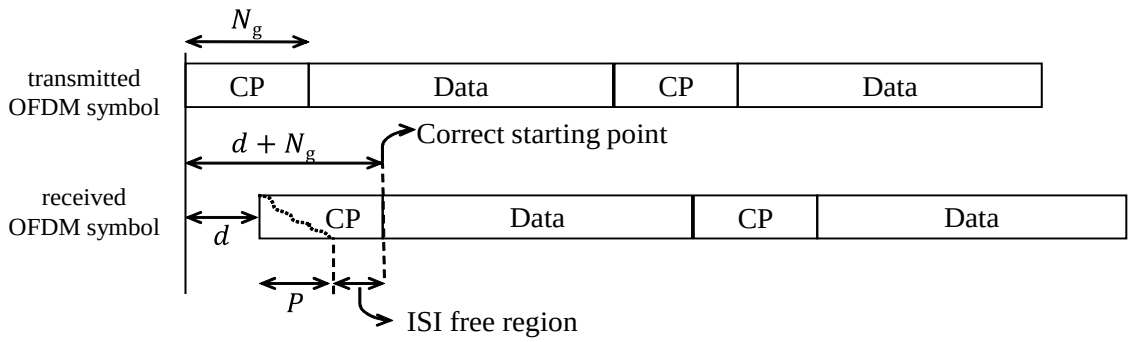

Figure 2: Received OFDM symbol with a timing offset of d samples showing the ISI-free region.

response (CIR) with P taps where $P < N_g$, and $w[n]$ represents the n^{th} additive white Gaussian noise (AWGN) sample.

2.1.2 Effect of Timing and Carrier Frequency Offsets

In this section, we discuss the effect of synchronization impairment on the decoding of the received OFDM symbols. The multipath channel $h[p]$ introduces ISI in the received OFDM symbol in (3). As $N_g > P$, the CP absorbs the ISI in the current received OFDM symbol from the previous symbol, and the last $N_g - P$ samples of the CP of the received OFDM symbol are ISI-free as shown in Figure 2. If the receiver can estimate the start of the OFDM symbol within the ISI-free region, the ISI can be avoided. Moreover, as the CP makes the OFDM symbol repetitive, a TO estimate within the ISI-free region also transforms the linear convolution of the OFDM symbol with the multipath channel in (3) into circular convolution, which enables low-complexity channel equalization [85]. Thus, to perform CP removal, DFT, and correspondingly the decoding of the received OFDM symbol as shown in Figure 1, the receiver must estimate the TO d in (3). Failure to estimate the TO or starting index within the ISI-free region results in ISI and ICI in the received OFDM symbol, which severely degrade the system performance [72].

After TO estimation and CP removal, the received OFDM symbol can be expressed as [85],

$$\mathbf{y} = e^{j\frac{2\pi}{N}fN_g}\mathbf{D}_N(f)\mathbf{F}_N^H\mathbf{D}_N(\mathbf{H})\mathbf{X} + \mathbf{w}, \tag{4}$$

where $\mathbf{y}$ is an $N \times 1$ vector containing the samples of the received OFDM symbol after CP removal, and $\mathbf{H}$ is an $N \times 1$ vector containing an N point DFT of the CIR. If there is no CFO, i.e., $f = 0$, $\mathbf{D}_N(0) = \mathbf{I}$ in (4), and an N point DFT of the received OFDM symbol in (4) results in

$$\begin{aligned}\mathbf{Y} &= \mathbf{F}_N\mathbf{D}_N(0)\mathbf{F}_N^H\mathbf{D}_N(\mathbf{H})\mathbf{X} + \mathbf{F}_N\mathbf{w}, \\ &= \mathbf{D}_N(\mathbf{H})\mathbf{X} + \mathbf{W}, \ f = 0,\end{aligned} \tag{5}$$

where $\mathbf{W} = \mathbf{F}_N\mathbf{w}$. Eq. (5) shows that the sub-carriers of the received OFDM symbol remain orthogonal if CFO is zero, and the multipath channel in time domain is transformed to a one-tap channel for each sub-carrier in frequency domain, which enables low-complexity channel equalization. However, if f is non-zero, $\mathbf{F}\mathbf{D}_N(f)\mathbf{F}^H$ is not an identity matrix, which leads to interference between the sub-carriers of the received OFDM symbols, termed as the ICI. Without CFO estimation and compensation, the ICI in the received OFDM symbol severely degrades the system performance as it violates the orthogonality of the OFDM system. Thus, frequency synchronization, comprising CFO estimation and compensation, must be performed before decoding the OFDM symbol.

2.1.3 Literature Review of Synchronization Techniques for DL OFDM Transmissions

Timing and frequency synchronization schemes proposed in the literature for DL OFDM transmissions can be broadly classified into two types: data-aided or training-assisted schemes [3, 19, 27, 49, 50, 52, 57, 63, 67, 69, 72, 76, 81, 82, 87] and non-data-aided or blind schemes [10, 42–44, 58, 77, 79, 88]. Data-aided or training-assisted schemes

use specially designed training symbols or pilot sub-carriers for timing and frequency synchronization, while non-data-aided or blind schemes use inherent structure of the OFDM symbol [10,44,58,79], its statistical characteristics [42,88] or null sub-carriers for synchronization [43,77]. However, for satisfactory performance, non-data-aided algorithms usually require a large number of OFDM symbols.

Data-aided synchronization schemes employ either the auto-correlation of the received training symbol or its cross-correlation with the local copy at the receiver. Auto-correlation-based methods for timing synchronization [49,57,67,69] use training symbols with repetitions that offer robustness to large CFO and multi-path channel. Therefore, these methods are suitable for coarse DL TO and CFO estimation as DL timing synchronization must be robust to integer CFOs as mentioned in Section 1.1. In the absence of CFO, cross-correlation-based methods [76,81,82] offer better timing synchronization performance and lower probabilities of miss and false alarm. However, in the presence of integer CFOs, the performance of these methods degrades severely, which limits their use to fine timing estimation schemes as in [19,76,81,87]. Thus, the schemes employed for DL synchronization in OFDM systems usually employ auto-correlation-based algorithms for coarse timing and frequency synchronization in order to obtain robustness to large CFOs, and cross-correlation-based algorithms for fine timing estimation to improve the timing estimation performance. However, the use of both auto-correlation and cross-correlation-based algorithms increases the overall complexity of the hardware architecture. Hence, it is desirable to investigate only cross-correlation-based coarse and fine timing synchronization schemes, which are robust to integer CFOs.

To facilitate synchronization and cell search procedures in LTE DL and UL, Zadoff-Chu (ZC) sequences [16] have been proposed as training symbols [40]. ZC sequences are part of the family of constant-amplitude zero auto-correlation (CAZAC) sequences in which circularly shifted copies of a sequence are uncorrelated [16]. ZC

sequences are used in LTE downlink for cell-search and DL synchronization. Recently, joint fine timing and channel estimation using ZC or general CAZAC sequences have been proposed for DL transmissions in [81, 82]. The algorithm uses a ZC sequence as a training symbol and shows that the cross-correlation with the received ZC sequence generates an estimate of the CIR that is further used to estimate fine timing of the OFDM symbol. However, the critical problems of CFO estimation and coarse timing synchronization in the presence of CFOs have not been addressed. Instead, following the same architecture for DL synchronization as mentioned before, the algorithm resorts to auto-correlation-based scheme [67] for coarse timing and CFO estimation that increases the complexity of the overall synchronization procedure.

As part of our research on DL synchronization, our objective was to develop a cross-correlation-based synchronization scheme, which offers robustness to CFOs and better synchronization performance. The proposed solution is a training-based timing and frequency synchronization algorithm. The training symbol is based on ZC sequences, and we have proposed the criterion to select appropriate parameters of the ZC sequence to achieve robustness to CFOs. Using the proposed training symbol, we have then designed training signal detection, timing, and frequency synchronization algorithms. The details can be found in Chapter 3 and [24]. With our proposed synchronization schemes combined with [81,82], a single cross-correlation-based hardware architecture can be used for detection of training signal and estimation of coarse TO, fine TO, integer CFO, and multi-path channel resulting in a significant reduction in hardware resource usage for practical implementations.

2.1.4 Synchronization in DL CoMP OFDM transmissions

As mentioned in Section 1.1, in DL CoMP OFDM transmissions, multiple BSs transmit simultaneously to the MUs, and the challenge is to estimate the TO and CFO corresponding to each BS at the MU. Conventional synchronization schemes for DL

OFDM transmissions discussed in Section 2.1.3 cannot be employed in this scenario as BSs share time as well as frequency (sub-carriers) resources. Hence, novel frequency synchronization schemes must be devised for DL CoMP OFDM transmissions.

2.1.5 System Model for DL CoMP OFDM Transmissions

The total number of BSs in the CoMP transmissions is denoted as B, and the parameters corresponding to the b^{th} BS are denoted with a sub-script b, $0 \leq b \leq B-1$. Thus, the multi-path channel between the b^{th} BS and the MU is denoted as $\tilde{h}_b[p]$ for $0 \leq p \leq P_b - 1$, where P_b is the number of taps of the channel. Assuming all B BSs' signals are received within the ISI-free region, the timing offset of b^{th} base-station (denoted as d_b) relative to the earliest BS (assumed to be $b = 0$ with $d_0 = 0$ without loss of generality) can be incorporated in its CIR. Therefore, the effective CIR between the b^{th} BS and the MU is given as

$$h_b[p] = \begin{cases} 0 & 0 \leq p \leq d_b - 1, \\ \tilde{h}_b[p - d_b] & d_b \leq p \leq P_b + d_b - 1, \\ 0 & P_b + d_b \leq p \leq P - 1, \end{cases} \tag{6}$$

where $P = \max_b\{P_b + d_b\}$ is the effective maximum excess delay of the CoMP channel. We assume that the length of the CP satisfies $N_{\mathrm{g}} > P$. The received signal at the MU is modified from the single BS case in (3) to

$$y[n] = \sum_{b=0}^{B-1} e^{j\frac{2\pi}{N} f_b n} \sum_{p=0}^{P-1} h_b[p] x_b[n-p] + w[n], \tag{7}$$

where f_b is the CFO between the b^{th} BS and the MU. We assume that $|f_b| \leq 0.5\ \forall b$. It is a reasonable assumption for DL CoMP transmissions since a MU must be synchronized to a serving BS prior to entering in the CoMP mode, which implies that the MU will have already estimated the CFO corresponding to the serving BS. Thus, CFO estimation for CoMP transmissions is the estimation of CFO between BSs. As the BS clock accuracy is usually much higher than the MU clock accuracy, the CFO

between the BSs is usually very small. For example, a typical BS clock accuracy in LTE varies from $50-250$ parts per billion (ppb) [9], which implies a maximum CFO of 1 kHz between any two BSs at 2 GHz carrier frequency. As the sub-carrier spacing in LTE is 15 kHz, it implies that $|f_b| < 0.07 < 0.5$. Thus for practical systems, it can be safely assumed that each CFO f_b is only a fraction of the sub-carrier spacing. However, the CFO of each BS is independent and thus, CFO estimation corresponding to each BS must be carried out to combat IBI and ICI. If the MU can somehow decouple different BSs' signals, CFO estimation for each BS can be performed separately.

2.1.6 Literature Review of Synchronization Techniques for DL CoMP OFDM Transmissions

Frequency synchronization for CoMP transmissions is a relatively new research area and few contributions exist in the literature including [4, 8, 39, 75, 90, 91]. Time orthogonal sequences are proposed in [4] to decouple different BSs and simplify the CFO estimation scheme at the cost of reduced spectral efficiency. Joint Maximum likelihood (ML) CFO estimation has been proposed in [90]. However, the complexity of the proposed algorithm is too high for practical implementations. Iterative CFO estimation method has been proposed in [39] using mutually orthogonal signals with a low-complexity CFO estimation scheme using first-order Taylor expansion. In [75], time-domain ZC sequences [16] are employed for CoMP CFO estimation. Each BS transmits a training symbol containing a ZC sequence with different circular shift, and simplified ML CFO estimation combined with iterative interference cancelation (IIC) is proposed. A criterion for selection of ZC sequence parameters and circular shifts is also presented, termed as the robust orthogonal sequences (ROSE) [75]. However, the method requires several iterations of IIC along with line search for each BS in each iteration, increasing the complexity of CFO estimation. Moreover, the ROSE selection criterion is only for time domain ZC sequences, which may not be applicable to certain OFDM systems, e.g., LTE DL [40], where only a subset of total

sub-carriers is modulated to satisfy certain bandwidth constraints.

We have designed training signals and associated frequency synchronization scheme for DL CoMP OFDM transmissions using ZC sequences. The training signals are designed to allow decoupling of BSs' information at the MU. The proposed training signal design criterion is applicable to ZC sequences defined either in time or frequency (sub-carrier) domain. After decoupling based on the proposed training signals, a cost function has been proposed to estimate the CFO of each BS separately. The detailed analysis and performance evaluation can be found in Chapter 4 and [25].

2.2 Synchronization in UL OFDMA Transmissions

As this dissertation deals with synchronization for both OFDMA and SC-FDMA UL transmissions, this section presents a joint system model and the signal structure for OFDMA and SC-FDMA UL transmissions. In addition, a literature review of synchronization schemes along with the contributions of this dissertation are discussed.

2.2.1 System Model and Signal Description

We consider a baseband equivalent system model of UL transmissions where M active MUs transmit to a BS using their allocated sub-carriers. Maximum number of MUs allowed in the system is denoted as M_u. Total number of sub-carrier is denoted as N while each MU is allocated $R = \left\lfloor \frac{N}{M_u} \right\rfloor$ exclusive sub-carriers. The set of indices of sub-carriers allocated to the m^{th} MU is denoted as $\mathcal{I}_m$. The block diagram of OFDMA/SC-FDMA system is shown in Figure 3, which shows that the SC-FDMA transmissions employ extra DFT/IDFT precoding at the Tx/Rx to achieve lower PAPR.

The information bit stream of the m^{th} MU, $0 \leq m \leq M-1$, is mapped to constellation symbols based on the specified modulation scheme. Each OFDMA symbol contains a block of R modulation symbols, denoted as an $R \times 1$ vector $\mathbf{S}_m$, which are mapped to the sub-carriers allocated to the m^{th} MU. The resulting OFDMA symbol

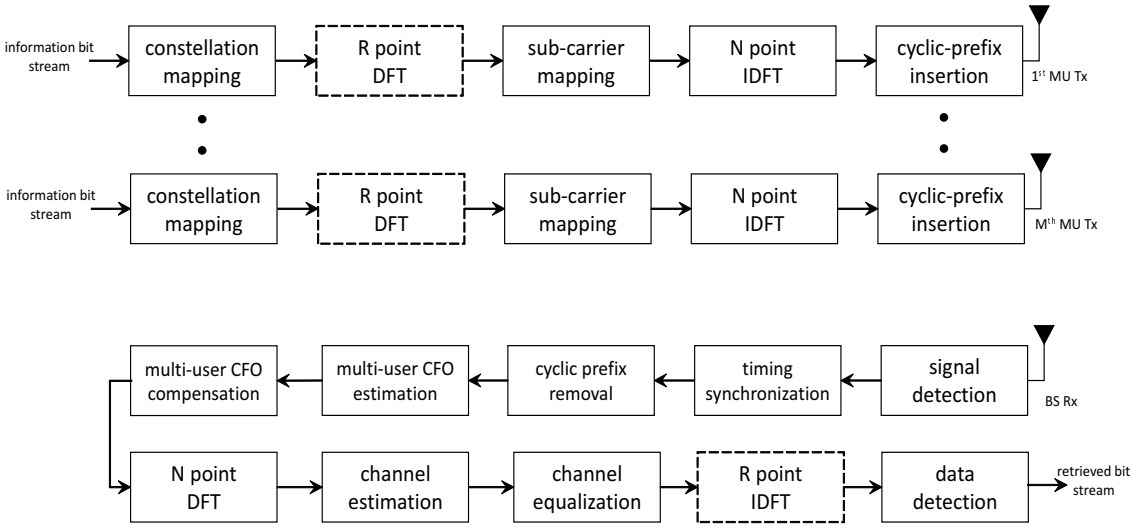

Figure 3: Block diagaram of an OFDMA/SC-FDMA system. The blocks with dashed lines are only part of an SC-FDMA system.

signal of the m^{th} MU is given as

$$\mathbf{X}_m = \mathbf{T}_m \mathbf{S}_m, \tag{8}$$

where $\mathbf{T}_m$ is the $N \times R$ sub-carrier mapping matrix given as $\mathbf{T}_m = \left[\mathbf{e}_{x_0}, \mathbf{e}_{x_1}, \ldots, \mathbf{e}_{x_{R-1}}\right]$, where $\mathbf{e}_x$ is the x^{th} column of the $N \times N$ identity matrix, and $x_r \in \mathcal{I}_m, 0 \leq r \leq R-1$. However, in SC-FDMA, the constellation symbols are pre-coded by an R-point DFT before sub-carrier mapping as shown in Figure 3. Thus, the SC-FDMA symbol is given as,

$$\mathbf{X}_m = \mathbf{T}_m \mathbf{F}_R \mathbf{s}_m. \tag{9}$$

The transmitted OFDMA/SC-FDMA is then formed by taking N point IDFT of the $\mathbf{X}_m$ as

$$\mathbf{x}_m = \mathbf{F}_N^H \mathbf{X}_m. \tag{10}$$

The purpose of R-point DFT pre-coding in SC-FDMA as in (9) is to cancel out the effect of high PAPR introduced by the following N-point IDFT. The effect of DFT precoding is discussed in detail in Chapter 6. A CP of N_g samples is then appended to the transmitted symbol.

The channel between the m^{th} MU and the BS is assumed to be of order P_m and denoted as $\tilde{h}_m[p], 0 \leq p \leq P_m - 1$. We assume that $N_g \geq P$ where $P = \max_m\{P_m + d_m\}$, and d_m is the timing offset (TO) of the m^{th} MU. Under this assumption, the TO of the m^{th} MU can be incorporated into its channel and the effective channel is given as

$$h_m[p] = \begin{cases} 0 & 0 \leq p \leq d_m - 1, \\ \tilde{h}_m[p - d_m] & d_m \leq p \leq P_m + d_m - 1, \\ 0 & P_m + d_m \leq p \leq P - 1, \end{cases} \tag{11}$$

Such a system is termed as *quasi-synchronous* system [51] as mentioned before in Section 1.2.

The signal received at the BS is the sum of the signals transmitted by all M active MUs. After CP removal, the received signal can be expressed as,

$$\mathbf{y} = \sum_{m=0}^{M-1} e^{j\frac{2\pi}{N} f_m(N_\mathrm{g})} \mathbf{D}_N(f_m) \mathbf{F}_N^H \mathbf{D}_N(\mathbf{H}_m) \mathbf{X}_m + \mathbf{w},$$

where f_m is the normalized CFO of the m^{th} MU, and $\mathbf{H}_m$ is the $N \times 1$ vector containing the N-point DFT of the m^{th} MU's effective CIR. Taking N-point DFT of the received signal at the BS results in

$$\mathbf{Y} = \sum_{m=0}^{M-1} e^{j\frac{2\pi}{N} f_m(qN_\mathrm{t}+N_\mathrm{g})} \mathbf{F}_N \mathbf{D}_N(f_m) \mathbf{F}^H \mathbf{D}_N(\mathbf{H}_m) \mathbf{X}_m + \mathbf{F}_N \mathbf{w}.$$

Note that if $f_m = 0$ for every MU, $\mathbf{F}_N \mathbf{D}_N(f_m) \mathbf{F}_N^H = \mathbf{I}_N$, and the MUs are perfectly separable and channel estimation and symbol detection can be performed for each MU. However, if f_m is non-zero, $\mathbf{F}_N \mathbf{D}_N(f_m) \mathbf{F}_N^H$ gives a non-diagonal matrix, which leads to ICI as well as MUI. Therefore, estimation and compensation of the CFOs are necessary for estimating the channels and decoding the signals from each MU.

2.2.2 Literature review of Synchronization Techniques for UL OFDMA and SC-FDMA Transmissions

Various CFO estimation algorithms for OFDMA and SC-FDMA UL transmissions have been proposed in the literature for different sub-carrier allocation schemes. As

SC-FDMA is a DFT pre-coded version of OFDMA, the synchronization techniques for OFDMA are also applicable to SC-FDMA.

CFO estimation techniques for SSAS in which a group of adjacent sub-carriers is allocated to each MU, have been proposed in [7, 80, 88]. To decouple different MU's signal on the UL, a guard band containing null sub-carriers is inserted between sub-bands of different MUs and band-pass filtering is used to separate each MU's signal. After separation, CFO estimation for each MU becomes equivalent to single-MU CFO estimation. However, due to non-zero CFOs, MU separation cannot be perfect and guard bands among MUs reduce the spectral efficiency. Cyclic-prefix-based CFO estimation has been proposed in [80] while 4^{th} order statistics of the received symbols are used for CFO estimation in [88]. Null sub-carriers in the guard band are used in [7] for CFO estimation.

GSAS is a hybrid of SSAS and ISAS in which each MU is allocated a number of small sub-bands or tiles. A tile is a grid of sub-carriers in frequency and time, and each MU is allocated specific tiles based on its channel condition and data rate requirement in order to obtain better channel diversity and dynamic resource allocation. Several CFO estimation schemes proposed in [15,49,61,65,74,83,84] are applicable for GSAS. Maximum likelihood CFO estimation and its low complexity approximations are proposed in [15, 61] using a training symbol transmitted at the start of the frame. However, the complexity of ML estimation is too high for practical implementations, while the low complexity approximations offer degraded performance. An iterative scheme is proposed in [84] in order to further lower the computational requirement of [61] while low complexity pilot-based CFO estimation has been proposed in [65, 74] in which pilots are inserted in some OFDMA symbols at the beginning of the frame.

In this dissertation, we have presented a CFO estimation algorithm for OFDMA uplink transmissions supporting both SSAS or GSAS. The proposed algorithm employs null sub-carriers for CFO estimation. However, instead of using null sub-carriers

as guard-bands as in [7, 80, 88], we move the null sub-carriers to the middle of the sub-band and form a cost function for CFO estimation by minimizing the interference on the null sub-carriers. The details can be found in Chapter 5 and [22]. The proposed algorithm requires less number of null sub-carriers as compared to previously proposed schemes and thus, improves the spectral efficiency. Moreover, the proposed algorithm is applicable to both SSAS and GSAS, while it is difficult to extend the previously mentioned schemes to GSAS.

CFO estimation schemes proposed in the literature for ISAS include [12, 13, 28, 37, 92, 93]. Multiple-signal classification or MUSIC algorithm is employed in [12] for CFO estimation using line search. A close form solution with better performance at lower signal-to-noise ratios (SNR) is proposed in [37] employing the estimation of signal parameters via rotational invariance technique or ESPRIT. As both MUSIC and ESPRIT as sub-space-based techniques, the CFO estimation schemes in [12, 37] require a non-empty noise sub-space for CFO estimation. This condition implies that the system cannot operate on full load or an extended CP must be employed, which reduces the overall spectral efficiency. Low complexity blind CFO estimation algorithm has been proposed in [28] while two CFO estimation methods for multi-antenna BSs, based on rank reduction and alternating projection methods are proposed in [92]. However, the schemes in [92] support fully loaded systems only when the BS has multiple antennae.

In addition to CFO estimation, various CFO compensation algorithms have also been proposed in the literature [5, 11, 29, 47, 94]. An interference cancelation scheme based on circular-convolution is proposed in [29] while parallel interference cancelation is used in [47] for CFO compensation. A linear de-correlator detector is proposed in [11]. However, the method is computationally intensive as it requires inversion of a large matrix for satisfactory performance. A joint CFO compensation and channel estimation algorithm is proposed in [5] for multi-antenna SC-FDMA systems. Finally,

several time-domain CFO compensation schemes paired with successive interference cancelation and MU ordering are proposed in [29].

In this dissertation, we have proposed a joint CFO estimation and compensation scheme for SC-FDMA UL transmissions with ISAS. The proposed scheme is based on tensor decomposition method known as parallel-factor (PARAFAC) analysis [18] and uses a training block of identical SC-FDMA symbols to perform CFO estimation and the estimation of MUI-free received training symbol. The main advantage of the proposed schemes is that it supports full load transmissions, improving the spectral efficiency. The PARAFAC decomposition also allows us to design a low-complexity CFO estimation schemes for the SC-FDMA symbols carrying data. The details on performance evaluations and complexity comparisons with the existing approaches can be found in Chapter 6 and [26].

CHAPTER III

TIMING AND FREQUENCY SYNCHRONIZATION FOR DOWNLINK OFDM TRANSMISSIONS

This chapter presents a cross-correlation-based detection and synchronization algorithm for DL OFDM transmissions. The proposed algorithm is data-aided and employs ZC sequences as training symbols. The structure of the training symbols is first discussed followed by the analysis of the cross-correlation of the received training symbol at the receiver. The analysis shows that the magnitude and location of cross-correlation peaks are dependent on the CFO and the ZC sequence parameters. It is illustrated that this sensitivity to CFOs can affect the identifiability of TO estimation. Based on the analysis, a criterion is proposed to choose suitable ZC sequence parameters in the training symbol to achieve robustness to CFOs. Based on the proposed sequences, a joint training signal detection and synchronization scheme is designed. The chapter concludes with simulation results to compare the performance of the proposed algorithms with the existing approaches in the literature.

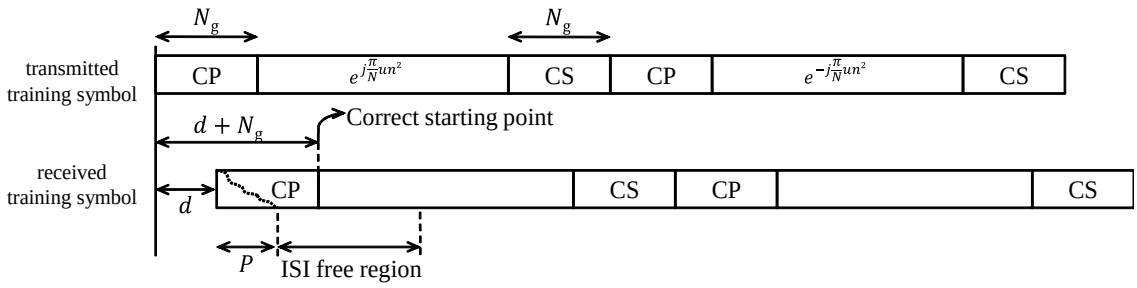

Figure 4: Proposed training symbol for downlink synchronization and the corresponding enlarged ISI-free region for a timing offset of d samples.

3.1 Training Signal Structure

We consider a base-band equivalent system model of an OFDM DL transmission as discussed in Section 2.1 in which a BS transmits a training block to the MU. The training block contains two ZC sequences, each with a CP of N_{CP} samples and a CS of N_{CS} samples, as shown in Figure 4. For simplicity, we take $N_{\mathrm{CP}} = N_{\mathrm{CS}} = N_{\mathrm{g}}$. The purpose of inclusion of CS is to enlarge the ISI-free region as shown in Figure 4 and to achieve robust timing synchronization as discussed later in Section 3.3. The n^{th} sample of the training block is given as

$$x[n] = \begin{cases} e^{j\frac{\pi}{N}u(n-N_{\mathrm{g}})^2} & 0 \leq n \leq N_{\mathrm{t}} - 1, \\ e^{-j\frac{\pi}{N}u(n-N_{\mathrm{t}}-N_{\mathrm{g}})^2} & N_{\mathrm{t}} \leq n \leq 2N_{\mathrm{t}} - 1, \end{cases} \tag{12}$$

where N is the length of the ZC sequence, u is the root index relatively prime to N, and $N_{\mathrm{t}} = N + 2N_{\mathrm{g}}$. Note that the samples $x[n]$ for $0 \leq n \leq N_{\mathrm{g}} - 1$ and $N_{\mathrm{t}} \leq n \leq N_{\mathrm{t}} + N_{\mathrm{g}} - 1$ are the CP for the first and second ZC sequences, respectively. Similarly, $N + N_{\mathrm{g}} \leq n \leq N_{\mathrm{t}} - 1$ and $2N_{\mathrm{t}} - N_{\mathrm{g}} \leq n \leq 2N_{\mathrm{t}} - 1$ comprise the CS. We assume an even value of N here, but similar analysis can be carried out for odd N as well. Note that the second ZC sequence of the training block is the complex conjugate of the first sequence.

As discussed in Section 2.1, the n^{th} sample of the received training block can be represented as

$$y[n] = e^{j\frac{2\pi}{N}fn} \sum_{p=0}^{P-1} h[p]x[n-d-p] + w[n]. \tag{13}$$

We assume that the CFO f is distributed as $f \sim \mathcal{U}[-f_{\max}, f_{\max}]$, where $\mathcal{U}[\cdot]$ represents the uniform distribution, and $f_{\max}$ is the maximum absolute value of the CFO. The CIR is distributed as $h[p] \sim \mathcal{CN}(0, \sigma_{\mathrm{p}}^2)$, where $\mathcal{CN}(\cdot)$ represents the complex Gaussian distribution, and σ_{p}^2 is the power of the p^{th}path. Similarly, AWGN samples are distributed as $w[n] \sim \mathcal{CN}(0, \sigma_{\mathrm{w}}^2)\ \forall n$, where σ_w^2 denotes the noise variance. We assume that different channel taps and AWGN samples are uncorrelated.

Timing and frequency synchronization provide TO and CFO estimates, denoted as $\hat{d}$ and $\hat{f}$, respectively. We employ the first ZC sequence in (12) for signal detection and coarse TO estimation, after which both ZC sequences are employed for CFO estimation and TO estimate refinement.

3.2 Timing Synchronization Using ZC Sequence

For timing synchronization, a cross-correlation of the received signal with the local copy of the training sequence can be used. In this section, we analyze cross-correlation-based timing synchronization using a generic ZC sequence with a CP and CS and its sensitivity to CFOs. The cross-correlation of the received signal in (13) with a local copy of the ZC sequence is given as

$$\begin{aligned} r[l] &= \frac{1}{N}\sum_{n=0}^{N-1} y[n+l]e^{-j\frac{\pi}{N}un^2} \\ &= \frac{1}{N}\sum_{n=0}^{N-1}\left(e^{j\frac{2\pi}{N}f(n+l)}\sum_{p=0}^{P-1}h[p]x[n+l-d-p]+w[n+l]\right)e^{-j\frac{\pi}{N}un^2}, \end{aligned} \tag{14}$$

where l is the lag of the cross-correlation. Note that, because of CP and CS, linear cross-correlation in (14) is similar to circular cross-correlation for $d \le l \le d+2N_{\mathrm{g}}$. We denote this set of sample range as the circular-correlation region, $\mathcal{R}_{\mathrm{cc}} \equiv \{l \in [d, d+2N_{\mathrm{g}}]\}$. For a channel with P taps, the ISI-free region is $l \in [d+P-1, d+2N_{\mathrm{g}}]$, as shown in Figure 4, and the circular-correlation region encloses the ISI-free region. Within $\mathcal{R}_{\mathrm{cc}}$, the l^{th} element of cross-correlation is

$$\begin{aligned} r[l] &= \frac{1}{N}e^{j\frac{2\pi}{N}fl}\sum_{p=0}^{P-1}h[p]\sum_{n=0}^{N-1}e^{j\frac{2\pi}{N}fn}e^{j\frac{\pi}{N}u(n+l-d-N_g-p)^2}e^{-j\frac{\pi}{N}un^2}+\frac{1}{N}\sum_{n=0}^{N-1}w[n+l]e^{-j\frac{\pi}{N}un^2} \\ &= \frac{1}{N}e^{j\frac{2\pi}{N}fl}\sum_{p=0}^{P-1}h[p]e^{j\frac{\pi}{N}u(l-d-N_g-p)^2}\left(\sum_{n=0}^{N-1}e^{j\frac{2\pi}{N}(u(l-d-N_g-p)+f)n}\right) \\ &+ \frac{1}{N}\sum_{n=0}^{N-1}w[n+l]e^{-j\frac{\pi}{N}un^2},\ l \in \mathcal{R}_{\mathrm{cc}}. \end{aligned} \tag{15}$$

In the absence of CFO, i.e., $f = 0$, the inner sum in (15) is non-zero only when $l = d + N_g + p,\ 0 \leq p \leq P-1$. Hence, the cross-correlation term in (15) simplifies to

$$r[l] = \sum_{p=0}^{P-1} h[p]\delta[l - d - N_g - p] + \frac{1}{N}\sum_{n=0}^{N-1} w[n+l]e^{-j\frac{\pi}{N}un^2}, \quad \text{if } f = 0, \tag{16}$$

with $\delta[l]$ being the Kronecker delta function. Note that (16) generates an estimate of the CIR for the set of indices $d + N_{\mathrm{g}} \leq l \leq d + N_{\mathrm{g}} + P - 1$, with the first tap $h[0]$ appearing at the correct starting index $r[d + N_{\mathrm{g}}]$. The rest of the cross-correlation values within $\mathcal{R}_{\mathrm{cc}}$ contain only noise. We denote the set of indices providing the CIR estimate as the 'CIR region' given as

$$\mathcal{R}_{\mathrm{CIR}} = \{l \in [d + N_{\mathrm{g}}, d + N_{\mathrm{g}} + P - 1]\} \subseteq \mathcal{R}_{\mathrm{cc}}, \text{if } f = 0. \tag{17}$$

As the CIR region, in the absence of CFO, is a subset of the ISI-free region, peak detection corresponding to the strongest channel tap can be used for coarse TO estimation [27]. The CIR region is also used for channel estimation and fine TO estimation in [81, 82], which assume that coarse timing synchronization and CFO compensation have already been performed. Thus, the receiver knows $\mathcal{R}_{\mathrm{cc}}$, and the residual CFO is also minimal. Based on these assumptions, a threshold is derived in [81] to locate the first tap of the multi-path channel that provides fine TO estimate in addition to the channel estimate provided by the cross-correlation. However, for a non-zero CFO, the value of the inner sum in (15) is clearly dependent on the CFO and decreases from N to zero as CFO increases from zero to one for each $l \in \mathcal{R}_{\mathrm{CIR}}$ in (17). In addition, each cross-correlation value becomes a weighted sum of the channel taps and no longer provides the CIR estimate. Therefore, the fine timing and the channel estimation algorithms in [81] cannot be applied for non-zero CFOs. This dependency on CFO implies that cross-correlation-based coarse timing synchronization using ZC sequence or any general CAZAC sequence is sensitive to large CFOs. Thus, the objective of the proposed scheme is twofold: to identify ZC

sequences, which offer robustness to CFOs and to design signal detection, TO and CFO estimation procedures using such sequences.

3.3 ZC Sequence Design for CFO Robustness

In this section, we discuss how to design ZC sequences for the proposed training block in (12) to achieve robustness to CFOs. Using proposed robust sequences, we will then design the detection and synchronization algorithms in the following sections. We denote the cross-correlation of the received training block with the first ZC sequence in (12) as $r_1[l]$. Within the circular-correlation region, the cross-correlation term is

$$r_1[l] = \frac{1}{N} e^{j\frac{2\pi}{N}fl} \sum_{p=0}^{P-1} h[p] e^{j\frac{\pi}{N}u(l-d-N_g-p)^2} \left(\sum_{n=0}^{N-1} e^{j\frac{2\pi}{N}(u(l-d-N_g-p)+f)n} \right) + \frac{1}{N} \sum_{n=0}^{N-1} w[n+l] e^{-j\frac{\pi}{N}un^2}, \; l \in \mathcal{R}_{\text{cc}}, \tag{18}$$

which is the same as (15).

3.3.1 Effect of Integer CFOs

Let us represent the CFO by the sum of an integer part f_{I} and a fractional part $-0.5 \leq f_{\text{F}} \leq 0.5$ so that $f = f_{\text{I}} + f_{\text{F}}$. In this section, we assume that $f_{\text{F}} = 0$ to concentrate on integer CFOs. Note that the sum within the parenthesis in (18) is non-zero only when

$$u(l - d - N_{\text{g}} - p) + f_{\text{I}} = mN, \tag{19}$$

where m is any integer and $l \in \mathcal{R}_{\text{cc}}$. For $f_{\text{I}} = 0$, the condition in (19) is satisfied whenever $l = d + N_{\text{g}} + p$, for any $0 \leq p \leq P-1$ with $m = 0$ and $r_1[l]$ reduces to (16) and $\mathcal{R}_{\text{CIR}}$ is the same as in (17). However, it is important to note that when f_{I} is a non-zero integer value, the condition in (19) will be satisfied for different values of lag l within the circular-correlation region, or it may not be satisfied at all. Hence, the indices or the values of lag l in $\mathcal{R}_{\text{CIR}}$ will change and shift away from the ideal location

in (17) for non-zero integer CFOs. The amount of shift depends on the values of N, u, and f_{I}. For example, with $N = 256$, $N_{\mathrm{g}} = 16$, $P = 12$, $f_{\mathrm{I}} = 1$, and $u = 85$, (19) is satisfied for $m = 1$ and $l = d+N_g+p+3$ with $\mathcal{R}_{\mathrm{CIR}} = [d+N_{\mathrm{g}}+3, d+N_{\mathrm{g}}+3+P-1]$, resulting in a shift of three samples in the CIR region, which still lies within the ISI-free region. In contrast, for $u = 17$ and $f_{\mathrm{I}} = 2$, (19) is satisfied for $m = 2$ and $l = d + N_g + p + 30$ with $\mathcal{R}_{\mathrm{CIR}} = [d + N_{\mathrm{g}} + 30, d + N_{\mathrm{g}} + 30 + P - 1]$, which is no longer within the ISI-free region. Hence, because of the shift in the CIR region in the presence of integer CFOs, the value of the root index can significantly affect the performance of TO estimation. The following two propositions show that the CIR region shifts linearly with CFO, and the elements in CIR region are unique.

Proposition 1: Let l_i denote the index of the CIR region corresponding to $h[0]$, for $f_{\mathrm{I}} = i$, where i is an integer. If there exists l_1 such that $u(l_1-N_g-d)+1 = m_1 N$, then $l_{i+1} = l_i+(l_1-N_g-d)$ satisfies $u(l_{i+1}-N_g-d)+i+1 = m_{i+1}N$ with $m_{i+1} = (i+1)m_1$.

Proof: See Appendix A.

A similar proposition shows that $l_{i-1} = l_i - (l_1 - N_g - d)$.

Proposition 2: The indices of $\mathcal{R}_{\mathrm{CIR}}$ within $\mathcal{R}_{\mathrm{cc}}$ are unique given $N_{\mathrm{g}} < \frac{N}{2}$.

Proof: See Appendix B.

Proposition 1 implies that, given u, N, N_{g}, and f_{I}, each element in $\mathcal{R}_{\mathrm{CIR}}$ shifts linearly by $s = l_1 - N_{\mathrm{g}} - d$ samples with a unit shift in f_{I}, and the value of s depends on the value of the root index u for a given N. Hence, for $f = f_{\mathrm{I}}$, $r_1[l]$ becomes

$$r_1[l] = e^{j\frac{2\pi}{N}f_I l}\sum_{p=0}^{P-1} h[p]\delta(l - d - N_g - p - sf_{\mathrm{I}}) + \frac{1}{N}\sum_{n=0}^{N-1} w[n+l]e^{-j\frac{\pi}{N}un^2}, \forall l \in \mathcal{R}_{\mathrm{cc}}. \tag{20}$$

Proposition 1 also implies that if f_{I} keeps on increasing, $\mathcal{R}_{\mathrm{CIR}}$ will eventually move out of $\mathcal{R}_{\mathrm{cc}}$, and if $l_{i\pm1} = l_i \pm (l_1 - N_g - d) \gtrless N$, then $(l_{i\pm1})_N$ satisfies (19), where $(\cdot)_N$ represents the modulo N operation. This implies that the shift in CIR region is eventually periodic. However, outside $\mathcal{R}_{\mathrm{cc}}$, linear correlation is no longer

equal to circular correlation. Moreover, in OFDM systems, the TO estimate must be within the ISI-free region, which is in turn a subset of $\mathcal{R}_{\text{cc}}$. As coarse TO will be estimated using cross-correlation values in the CIR region, whose location is unknown because integer CFO is unknown (CFO estimation is performed after coarse timing synchronization), it implies that the TO estimate also shifts left or right from the correct location by s samples with each unit increase or decrease in the integer CFO, respectively. If $f_{\max}$ is the maximum absolute integer CFO that can be observed in the system, $\mathcal{R}_{\text{CIR}}$ will be a subset of $[d+N_g-sf_{\max}, d+N_g+sf_{\max}+P-1]$. If the CIR region is restricted within the ISI-free region for $f \leq f_{\max}$, the TO estimate will also be within ISI-free region, which motivates the design of the proposed preamble. We introduce the CS along with the CP, which extends the circular-correlation region and allows the CIR region to shift in either direction and still remain within the ISI-free region for a certain maximum CFO given as

$$f_{\max} = \left| \left\lfloor \frac{N_{\text{g}} - (P-1)}{s} \right\rfloor \right|. \tag{21}$$

3.3.2 Choosing the Root Index

As the root index determines the amount of shift s in the CIR region for a unit change in CFO, it is important to select a root index which results in the minimum possible value of s, for it will maximize $f_{\max}$ in (21) that the coarse timing synchronization can handle. A smaller value of s also helps in training block detection, discussed in Section 3.4. Hence, we choose a root index that is relative prime to N based on the definition of ZC sequence and satisfies

$$u(l_1 - N_g - d) = us = m_1 N - f_{\text{I}} \tag{22}$$

for $f_{\text{I}} = 1$ or -1 with the minimum possible s. An obvious choice is $u = \pm 1$ or $\pm(N-1)$, which results in the minimum possible $s = \mp 1$. Otherwise, any factor of $m_1 N \pm 1$ that is relative prime to N can be used as u. For example, if N is an

even number not divisible by 3 (N is usually a power of 2 in OFDM systems), one of $m_1 N \pm 1$ must be divisible by $s = 3$, which provides the second minimum value of s for any even N. As an example, for $N = 256$, $N_g = 32$ and $P = 17$, $u = 1$ gives $s = -1$ and the TO estimate remains in the ISI-free region for $f_{\max} = 16$. For the same parameters, $u = 85$ gives $s = 3$ and $f_{\max} = 5$, while $u = 51$ gives $s = 5$ and $f_{\max} = 3$. As the length of CP in OFDM systems is always longer than the maximum excess delay of the channel, and $f_{\max}$ in practical systems is usually 1 or 2, a number of choices for root indices can be employed for specific values of N, N_{g}, and $f_{\max}$. For example, for the LTE-DL system parameters for 20 MHz transmission with extended CP, $N = 2048$ and $N_g = 512$. A typical clock accuracy of 10 ppm results in $f_{\max} = 2$, and ITU vehicular-A channel [30], as an example, has $P = 77$. For these practical system parameters, a number of feasible root indices exist including $u = \pm 1, \pm 91, \pm 273, \pm 315, \pm 585, \pm 455$, and ± 1365.

3.3.3 Choosing the Root Indices for ZC Sequences Defined in the Sub-carrier Domain

The proposed training block in (12) contains ZC sequences defined in the time domain. However, a training block can also be defined by modulating certain sub-carriers of an OFDM symbol with a ZC sequence. For example, in LTE DL, primary synchronization signal (PSS) contains ZC sequences, defined only for the middle 63 sub-carriers of the OFDM symbol. In this section, we discuss the design of root indices for ZC sequences for such training symbols. We derive a condition similar to (22) that can help the designer to choose root indices that minimize the shift s in the cross-correlation for integer CFOs. Please note that the synchronization algorithms proposed in the following sections are still based on the training signal in (12).

Let us consider an OFDM training symbol with a ZC sequence centered around DC sub-carrier occupying a subset of M sub-carriers out of N total sub-carriers, and

given as

$$X[k] = e^{j\frac{\pi}{M}u_f k(k+1)}, \quad k \in \mathcal{I} := \left\{ -\frac{(M-1)}{2}, \ \cdots, \ \frac{(M-1)}{2} \right\} \setminus \{0\}, \tag{23}$$

for odd M and

$$X[k] = e^{j\frac{\pi}{M}u_f k^2}, \quad k \in \mathcal{I} := \left\{ -\frac{M}{2}, \ \cdots, \frac{M}{2} - 1 \right\} \setminus \{0\}, \tag{24}$$

for even M, where k is the sub-carrier index, u_f is the root-index of the ZC sequence defined in the sub-carrier domain, and $\mathcal{I}$ is the set of sub-carriers modulated by the ZC sequence. The rest of the sub-carriers are zero[1]. As an example, in LTE DL transmissions $M = 63$. An IDFT (inverse discrete Fourier transform) of the training symbol followed by CP and CS insertions result in the training signal

$$x[n] = \sum_{k=-\frac{N}{2}}^{\frac{N}{2}-1} X[k] e^{j\frac{2\pi}{N}k(n-N_g)}, \quad 0 \leqslant n \leqslant N_t - 1. \tag{25}$$

The received signal is given as in (13). The cross-correlation is then given as

$$r[l] = \frac{1}{N} \sum_{n=0}^{N-1} y[n+l] x^*[n+N_g], \tag{26}$$

and the circular correlation region is still defined as $\mathcal{R}_{\text{cc}} = \{d \leq l \leq d + 2N_g\}$. We use the fact that the N-point circular correlation of two sequences in the time domain is equivalent to the point-by-point multiplication in the frequency domain of the N point DFT of one sequence and the conjugate of the DFT of the other sequence. As the N point DFT of $y[n]$, $d + N_g \leq n \leq d + N_g + N - 1$, for an integer CFO f_{I} is given as

$$Y[k] = \begin{cases} e^{-j\frac{2\pi}{N}k(d+N_g)} H[k - f_{\text{I}}] X[k - f_{\text{I}}] & k \in \mathcal{I}, \\ 0 & \text{otherwise}, \end{cases} \tag{27}$$

[1]If the training symbol also contain data sub-carriers as in PSS, low-pass filtering can be performed prior to cross-correlation to reject the contribution of data sub-carriers on the cross-correlation.

where $H[k]$ is the N point DFT of the CIR $h[p],\ 0 \leq p \leq P-1$, the cross-correlation in (26) for $l \in \mathcal{R}_{\text{cc}}$ can be equivalently expressed as

$$r[l] = \frac{1}{N} \sum_{k=-\frac{N}{2}}^{\frac{N}{2}-1} e^{-j\frac{2\pi}{N}k(d+N_g)} H[k-f_{\text{I}}] X[k-f_{\text{I}}] X^*[k] e^{j\frac{2\pi}{N}kl} + \frac{1}{N} \sum_{n=0}^{N-1} w[n]x^*[n], \forall l \in \mathcal{R}_{\text{cc}}. \tag{28}$$

Using the definition of the training symbol in (24), the product $X[k-f_{\text{I}}]X^*[k]$ is non-zero for $k \in \mathcal{I}' := [\frac{-M}{2} + f_{\text{I}}, \ldots, -1, f_{\text{I}}+1, \ldots, \frac{M}{2}-1]$ for a positive f_{I}, and $\mathcal{I}' := [\frac{-M}{2}, \ldots, f_{\text{I}}-1, 1, \ldots, \frac{M}{2}-1]$ for a negative f_{I}. Hence,

$$r[l] = \frac{1}{N} e^{j\frac{\pi}{M}u_f f_{\text{I}}^2} \sum_{p=0}^{P-1} h[p] e^{j\frac{2\pi}{N}f_I p} \left(\sum_{k \in \mathcal{I}'} e^{j\frac{2\pi}{N}(l-d-N_g-p-\frac{N}{M}u_f f_{\text{I}})k} \right) + \frac{1}{N} \sum_{n=0}^{N-1} w[n]x^*[n]. \tag{29}$$

The term inside the parentheses is maximum (equal to $|\mathcal{I}'|$) whenever lag l satisfies

$$l - d - N_g - p - \frac{N}{M} u_f f_{\text{I}} = mN, \tag{30}$$

where m is any integer. The training sequence with odd M in (23) also results in the same condition. This condition is in fact similar to the condition in (22) (with $p = 0$ except that N is replaced by $\frac{N}{M}$), and it can be used to predict the shift in the cross-correlation peak with integer CFOs. Unlike (20), the cross-correlation in (29) does not yield the CIR when $M < N$. However, the peak or energy detection can still be used for training block detection and coarse timing synchronization for appropriately chosen root indices. Analyzing (30), $u_f = \pm 1$ again results in the minimum value of the shift $s = 1$. However, as $\frac{N}{M}$ may not be an integer, the value of s may not be exactly an integer for an integer CFO. Viewed in another way, in order to get an integer s, the value of CFO may not be exactly an integer. For example, in one of the LTE PSSs, $N = 2048$, $M = 63$, and $u_f = 25$ result in $s = 812.69 \approx 813$ samples for $f = 1$, or $s = 813$ samples for $f = 1.004 \approx 1$. Table I shows the values of shifts obtained for $f = 1$ and 2 in all three LTE PSSs. As obvious, none of the

Table 1: Shifts in cross-correlation maxima with integer CFOs for root indices of LTE downlink PSS.

root index (u_f)	s ($f=-2$)	s ($f=-1$)	s ($f=0$)	s ($f=1$)	s ($f=2$)
25	423	−813	0	813	−423
29	−163	−943	0	943	−163
34	163	943	0	−943	163

root indices have s that lies in ISI-free region for $f = 1$. Hence, cross-correlation-based synchronization is not feasible for LTE in the presence of integer CFOs without further modifications. Thus, blind coarse-timing synchronization, as opposed to cross-correlation-based timing synchronization, is usually proposed for LTE DL, as in [46].

3.4 Detection and Coarse Timing Offset Estimation with Unknown CFO

The previous section described the effect of integer CFOs on timing synchronization and presented conditions to select the appropriate root indices of the ZC sequences to achieve robustness to integer CFOs. However, the effect of fractional CFO was neglected for simplification. We observed that integer CFOs do not affect the values of the cross-correlation but result only in a translation of these values. Therefore, from a perspective of fractional CFOs, zero or non-zero integer CFOs are the same, and the analysis for fractional CFOs with zero integer CFO can be directly applied to the case of non-zero integer CFOs for the corresponding shifted samples.

In this section, we develop training block detection and coarse timing synchronization schemes using the ZC sequences with proposed root indices. Note that, for detection and coarse timing synchronization, only the first ZC sequence in the training block in (12) is employed. Also, f_{F} is no longer zero so that $|f| \leq f_{\max}$ is a real

number. Eq. (18) can then be written as

$$r_1[l] = e^{j\frac{\pi}{N}(2l+N-1)f} e^{j\frac{\pi}{N}u((l-d-N_g)^2+(N-1)(l-d-N_g))} \sum_{p=0}^{P-1} h[p] e^{j\frac{\pi}{N}u\left(p^2-\{2(l-d-N_g)+N-1\}p\right)}$$

$$\times \Psi\left(u\{p-(l-d-N_g)\}\right) + \frac{1}{N}\sum_{n=0}^{N-1} w[n+l] e^{-j\frac{\pi}{N}un^2}, \quad \forall l \in \mathcal{R}_{\text{cc}}, \tag{31}$$

where

$$\Psi\left(u\{p-(l-d-N_g)\}\right) = \frac{1}{N}\frac{\sin\pi\left(u(p-(l-d-N_g))-f\right)}{\sin\frac{\pi}{N}\left(u(p-(l-d-N_g))-f\right)}.$$

As each channel tap $h[p] \sim \mathcal{CN}(0, \sigma_p^2)$ and different taps of the channel and noise samples are assumed to be uncorrelated, the cross-correlation values are distributed as follows:

$$r_1[l] \sim \mathcal{CN}\left(0, \sum_{p=0}^{P-1} \sigma_p^2 \Psi^2\left(u\{p-(l-d-N_g)\}\right) + \frac{\sigma_w^2}{N}\right), \tag{32}$$

for each $l \in \mathcal{R}_{\text{cc}}$, given s and f. $\Psi^2(x)$ is a periodic $\frac{\text{sinc}^2}{\text{sinc}^2}$ type of function whose magnitude is maximum (equal to 1) in the center of its main lobe ($|x| \leq 1$) and decreases rapidly as the distance from the main lobe increases when $|x|$ increases. As p varies, different samples of $\Psi^2\left(u\{p-(l-d-N_g)\}\right)$ contribute to the summation in (32). These samples have significant magnitude only for those values of p that satisfy $p-(l-d-N_g) = ms$, where m is any integer because $ums = mm_1N - m$ and a sample close to the main lobe of $\Psi^2\left(u\{p-(l-d-N_g)\}\right)$ is obtained. In that case,

$$\Psi^2\left(u\{p-(l-d-N_g)\}\right) = \frac{\sin^2(\pi f)}{\sin^2\frac{\pi}{N}(m+f)} \approx \frac{N^2\sin^2(\pi f)}{\pi^2(m+f)^2},$$

where we use $\sin^2(x) \approx x^2$ for small x. Thus, neglecting the samples far from the main lobe and applying some algebraic manipulations, (31) and (32) can be approximated as

$$r_1[l'] \approx \frac{\sin(\pi f)}{\pi} e^{j\frac{\pi}{N}(2l+N-1)f} \sum_{m=-\lfloor\frac{l'}{s}\rfloor}^{\lfloor\frac{P-1-l'}{s}\rfloor} h[ms+l'] e^{-j\frac{\pi}{N}(m^2s+m)} \frac{1}{(m+f)}$$

$$+ \frac{1}{N}\sum_{n=0}^{N-1} w[n+l'+d+N_g] e^{-j\frac{\pi}{N}un^2}, \tag{33}$$

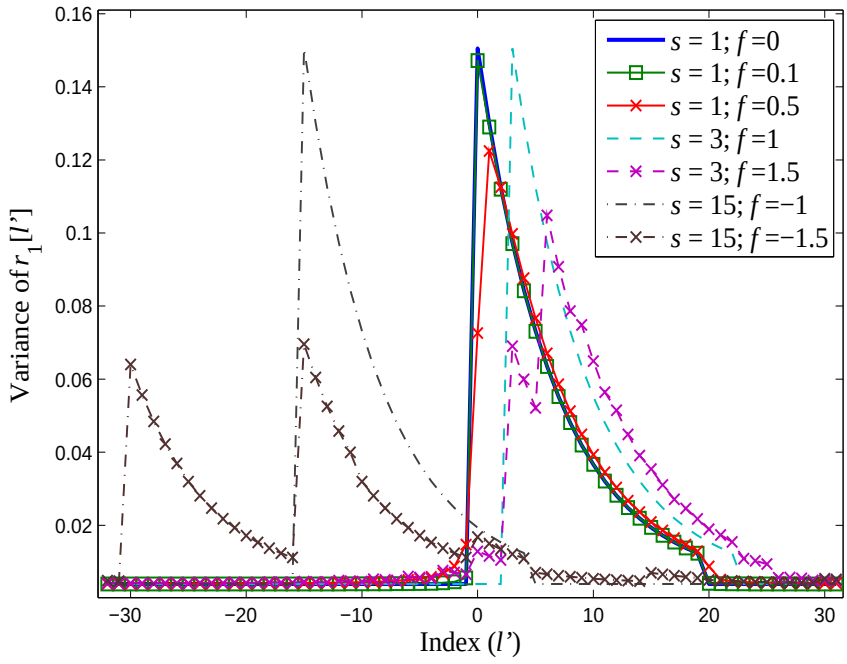

Figure 5: Variance of cross-correlation $r_1[l']$ with different values of shift s and CFO f; $N = 256$, $N_g = 32$, $P = 20$.

for $0 \leq l' = l - d - N_g \leq P - 1$, and

$$r_1[l'] \sim \mathcal{CN}\left(0, \frac{\sin^2(\pi f)}{\pi^2} \sum_{m=-\lfloor \frac{l'}{s} \rfloor}^{\lfloor \frac{P-1-l'}{s} \rfloor} \sigma^2_{ms+l'} \frac{1}{(m+f)^2} + \frac{\sigma_w^2}{N}\right). \tag{34}$$

We see that in the presence of fractional CFOs, the cross-correlation no longer provides channel estimates, for each cross-correlation value within $\mathcal{R}_{\text{cc}}$ is a weighted sum of the CIR. As an illustration, Figure 5 shows the change in the variance of $r_1[l]$ in (34) for an exponential power delay profile (PDP), with $N = 256$, $N_{\text{g}} = 32$, $P = 20$, and different values of CFO and shift s. As shown, $f = 0$ provides the actual PDP of the channel starting at $l' = 0$, while it shifts by 3 and -15 samples for $f = 1$ and $f = -1$ with $s = 3$ and $s = 15$, respectively, while the values remain the same. However, as f_{F} changes, the change in the variance depends on f_{F} itself as well as the values of s. As f changes from an integer i to $i+1$, the PDP obtained at $l' \in [is : is + P - 1]$ begins to decrease while its copy at $l' \in [(i+1)s : (i+1)s + P - 1]$

begins to increase until the former disappears completely at $f = i + 1$. For any intermediate value between i to $i + 1$, the resultant variance of the cross-correlation is given by (34). If $s \ll P$, the resultant variance is still concentrated in a region $[is : (i + 1)s + P - 1]$, as shown in Figure 5 for $s = 1$ and 3. However, if s is comparable to P, two copies remain distinct because of a higher value of s, and the effective PDP expands, as shown in the case of $s = 15$. Moreover, Eq. (33) shows that the correlation between $r_1[l']$, ..., $r_1[l' + s - 1]$ is very small (less than $\frac{\sigma_w^2}{N}$) as it is only due to noise samples and $\sigma_w^2 \ll N$ for practical SNR. We define the SNR as $\frac{\sum_{p=0}^{P-1} \sigma_k^2}{\sigma_w^2}$. The correlation between $r_1[l']$ and $r_1[l' \pm is]$ is given as

$$\sigma_{r_1[l'],r_1[l'\pm is]} = \frac{\sin^2(\pi f)}{\pi^2} e^{j\frac{2\pi}{N}isf} \sum_{m=\lfloor -\frac{l'}{s} \rfloor}^{\lfloor \frac{P-1-l'}{s} \rfloor} \sigma_{ms+l'}^2 \frac{1}{(m+f)(m \mp i + f)}. \tag{35}$$

As expected, when f is an integer, the correlation in (35) is zero and increases as $|f_{\mathrm{F}}|$ increases from 0 to 0.5. However, as the factor $\frac{1}{(m\pm f)(m\mp i\pm f)}$ decreases exponentially with m, the correlation is still very small particularly for exponential PDPs and small values of s. Hence, as an approximation to simplify the synchronization and detection schemes, we assume that cross-correlation samples are uncorrelated.

3.4.1 Neyman-Pearson Detection

After gaining insights into the distribution of cross-correlation, we now focus on the design of training block detection and coarse timing synchronization algorithms. To distinguish the presence or absence of a training block, we also need the distribution of cross-correlation outside the circular-correlation region. We assume that the training sequence is transmitted as a preamble and the received signal before the training block contains only noise samples. Assuming that the noise samples are uncorrelated, the distribution of the cross-correlation is

$$r_1[l'] \sim \mathcal{CN}\left(0, \frac{\sigma_w^2}{N}\right), \quad l' < 0. \tag{36}$$

To find a criterion for determining whether the cross-correlation values come from a received training symbol or only noise samples, we use the Neyman-Pearson (NP) test [33]. Instead of processing each output sample of the cross-correlation individually, we process a window of cross-correlation samples to take all the samples of cross-correlation, corresponding to the CIR region, into account simultaneously. We assume $s \ll P$ so that the extension in the CIR region in the presence of fractional CFOs is minimal. The test evaluates the absolute values in a window of last P samples of the cross-correlation $\mathbf{r}[l] = [|r_1[l-(P-1)]|, \ldots, |r_1[l]|]^T$ to declare in favor of the null or the alternative hypothesis defined as

Null Hypothesis (H_o):

$$\mathbf{r}[l] \sim \left(\frac{2}{\sigma_{\tilde{w}}^2}\right)^P \exp\left(-\frac{1}{\sigma_{\tilde{w}}^2}\sum_{k=0}^{P-1}|r_1[l+k-(P-1)]|^2\right)\prod_{k=0}^{P-1}|r_1[l+k-(P-1)]|, \tag{37}$$

with $\sigma_{\tilde{w}}^2 = \frac{\sigma_w^2}{N}$.

Alternative Hypothesis (H_a):

$$\mathbf{r}[l] \sim \exp\left(-\sum_{k=0}^{P-1}\frac{1}{\sigma_k^2}|r_1[l+k-(P-1)]|^2\right)\prod_{k=0}^{P-1}\left(\frac{2}{\sigma_k^2}|r_1[l+k-(P-1)]|\right), \tag{38}$$

with

$$\sigma_k^2 = \frac{\sin^2(\pi f)}{\pi^2}\sum_{m=-\lfloor\frac{k}{s}\rfloor}^{\lfloor\frac{P-1-k}{s}\rfloor}\sigma_{ms+k}^2\frac{1}{(m+f)^2} + \sigma_{\tilde{w}}^2, \tag{39}$$

where we use the fact that the absolute value of a complex Gaussian random variable has Rayleigh distribution. In addition, we assume that the cross-correlation values are uncorrelated in the cross-correlation region as discussed in the previous section. Through simulations in Section 3.6, we will demonstrate that the effect of this independence assumption is minimal. Based on the null and alternative hypotheses, the NP test is given as

Decide H_a if

$$\frac{\Pr[\mathbf{r}[l];H_a]}{\Pr[\mathbf{r}[l];H_o]} = \frac{(\sigma_{\tilde{w}}^2)^P}{\prod_{k=0}^{P-1}\sigma_k^2}\exp\left(-\sum_{k=0}^{P-1}|r_1[l+k-(P-1)]|^2\left(\frac{1}{\sigma_k^2}-\frac{1}{\sigma_{\tilde{w}}^2}\right)\right) > \gamma, \quad (40)$$

where γ is the threshold. Eq. (40) is equivalent to

$$\frac{1}{P}\sum_{k=0}^{P-1}\frac{\sigma_k^2-\sigma_{\tilde{w}}^2}{\sigma_k^2\sigma_{\tilde{w}}^2}|r_1[l+k-(P-1)]|^2 > \gamma', \quad (41)$$

where γ' is the value satisfying

$$\Pr\left[\frac{1}{P}\sum_{k=0}^{P-1}\frac{\sigma_k^2-\sigma_{\tilde{w}}^2}{\sigma_k^2\sigma_{\tilde{w}}^2}|r_1[l+k-(P-1)]|^2 > \gamma'\right] = P_{\text{FA}}, \quad (42)$$

under H_o for a target probability of false alarm P_{FA}. Under H_o, $\frac{1}{P}\frac{\sigma_k^2-\sigma_{\tilde{w}}^2}{\sigma_k^2\sigma_{\tilde{w}}^2}|r_1[l+k-(P-1)]|^2$ for each $k \in [0, P-1]$ has exponential distribution with rate $\lambda_k = \frac{P\sigma_k^2}{\sigma_k^2-\sigma_{\tilde{w}}^2}$. Therefore, $\frac{1}{P}\sum_{k=0}^{P-1}\frac{\sigma_k^2-\sigma_{\tilde{w}}^2}{\sigma_k^2\sigma_{\tilde{w}}^2}|r_1[l+k-(P-1)]|^2$ has the hypo-exponential distribution [64, p. 308] and

$$\Pr\left[\frac{1}{P}\sum_{k=0}^{P-1}\frac{\sigma_k^2-\sigma_{\tilde{w}}^2}{\sigma_k^2\sigma_{\tilde{w}}^2}|r_1[l+k-(P-1)]|^2 > \gamma'\right] = \sum_{k=0}^{P-1}C_{k,P}\exp\left(-\gamma'\lambda_k\right), \quad (43)$$

where

$$C_{k,P} = \prod_{\substack{m=0,1,\ldots,P-1\\ m\neq k}}\frac{\lambda_m}{\lambda_m-\lambda_k}. \quad (44)$$

Hence, the test for signal detection calculates a running weighted power estimate of the cross-correlation according to (41), and if the estimate is greater than γ', it declares the detection of the training block. The corresponding index is then taken as the coarse TO estimate $\hat{d}$. Thus,

$$\hat{d} = l - P + 1 : \frac{1}{P}\sum_{k=0}^{P-1}\frac{\sigma_k^2-\sigma_{\tilde{w}}^2}{\sigma_k^2\sigma_{\tilde{w}}^2}|r_1[l+k-(P-1)]|^2 > \gamma'. \quad (45)$$

However, in some cases, the condition in (45) can be triggered early due to a partial correlation with the CP of the training signal for $l = d + N_g - N$. In order to avoid a wrong TO estimate in that case, the algorithm picks the index of the maximum

value of the power estimate in (45) out of the $N + N_g$ indices following the index for which the condition in (45) is satisfied. From Eq. (41) and (42), it is clear that both the test criterion and the calculation of γ' require knowledge of the channel PDP and the $\sigma^2_{\tilde{w}}$. In addition, the calculation of σ^2_k in (39) also requires the values of CFO. We now derive an approximation that can alleviate some of these requirements.

3.4.2 Simplified Neyman-Pearson Detection

As $\sigma^2_{\tilde{w}} = \frac{\sigma^2_w}{N}$, it implies that $\sigma^2_{\tilde{w}} \ll \sigma^2_k$, especially for high values of SNR and/or large N. Moreover, channel taps below the noise floor of the system cannot be estimated. Therefore, $\lim_{\mathrm{SNR}\to\infty} \lambda_k = \lim_{\mathrm{N}\to\infty} \lambda_k = P$, and the asymptotic distribution of the weighted windowed energy in (41) approaches the Erlang distribution with rate P. Using this approximation, (43) simplifies to

$$\Pr\left[\frac{1}{P}\sum_{k=0}^{P-1}\frac{\sigma^2_k - \sigma^2_{\tilde{w}}}{\sigma^2_k\sigma^2_{\tilde{w}}}|r_1[l+k-(P-1)]|^2 > \gamma'\right] = \sum_{k=0}^{P-1}\frac{1}{k!}\exp\left(-P\gamma'\right)(P\gamma')^k. \quad (46)$$

Similarly, the test criterion in (41) can be approximated as

$$\frac{1}{P}\sum_{k=0}^{P-1}\frac{1}{\sigma^2_{\tilde{w}}}|r_1[l+k-(P-1)]|^2 > \gamma'. \quad (47)$$

Note that neither the test criterion nor the calculation of γ' for this approximation depend on the channel PDP or CFO. However, the test still requires an estimate of the noise variance [78], which is also required for fine TO estimation in [81]. The value of P can be calculated through the delay spread of the channel. We will evaluate the robustness of this simplified NP detection and compare its performance with the original detection test in (41) in Section 3.6.

This simplified NP detection completes the discussion of training block detection and coarse timing synchronization. We have investigated the effect of integer CFOs on cross-correlation-based timing synchronization using ZC sequences and shown that given system parameters, some ZC sequences can minimize the shift in the CIR region as the CFO increases. A smaller value of s also helps to maintain the channel profile

within the CIR region and allows us to design a test used for both signal detection and coarse TO estimation. A simplified test criterion also alleviates the constraints of *a priori* information about channel PDP and CFO. Thus, the proposed cross-correlation-based detection and coarse timing synchronization schemes are robust to CFOs as these schemes do not requiring the knowledge of CFOs. Once the training block is detected and correspondingly, a coarse TO estimate is available, the receiver can proceed to CFO estimation, discussed in the following section.

Noise variance estimation The simplified NP test in (47) requires an estimate of the effective noise variance $\sigma^2_{\tilde{\omega}}$ for which noise estimation methods proposed in the literature like [78] can be employed. Although, proposing a new noise variance estimation method is beyond the scope of this dissertation, we present a simple scheme for noise variance estimation. As the proposed training block is transmitted as a preamble, the received signal before the preamble contains only noise. Therefore, we use a running power estimate of the received signal samples for noise variance estimation. Specifically, if the cross-correlation for lag l is computed as in (14), $\sigma^2_{\tilde{\omega}}$ used for detection employing $r[l]$, is estimated as,

$$\hat{\sigma}^2_{\tilde{\omega}}[l] = \frac{1}{MN} \sum_{n=0}^{M-1} |y[l - n - 2N_g]|^2, \tag{48}$$

where M is the number of samples used for noise-variance estimation. A lag of $2N_g$ samples ensures that $\sigma^2_{\tilde{\omega}}$ estimate in (48) employs only noise samples for $l \in \mathcal{R}_{cc}$. The accuracy of noise variance estimate will degrade (larger than the actual value) as the cross-correlation moves further along samples ($l > d + 2N_g$) but it actually helps in reducing false alarms according to (47) as the noise variance estimate will be larger than the actual value. We show the effect of noise variance estimation on the performance of simplified NP test in Section 3.6.

Midamble detection A training block can also be transmitted as a midamble, which refers to a training block with at least one data symbol before and after it. For example, in LTE DL with the extended-CP mode, a training block is transmitted in the sixth OFDM symbol of each half-frame containing sixty OFDM symbols. We discuss how the proposed training block detection and coarse timing synchronization scheme can be adapted for midamble detection. We assume, as in the case of cellular communications, that a continuous stream of signal is transmitted on the DL. Therefore, *noise only* hypothesis does not exist in this case; rather the *noise only* case is replaced by the *noise + random data* case. A false alarm now refers to a case in which a cross-correlation with the random data symbol preceding the training symbol is mistaken as the training symbol. However, assuming that the data symbols are uncorrelated from the training block, midamble detection can be performed as preamble detection with increased noise level. Assuming that the transmitted signal has unit power and the channel has unit average energy, the distribution of $r_1[l']$ under the null hypothesis is given as

$$r_1[l'] \sim \mathcal{CN}\left(0, \frac{\sigma_w^2 + \sum_{p=0}^{P-1} \sigma_p^2}{N}\right) = \mathcal{CN}\left(0, \frac{\sigma_w^2 + 1}{N}\right), \quad l' < 0, \tag{49}$$

as opposed to (36). The test criterion and the calculation of the threshold in (41) and (42), respectively, remain the same with $\sigma_{\tilde{w}}^2$ replaced by $\frac{\sigma_w^2+1}{N}$. As the effective noise variance for the test criterion, that is, $\frac{\sigma_w^2+1}{N}$ does not approach zero with higher SNR values, the approximation in Sec. 3.4.2 is valid only for large values of N. However, an advantage of the frame-based continuous transmission is that the receiver can take advantage of the *a priori* information about periodicity of the midamble. Specifically, if the midamble is repeated once every S OFDM symbols, the receiver can perform peak detection on the running power estimate in (47) corresponding to all S symbols, followed by peak validation using the threshold γ'. Therefore, for midamble detection,

the test in (47) can be modified as follows: Decide H_a if

$$\max\left(\frac{1}{P}\sum_{k=0}^{P-1}\frac{N}{\sigma_{\tilde{w}}^2+1}|r_1[l+k-(P-1)]|^2\right)>\gamma' \quad 0\leq l\leq NS. \tag{50}$$

and the TO estimate can be obtained from the index of the maximum value of the metric in (50). As the '*noise only*' hypothesis is replaced by the '*noise + random data*', the method for noise variance estimation described above can also be used for midamble detection.

3.5 Carrier Frequency Offset Estimation

In this section, we discuss CFO estimation using the proposed training block. As CFO estimation requires an estimate of the symbol boundaries, the coarse TO estimate obtained through the NP test is employed for CFO estimation. Fractional CFO estimation is carried out first, followed by integer CFO estimation.

3.5.1 Fractional CFO Estimation

For fractional CFO estimation, we use correlation-based CFO estimation proposed in [44]. A blind timing and CFO estimation scheme is proposed in [44] using a correlation of the CP of the received signal with its corresponding samples. As the first P samples of the CP are corrupted by the ISI, the CFO estimate is correct if the last $N_{\mathrm{g}}-P$ samples of the CP are employed for CFO estimation. However, in the proposed training block, apart from the last $N_{\mathrm{g}}-P$ samples of the CP, all the samples corresponding to the CS are also ISI-free for both the first and the second ZC sequence. Thus, we employ the CS and its corresponding samples of both ZC sequences for fractional CFO estimation. Specifically, the fractional CFO estimate can be obtained as

$$\hat{f}_{\mathrm{frac}}=\frac{1}{2\pi}\,\mathrm{Im}\left(\ln\left(\sum_{n=0}^{N_{\mathrm{g}}-1}y[\hat{d}+n]y^*[\hat{d}+n+N]+\sum_{m=N_{\mathrm{t}}}^{N_{\mathrm{t}}+N_{\mathrm{g}}-1}y[\hat{d}+m]y^*[\hat{d}+m+N]\right)\right). \tag{51}$$

where $\hat{d}$ is the coarse TO estimate obtained using the original (41) or simplified NP test (47). For a non-zero f_{I}, the coarse TO estimate can have an error of sf_{I} samples as compared to the ideal TO estimate, i.e., $d + N_g$. However, for the proposed root indices, $s \ll N_{\mathrm{g}}$, and the effect of this shift can be neglected. Once $\hat{f}_{\mathrm{frac}}$ is available, its effect can be removed from each received OFDM symbol as follows:

$$y_c[n] = e^{-j\frac{2\pi}{N}fn}y[n] \quad 0 \leq n \leq N_{\mathrm{t}} - 1. \tag{52}$$

3.5.2 Integer CFO Estimation

After fractional CFO estimation and compensation, we employ both ZC sequences in the training block to estimate the integer CFO. As coarse TO estimate $\hat{d}$ is already available, the receiver has an estimate of the indices of the circular correlation regions corresponding to both ZC sequences in the training block. The receiver then calculates cross-correlations of the compensated training block with both ZC sequences given as

$$r_1[l] = \sum_{n=0}^{N-1} y_c[n+l]e^{-j\frac{\pi}{N}un^2},\ \hat{d} - N_{\mathrm{g}} \leq l \leq \hat{d} + N_{\mathrm{g}} - 1, \tag{53}$$

and

$$r_2[l] = \sum_{n=0}^{N-1} y_c[n+l]e^{j\frac{\pi}{N}un^2},\ \hat{d} - N_{\mathrm{g}} + N_{\mathrm{t}} \leq l \leq \hat{d} + N_{\mathrm{g}} + N_{\mathrm{t}} - 1, \tag{54}$$

for their respective circular correlation regions. As the fractional CFO has already been compensated for, both cross-correlations will provide an estimate of the CIR, but the locations of CIR regions will differ. As the second ZC sequence in the training block is the conjugate of the first sequence, the root index of the second ZC sequence is $-u$, instead of u for the first sequence. Therefore, if the CIR region for $r_1[l]$ is $\mathcal{R}_{\mathrm{CIR},1} = [d + N_{\mathrm{g}} + sf_{\mathrm{I}}, d + N_{\mathrm{g}} + sf_{\mathrm{I}} + P - 1]$, the CIR region for $r_2[l]$ will be $\mathcal{R}_{\mathrm{CIR},2} = [d + N_{\mathrm{g}} + N_{\mathrm{t}} - sf_{\mathrm{I}}, d + N_{\mathrm{g}} + N_{\mathrm{t}} - sf_{\mathrm{I}} + P - 1]$. The maximum distance between the CIR regions of $r_1[l]$ and $r_2[l]$ can be $2sf_{\max}$. As the location of CIR regions is dependent on f_{I}, the index for which the difference between the two cross-correlations is minimized can be used to estimate f_{I}. Specifically, a integer CFO

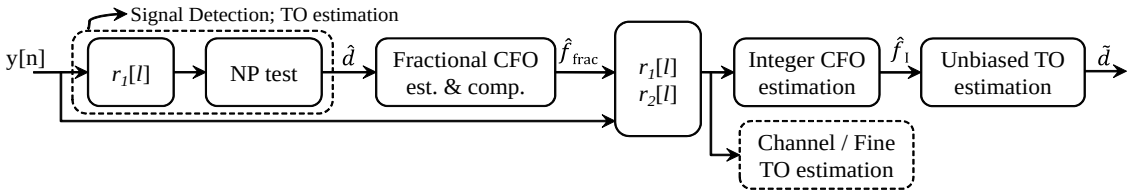

Figure 6: Block diagram of the proposed downlink synchronization scheme.

metric is calculated as

$$M(i) = \sum_{l=-N_{\text{g}}}^{N_{\text{g}}-1} (|r_1[l+\hat{d}]| - |r_2[l+\hat{d}+N_{\text{t}}-i]|), -2sf_{\max} \leq i \leq 2sf_{\max}, \tag{55}$$

and f_{I} is estimated as,

$$\hat{f}_{\text{I}} = \frac{\arg\min_i M(i)}{2s}. \tag{56}$$

3.5.3 Refined Timing Offset Estimation

As discussed in the previous section, a non-zero f_{I} causes a shift in the CIR region, creating a bias of sf_{I} samples in the coarse TO estimate. Once the estimate of the integer CFO ($\hat{f}_{\text{I}}$) is available, the bias can be removed. The unbiased TO estimate ($\tilde{d}$) is computed as

$$\tilde{d} = \hat{d} - \hat{f}_{\text{I}} s. \tag{57}$$

Apart from integer CFO estimation, (53) and (54) also provide the CIR estimate, which can be used for fine TO estimation, as in [81]. This completes the discussion on synchronization using the proposed training block, and the block diagram of the proposed scheme is shown in Figure 6. The detection and coarse timing synchronization procedures are entirely based on cross-correlation and threshold-based validation. In addition, after fractional CFO estimation and compensation, cross-correlation provides the integer CFO, the channel, and fine TO estimates. In the literature, integer CFO estimation is usually performed using correlation of the received training symbol in sub-carrier domain, as in [67], which increases the complexity and the latency

of integer CFO estimation. Hence, as the hardware resources used for computing cross-correlations can be used for CFO, coarse TO, fine TO, and channel estimation, the proposed scheme is conducive to practical implementation.

3.6 Simulation Results

In this section, we evaluate the performance of the proposed algorithms through Monte Carlo simulations and make comparisons with some of the existing approaches in the literature. Transmission is simulated in the form of packets, where each packet contains the preamble (training block) followed by 20 OFDM symbols carrying data. For training block detection tests, we simulate for $N = 64, 128$, and 256 with $u = -1$, which gives $s = 1$. For timing and CFO estimation, $N = 256$ is employed with $u = -1, 85$, and 51. The length of CP is $N_{\text{CP}} = \frac{N}{8}$ and $f_{\max} = 2$. The CFO for each iteration of the simulation is drawn randomly from $[-f_{\max}, f_{\max}]$. The channel is modeled as a Rayleigh fading channel with six taps and an exponential PDP given as $\sigma_p^2 = \frac{1}{\sum_{p=0}^{P-1} e^{-4\frac{p}{P}}} e^{-4\frac{p}{P}},\ 0 \leq p \leq P-1$ with unit average channel energy. The modulation scheme for OFDM symbols carrying data is Quadrature Phase-Shift Keying (QPSK). The number of samples used for noise variance estimation in (48) is $M = N$.

3.6.1 Performance of Training Block Detection

Performance of the signal detection test in (41) Figure 7 shows a comparison of the theoretical and the simulated results for the signal detection test in (41) with $N = 256$ and $u = -1$. Recall that the value of threshold γ' in (41) depends on CFO, SNR and channel PDP. Therefore, we calculate γ' through (43) for different values of target P_{FA}, SNR, and the aforementioned PDP with two cases for CFO. In the first case, we calculate γ' for $f = 0$ and simulate without CFO as the ideal benchmark. In the second case, we calculate γ' for a CFO of 0.5 while in simulation, CFO is chosen randomly from $[-f_{\max}, f_{\max}]$ for each iteration. As γ' is independent of

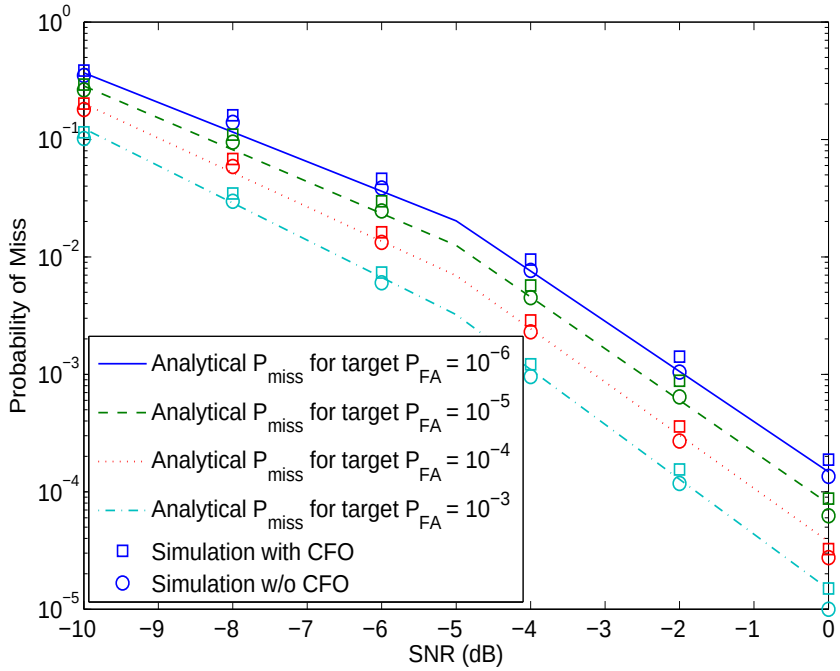

Figure 7: Comparison of simulated and analytical P_{MISS} for different target P_{FA} values for the proposed training block detection test; $N = 256$, $N_{\text{g}} = 32$, and $u = -1$.

integer CFOs, 0.5 is chosen as the worst case value for non-zero f_{F}. The probability of miss is calculated through simulations for each case and compared against the analytical values. As expected, a lower value of target P_{FA} results in a higher P_{MISS}. As shown in Figure 7, the simulated points match well with the theoretical curves for zero CFO case. Moreover, the performance of non-zero CFO is very close to the zero CFO case. The slight degradation in the non-zero CFO case is because of the independence assumption made during the design of NP test in Section 3.4.

Performance of the Simplified NP Test in (47) We now compare the performance of the original test in (41) and the simplified NP test in (47). Recall that the calculation of γ' in (46) for simplified NP test is independent of the CFO, channel PDP and noise variance. Hence, the value of γ' for simplified NP test changes only with the target P_{FA}. However, both tests require knowledge of the noise variance.

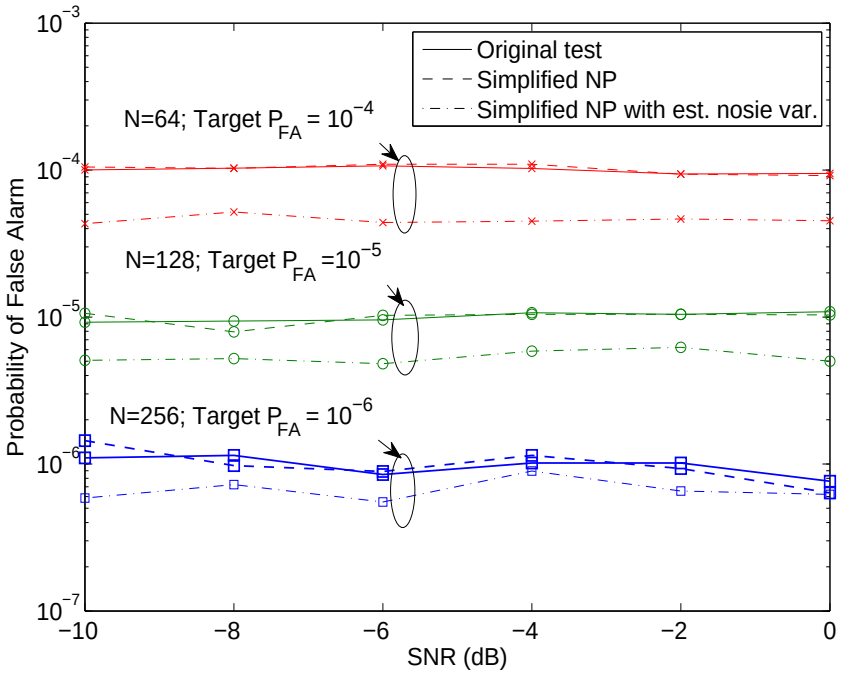

Figure 8: Comparison of simulated P_{FA} of the original NP test, simplified NP test, and simplified NP test with noise variance estimation for different values of N and target P_{FA}.

Figure 8 shows the P_{FA} obtained from simulations using γ' designed for different combinations of target P_{FA} values and the length N of the ZC sequence. For the simplified NP test, we present the performance both with perfect knowledge of noise variance and with its estimated value using (48). As shown, both original and simplified NP tests perform very close to the target P_{FA} for each value of SNR. Also the performance difference between the two tests is minimal when both test use ideal values of noise variance. However, the performance of simplified NP test with estimated noise variance is better than the target P_{FA} as compared to the perfect knowledge case. The gap between the performance of simplified NP test with and without perfect knowledge of noise variance decreases as the value of N increases because of increased noise variance estimation accuracy as $M = N$.

Figure 9 shows the performance comparison in terms of P_{MISS} for different combinations of target P_{FA} values and the length N of the ZC sequence. It also shows the

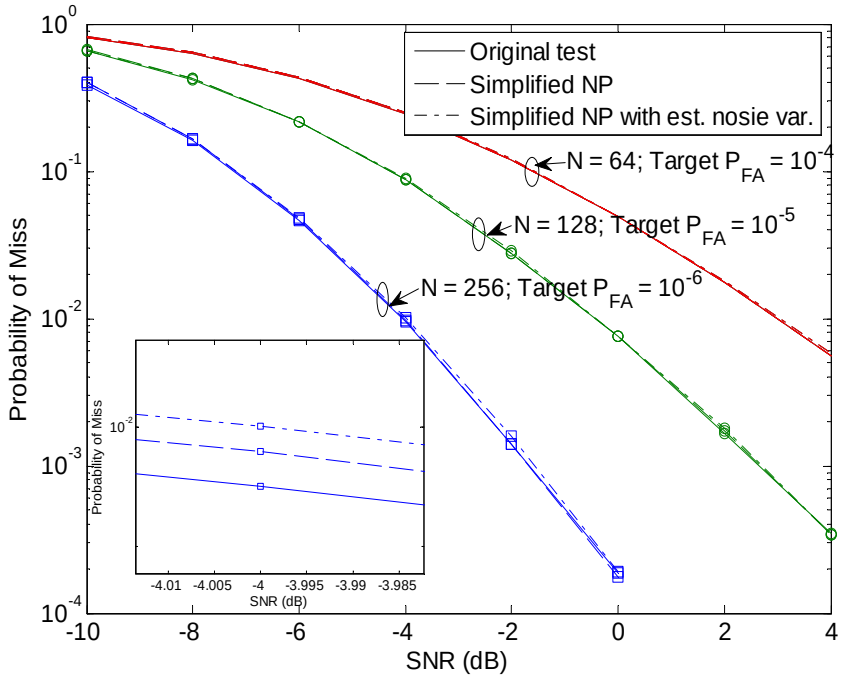

Figure 9: Comparison of simulated P_{MISS} of the original NP test, simplified NP test, and simplified NP test with noise variance estimation for different values of N and target P_{FA}.

zoomed-in performance at SNR of -4 dB for $N = 256$ case. Again, the original test assumes perfect knowledge of noise variance while the simplified NP test is simulated for both perfect knowledge case and the estimated noise variance case. As shown, the performance of simplified NP test, with and without perfect knowledge of noise variance, is very close to the original test for all values of target P_{FA} and N. The performance of simplified NP test is slightly degraded as compared to the original test. However, the degradation is minimal, which shows that the approximation employed in deriving the simplified NP test in Section 3.4.2, i.e., $\sigma^2_{\tilde{w}} \ll \sigma^2_k$ has negligible effect on its performance. Also the performance of simplified NP test with estimated noise variance is further degraded as compared to the perfect knowledge case, as shown in the magnified sub-figure. However, this performance degradation in P_{MISS} also provides an improvement in P_{FA} as discussed earlier for Figure 8.

Figure 10 presents the performance comparison, in terms of P_{MISS}, of simplified

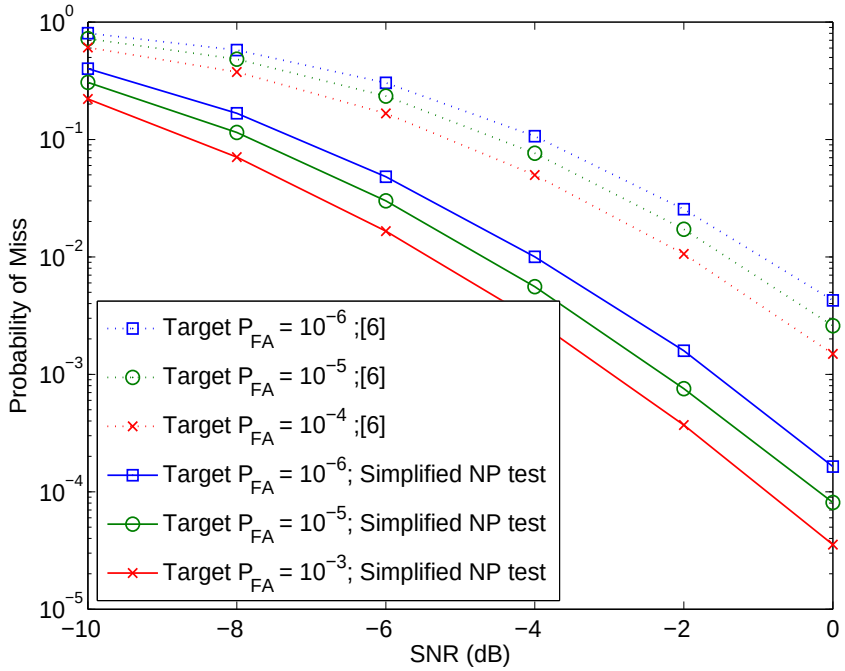

Figure 10: Comparison of simulated P_{MISS} of the simplified NP test, and [49] for different target P_{FA} values; $N = 256$, $N_{\text{g}} = 32$, and $u = -1$.

NP test with estimated noise variance against the signal detection algorithm in [49] for $N = 256$ and different values of target P_{FA}. As shown, the performance of simplified NP test exhibits a considerable improvement in performance as compared to [49]. These results show that the proposed signal detection schemes are indeed robust to large values of CFOs and the detection performance is superior to the schemes proposed in the literature. Moreover, the simplified NP test results in negligible performance degradation as compared to the original test. Hence, we will use only simplified NP test and its corresponding γ' values for the following simulation results.

3.6.2 Performance of Timing Synchronization

In Figure 11, we present the performance of proposed coarse timing synchronization in terms of mean absolute TO estimation error using the proposed simplified NP test. The value of γ' for the proposed test is designed for a target P_{FA} of 10^{-6} and the performance is evaluated, with and without the integer offset correction in (57),

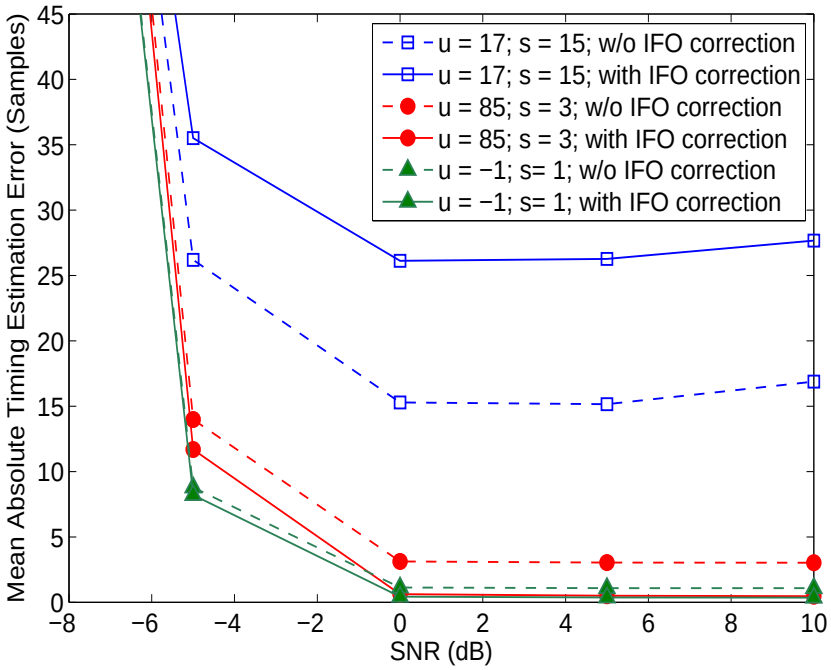

Figure 11: Performance of coarse TO estimation using the proposed algorithm for different values of root index u.

for three different root indices that are $u = -1, 85$, and 17, which result in $s = 1, 3$, and 15 samples, respectively. As $sf_{\max} = 30$ for $u = 17$, the TO estimates do not always lie in the ISI-free region. Thus, $u = 17$ is not a reasonable choice for the aforementioned system parameters and poor performance is expected in this case. On the other hand, both $u = -1$ and 85 are good choices. As shown in Figure 11, without integer-offset-based correction, both $s = 1$ and 3 show a bias in TO estimation. However, integer-offset-based correction removes the bias in both cases while $u = -1$ with a smaller value of s offers better performance for lower SNRs. The performance for $u = 17$, both with and without IFO-based correction, is poor as expected.

In Figure 12, we compare the performance of the proposed algorithms with the timing synchronization methods in [3, 49, 57, 63, 67, 81]. As the timing metric for [67]

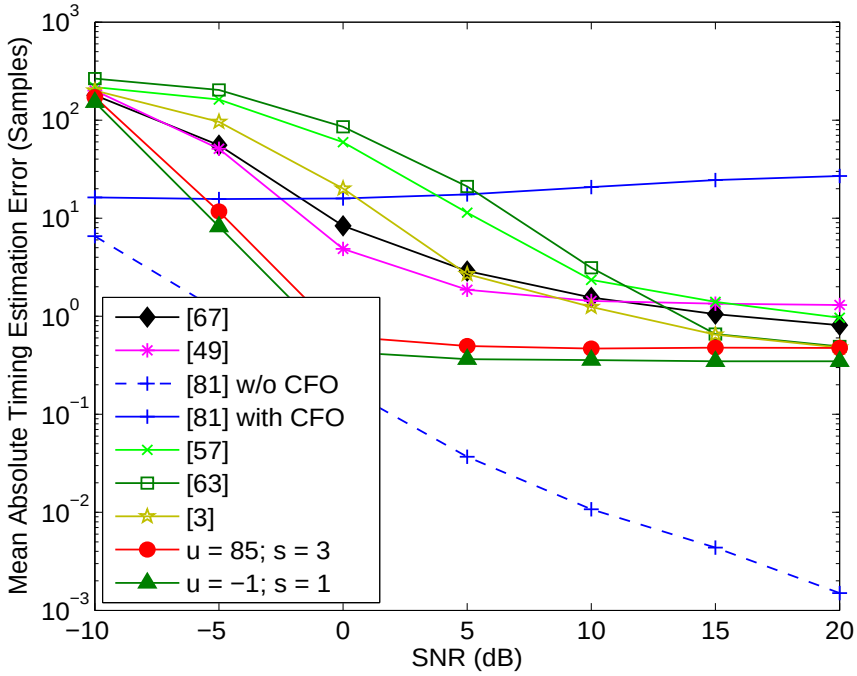

Figure 12: Performance of the proposed TO estimation compared with existing schemes.

shows a plateau, which causes ambiguity in TO estimation, we apply a moving average window equal to the size of the plateau in order to improve the TO estimate. As shown, the proposed algorithm for feasible root indices offers a significant improvement in performance specially for lower SNRs, which shows the effectiveness of the proposed algorithm. When simulating fine timing estimation in [81], we assume that the receiver already knows the coarse timing estimate and the cross-correlation region for all SNR values. Thus, the performance of [81] without CFO outperforms the proposed methods. However, in the presence of CFO, the performance degrades severely, which shows that the algorithm is not robust to CFOs. The schemes in [3, 57, 63] provide a sharp peak in timing metrics for flat fading channels but for multi-path channels, the performance degrades.

3.6.3 Performance of CFO Estimation

In Figure 13, we present the performance of coarse CFO estimation, in terms of mean square error (MSE) of CFO estimation $\left(E\left[|f-\hat{f}|^2\right]\right)$, using the proposed algorithm and its comparison with the coarse CFO estimation in [49, 52, 67]. The values of root indices used in the simulation are the same as the ones in Section 3.6.2. We also plot the modified Cramer-Rao bound (MCRB) [20] as an absolute reference for CFO estimation. As shown, in addition to better coarse TO estimation, root indices -1 and 85 also result in better CFO estimation performance. Moreover, the MSEs for $u = -1$ and 85 are better than the CFO estimation proposed in [49, 52, 67], particularly for lower SNRs and the performance is closer to MCRB as the SNR increases. The CFO estimation in [49], showing an error floor for high SNR values, requires fine CFO estimation for further performance improvement. The performance for infeasible root index $u = 17$ again suffers a high error floor similar to its TO estimation performance. This is because the performance of CFO estimation in Section 3.5 depends on successful TO estimation. Integer CFO estimation in (56) requires a TO estimate within the ISI-free region while the performance of fractional CFO estimation in (51) degrades with deviation of TO estimate from the ideal starting point. As $u = 17$ results in $s = 15$, the TO estimate does not always lie in the ISI-free region and therefore, CFO estimation performance for $u = 17$ exhibits an error floor.

3.6.4 Performance Comparison in Terms of Bit Error Rate

Figure 14 shows the comparison of the proposed synchronization scheme with the methods proposed in [49, 67] in terms of bit error-rate (BER). We simulate four different feasible root indices $u = -1, 85, 51$, and 73 with $s = 1, 3, 5$, and 7, respectively. The maximum deviation from the ideal TO estimate is 14 samples for $u = 73$ with $s = 7$ and $f_{\max} = 2$, which is still within the ISI-free region. We also show the BER performance of the system with ideal synchronization, which implies that the receiver

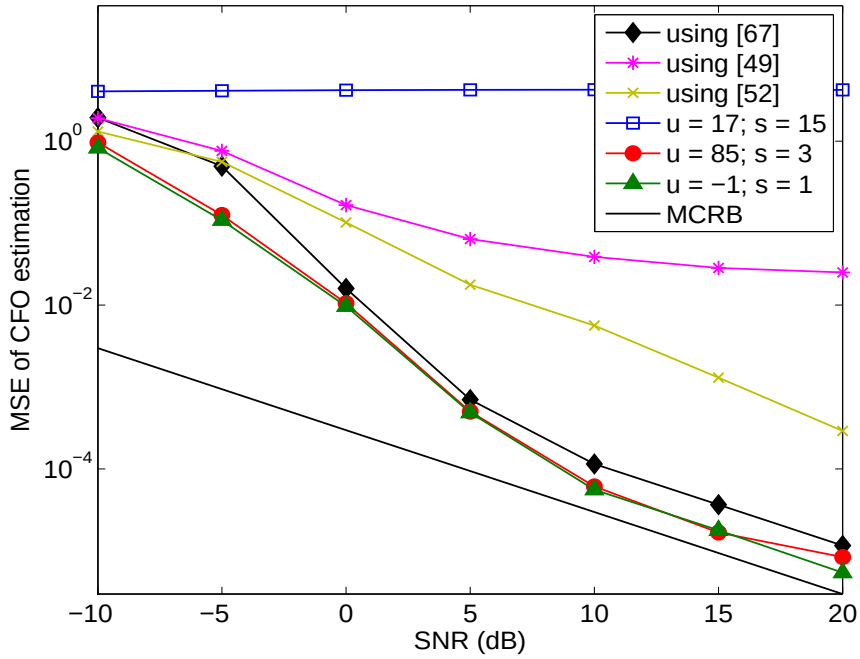

Figure 13: Performance of CFO estimation using the proposed algorithm for different values of root index u.

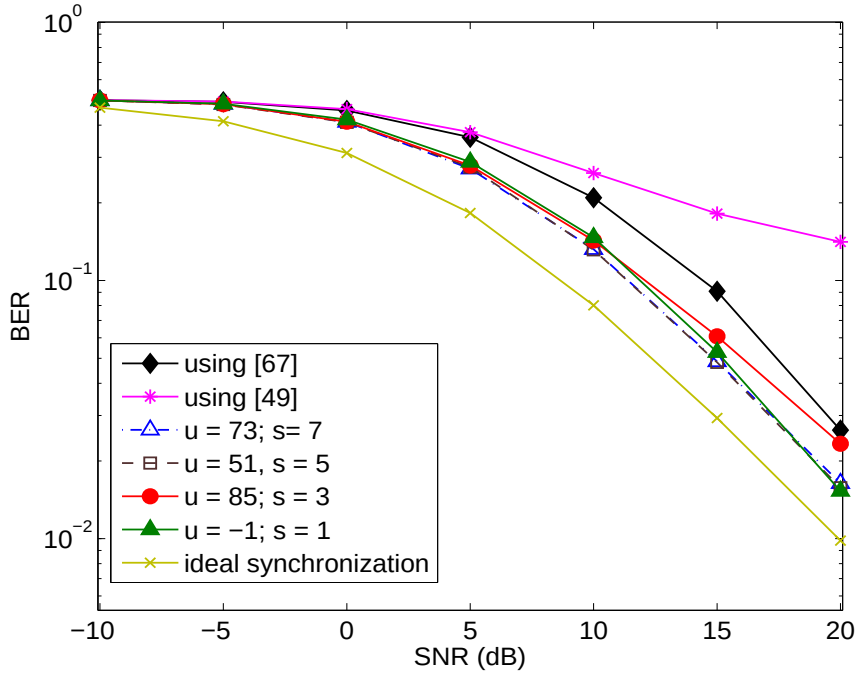

Figure 14: Bit error rate performance of the proposed algorithm for different values of root index u.

has the exact knowledge of the TO and the CFO. As shown, the performance of the proposed training block is similar for all feasible root indices and it is also significantly better than the performance of [49, 67] .

The simulation results show the effectiveness of the proposed algorithms for detection, timing, and frequency synchronization. It shows that if the root indices of the ZC sequences are carefully chosen according to (22), cross-correlation-based timing synchronization achieves robustness to integer CFOs and offers considerable improvements specially in lower SNR regimes.

CHAPTER IV

FREQUENCY SYNCHRONIZATION FOR DOWNLINK COORDINATED MULTI-POINT TRANSMISSIONS

This chapter presents a low-complexity frequency synchronization technique for DL CoMP OFDM transmissions employing ZC sequences as training symbols. The analysis in Chapter 3 has shown that the timing synchronization employing ZC sequences is sensitive to CFOs. Specifically, with non-zero CFO, spurious peaks, in the cross-correlation of the received training symbol with a local copy of the ZC sequence, are observed in addition to the correct peaks. The location of these spurious peaks, also referred as the *leakage* in the cross-correlation, is dependent on the ZC sequence parameters and the CFO. In this chapter, we exploit the properties of ZC sequences, along with this sensitivity to CFOs, to design training signals that allow a simple strategy to decouple different BSs' cross-correlation samples and perform CFO estimation for each BS. The resulting algorithm can be efficiently implemented using fast Fourier transform (FFT) operations, and comparisons with the existing schemes in the literature reveal that the proposed algorithm offers lower complexity and better performance. We also present the hardware implementation details of the proposed algorithm and the corresponding real-time performance measurements.

4.1 Training Signal Structure

We consider the base-band equivalent system model of DL CoMP OFDM transmissions as discussed in Section 2.1.5, where B base-stations transmit simultaneously to a MU. To facilitate synchronization, each BS transmits a training symbol as a preamble containing a ZC sequence with a CP and a CS of N_{g} samples each. The n^{th}

sample of the b^{th} BS's training symbol is given as

$$x_b[n] = e^{j\frac{\pi}{N}u(n-N_g-b\alpha)^2} \quad 0 \leq n \leq N_t - 1. \tag{58}$$

where N is the length of the ZC sequence, u is the root index, which should be relatively prime to N [16], and $N_t = N + 2N_g$ is the total number of samples in the training symbol. The samples of $x[n]$ for $0 \leq n \leq N_g - 1$ comprise the CP while $N + N_g \leq n \leq N_t - 1$ denote the CS. As the ZC sequence is periodic with period N, Eq. (58) indicates that the ZC sequence transmitted by the b^{th} BS is circularly shifted by $b\alpha$ samples, and the ZC sequence with no circular shift ($b = 0$) is denoted as the primary ZC sequence.

It is assumed that the BSs are sufficiently time synchronized, as explained in Section 2.1.5, so that the TO of each BS can be included in its effective CIR. Thus, the signal received at the MU is given as

$$y[n] = \sum_{b=0}^{B-1} e^{j\frac{2\pi}{N}f_b n} \sum_{p=0}^{P-1} h_b[p]x_b[n-p] + w[n], \tag{59}$$

where f_b is the CFO between the b^{th} BS and the MU, and $w[n]$ denotes the n^{th} AWGN sample. We first describe the CFO estimation algorithm for one BS and then extend it to the multiple BSs case.

4.2 CFO Estimation for Single Base-Station

In this section, we assume that $B = 1$ and, without loss of generality, $b = 0$ in (58) for this single BS case. For synchronization, the receiver performs a cross-correlation of the received training symbol with the local copy of the primary ZC sequence. The sample of cross-correlation for a lag l is given as

$$\begin{aligned} r[l] &= \frac{1}{N}\sum_{n=0}^{N-1} y[n+l]x^*[n] \\ &= \frac{1}{N}\sum_{n=0}^{N-1}\left(e^{j\frac{2\pi}{N}f_0(n+l)}\sum_{p=0}^{P-1} h_0[p]x_0[n+l-p] + w[n+l]\right)e^{-j\frac{\pi}{N}un^2}. \end{aligned} \tag{60}$$

Due to the presence of CP and CS, linear cross-correlation in (60) is similar to circular cross-correlation in the *circular correlation region* defined as $R_{cc} := \{0 \leq l \leq 2N_{\mathrm{g}}-1\}$. Within R_{cc}, $r[l]$ is given as

$$\begin{aligned} r[l] &= \frac{1}{N}\sum_{n=0}^{N-1}\left(e^{j\frac{2\pi}{N}f_0(n+l)}\sum_{p=0}^{P-1}h_0[p]e^{j\frac{\pi}{N}u(n+l-p-N_{\mathrm{g}})^2}+w[n+l]\right)e^{-j\frac{\pi}{N}un^2} \quad 0 \leq l \leq 2N_{\mathrm{g}} \\ &= \frac{1}{N}e^{j\frac{2\pi}{N}f_0 l}\sum_{p=0}^{P-1}e^{j\frac{\pi}{N}u(l-p-N_{\mathrm{g}})^2}\left(\sum_{n=0}^{N-1}h_0[p]e^{j\frac{2\pi}{N}(u(l-p-N_{\mathrm{g}})+f_0)n}\right)+\sum_{n=0}^{N-1}w[n+l]e^{-j\frac{\pi}{N}un^2}. \end{aligned} \tag{61}$$

For $f_0 = 0$, (61) simplifies to

$$r[l] = e^{j\frac{2\pi}{N}f_0 l}\sum_{p=0}^{P-1}h_0[p]\delta(l-p-N_{\mathrm{g}})+\sum_{n=0}^{N-1}w[n+l]e^{-j\frac{\pi}{N}un^2}. \tag{62}$$

Thus, the cross-correlation provides an estimate of the CIR in the *CIR region* defined as $R_{CIR} := \{N_{\mathrm{g}} \leq l \leq N_{\mathrm{g}}+P-1\} \subseteq R_{cc}$. The rest of the cross-correlation samples in R_{cc} contain only noise. However, for non-zero f_0, the cross-correlation is given as,

$$r[l] = e^{j\frac{2\pi}{N}f_0 l}\sum_{p=0}^{P-1}e^{j\frac{\pi}{N}u(l-p-N_{\mathrm{g}})^2}h_0[p]\Psi\left(u(l-p-N_{\mathrm{g}})+f_0\right)+\sum_{n=0}^{N-1}w[n+l]e^{-j\frac{\pi}{N}un^2}, \tag{63}$$

with

$$\Psi\left(u(l-p-N_{\mathrm{g}})+f_0\right) = e^{-j\pi\frac{N-1}{N}(u(l-d-N_{\mathrm{g}})+f_0)}\frac{1}{N}\frac{\sin\pi\left(u(l-p-N_{\mathrm{g}})+f_0\right)}{\sin\frac{\pi}{N}\left(u(l-p-N_{\mathrm{g}})+f_0\right)}. \tag{64}$$

$\Psi(\cdot)$ is a $\frac{\mathrm{sinc}}{\mathrm{sinc}}$ function periodic with period N, whose magnitude is maximum (equal to 1) in the center of its main lobe and decreases as a sample away from the center of a lobe is obtained. A sample close to the center of the main lobe is obtained when

$$u(l-p-N_{\mathrm{g}})+f_0 \approx mN \tag{65}$$

where m is any integer. For $f_0 = 0$, the condition in (65) is satisfied with equality only when $l = p+N_{\mathrm{g}}$ with $m = 0$, irrespective of the value of u, and the center of the main lobe is sampled with $\Psi(0) = 1$. Moreover, the value of $\Psi(u(l-d-N_{\mathrm{g}}))$ for

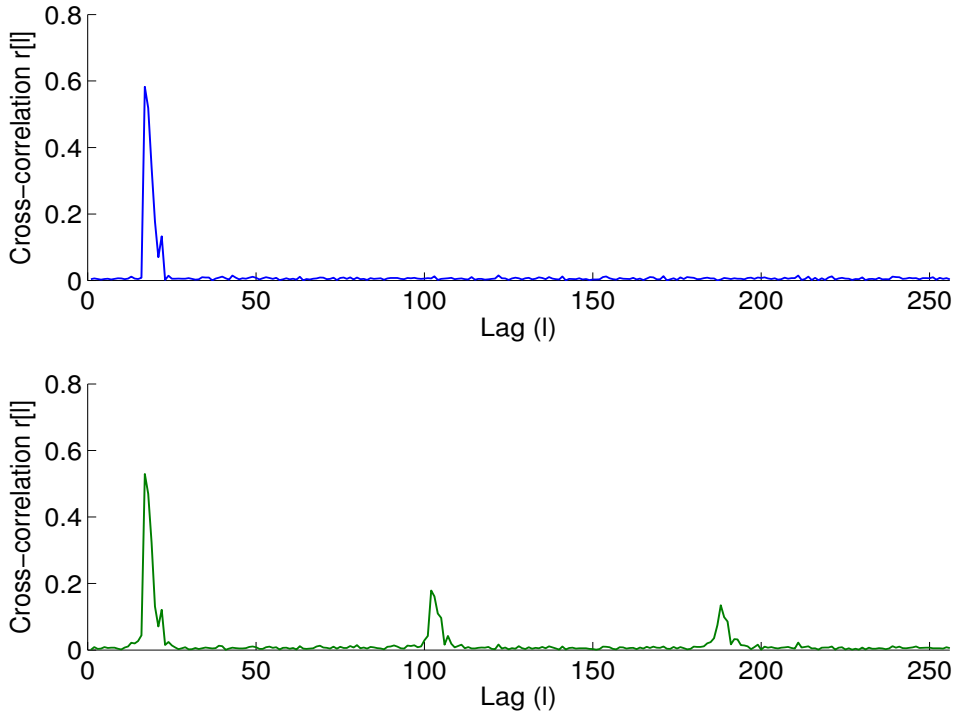

Figure 15: Cross-correlation without CFO (top figure) and with a CFO of 0.2 (bottom figure) showing the CIR region and the leakage regions.

$l-p-N_{\mathrm{g}} \neq 0$, is zero as the nulls of side lobes of $\Psi(\cdot)$ get sampled. Thus, significant cross-correlation values or peaks are obtained corresponding to the channel taps as in (62), for $l \in R_{CIR}$ while the cross-correlation for lags $l \in \{R_{cc} \setminus R_{CIR}\}$ contains only noise samples. However, for non-zero f_0, the magnitude of cross-correlation in the CIR region decreases as $|\Psi\left(u(l-p-N_{\mathrm{g}})+f_0\right)|_{l=p+N_{\mathrm{g}}} = |\Psi(f_0)| < 1$ and a sample away from the center of the main lobe in obtained. However, it is important to note that for non-zero f_0, the condition in (65) may also get satisfied for cross-correlation indices not in the CIR region, as side lobes get sampled. We denote the set of all such indices as the *leakage region* (R_L). The indices in the leakage region depend on the value of the root index.

Proposition 3: A root index u results in $T = |u| - 1$ leakage regions with t^{th} leakage region at $R_t := \{(N_{\mathrm{g}} + ts)_N \leq l \leq (N_{\mathrm{g}} + ts + P - 1)_N\}$, $t = 1, \cdots, T$ where s is the value satisfying $us + 1 = mN$, and m is any integer.

Proof: See appendix C.

We denote

$$R_L := \bigcup_{t=1}^{|u|-1} R_t \tag{66}$$

as the union of all leakage regions. Moreover, the distance of the leakage region, closest to the CIR region is denoted as

$$s_{\min} = \min_t \{(ts)_N\}, \tag{67}$$

which plays an important role in the proposed algorithm. As an example, $N = 256$ and $u = 3$ results in $T = 2$ leakage regions for non-zero CFO with $s = s_{\min} = 85$ and $m = 1$. An example of cross-correlation values obtained with and without a CFO of 0.2 and the above mentioned system parameters is shown in Figure 15 for an SNR of 20 dB, $N_{\mathrm{g}} = 16$, and a multi-path channel with 6 taps and an exponential PDP. As shown in the figure, the cross-correlation samples give the CIR estimate in the CIR region starting at $l = N_{\mathrm{g}} = 16$ when $f = 0$. However, two leakage regions appears with starting indices at $(N_{\mathrm{g}} + ts)_N = 101, 186$ for $f = 0.2$.

The discussion above shows that, for non-zero f_0, the magnitude of cross-correlation samples decreases in the CIR region while spurious peaks start appearing in leakage regions whose number and location depends on the value of the root index. Thus, the idea of the proposed CFO estimation is as follows: we choose the value of the root index of the ZC sequence such that the CIR region and the leakage regions are mutually exclusive ($R_{CIR} \cap R_L = \phi$ where ϕ denotes the empty set), and we pre-compensate the received training signal with a candidate CFO value prior to computing cross-correlation. In a noise-free environment, if the candidate CFO value is equal to the true CFO value, the magnitude of cross-correlation in the CIR region is maximum while it is zero in the leakage region. Thus, the CFO can be estimated as the candidate value which maximizes the ratio of the energy of cross-correlation samples in the CIR region to the energy of the cross-correlation samples in the leakage region.

Specifically, the cross-correlation with a candidate CFO value f_c is given as

$$r_{f_c}[l] = \frac{1}{N} \sum_{n=0}^{N-1} e^{-j\frac{2\pi}{N} f_c n} y[n+l] x^*[n], \tag{68}$$

a cost function corresponding to the candidate value is formed as

$$J_{f_c} = \frac{\sum_{l \in R_{CIR}} |r_{f_c}[l]|^2}{\sum_{l \in R_L} |r_{f_c}[l]|^2}, \tag{69}$$

and the CFO is estimated as

$$f_b = \arg\max_{f_c} J(f_c). \tag{70}$$

The proposed algorithm only requires an estimate of the coarse timing and the value of P, which can be derived from system parameters. As an added advantage, the cross-correlation samples in R_{CIR} for the CFO estimate also provide an estimate of the CIR. However, Eq. (68-70) imply that the proposed CFO estimation scheme has two drawbacks. First, the proposed algorithm is computationally complex. The number of leakage regions is dependent on the value of u and a higher value of u increases the number of leakage regions thereby increasing the computational complexity of (69). Second, the training symbol contains the extra overhead of CS in addition to the CP, and the length of CP and CS should be long enough so that $R_L \cup R_{CIR} \subseteq R_{cc}$, which decreases the spectral efficiency of the system. We address these shortcomings later in Section 4.4.

4.3 CFO Estimation for Multiple Base-Stations

In this section, we discuss the extension of the proposed CFO estimation algorithm to the multiple BS case, i.e., when $B > 1$. Recall from (58) that the b^{th} BS transmits a ZC sequence with a circular shift of $b\alpha$ samples. Thus the cross-correlation in (61)

becomes

$$r[l] = \frac{1}{N}\sum_{b=0}^{B-1} e^{j\frac{2\pi}{N}f_b l}\sum_{p=0}^{P-1} e^{j\frac{\pi}{N}u(l-p-N_g-b\alpha)^2}\left(\sum_{n=0}^{N-1} h_b[p]e^{j\frac{2\pi}{N}(u(l-p-N_g-b\alpha)+f_b)n}\right) + \sum_{n=0}^{N-1} w[n+l]e^{-j\frac{\pi}{N}un^2}. \quad (71)$$

If $f_b = 0$ for all BSs, (71) simplifies to,

$$r[l] = e^{j\frac{2\pi}{N}f_0 l}\sum_{p=0}^{P-1} h_b[p]\delta(l-p-N_g-b\alpha) + \sum_{n=0}^{N-1} w[n+l]e^{-j\frac{\pi}{N}un^2}, \quad (72)$$

which implies that the CIR region of b^{th} BS (denoted as R^b_{CIR}) is given as $R^b_{CIR} := \{N_g + b\alpha \leq l \leq N_g + b\alpha + P - 1\}$, i.e., a circular shift of $b\alpha$ samples with respect to (w.r.t.) R^0_{CIR}. Similarly, the indices of leakage region of the b^{th} BS (R^b_L) also shift circularly by $b\alpha$ samples w.r.t. R^0_L. Therefore,

$$R^b_L = \bigcup_{t=1}^{T} R^b_t \text{ with } R^b_t := \{(N_g + ts + b\alpha)_N, \ldots, (N_g + ts + b\alpha + P - 1)_N\}. \quad (73)$$

In order to apply the CFO estimation algorithm proposed in Section 4.2 to the multiple BS case, we need to de-couple the CIR and leakage regions corresponding to each BS. If we can choose u and α parameters of the training signal in (58) such that

$$\bigcap_{b=0}^{B-1} R^b_{CIR} = \phi, \quad (74)$$

and

$$\bigcap_{b=0}^{B-1} R^b_L = \phi, \quad (75)$$

the algorithm proposed in Section 4.2 can still be applied to estimate the CFO of each BS separately. Thus, r_{f_c} in (68) is calculated once for each value of f_c, and the cost function of b^{th} BS ($J_b(f_c)$) is formed by taking the cross-correlation values in R^b_{CIR} and R^b_L. Hence, a single line-search provides the CFO estimates of all BSs.

4.3.1 Parameter Selection for the Training Signal

The selection of appropriate u and α in (58) satisfying (74) and (75) can be posed as the following problem:

Given system parameters N, P and $B > 1$

$$\begin{aligned} &\text{choose} && u, \alpha \\ &\text{such that} && \gcd(u, N) = 1 && \text{(i)} \\ & && P < s_{\min} < N && \text{(ii)} \\ & && P < \alpha < N && \text{(iii)} \\ & && B\alpha < s_{\min} < N && \text{(iv)}, \end{aligned}$$

where $\gcd(\cdot)$ stands for the greatest common divisor, and $s_{\min}$, given in (67), is dependent on u. Condition (i) requires u to be relatively prime to N as per definition of ZC sequence. Condition (ii) ensures that $R^b_{CIR} \cap R^b_L = \phi \; \forall b$. Condition (iii) ensures that $R^b_{CIR} \cap R^{b'}_{CIR} = \phi$ for $b \neq b'$, while the Condition (iv) ensures that $R^b_{CIR} \cap R^{b'}_L = \phi$ for $b \neq b'$. These conditions can be solved to derive appropriate parameters of training signal in (58). From proposition 3, it is clear that a small value of u results in less number of leakage regions, reducing the computational complexity, and a larger values of $s_{\min}$, increasing the number of BSs ($B_{\max}$) that can be supported by the proposed algorithm for a given value of P. Specifically,

$$B_{\max} = \left\lfloor \frac{s_{\min}}{P+1} \right\rfloor. \tag{76}$$

For example, with $N = 256$ and $P = 15$, $u = 5$ results in $s_{\min} = 51$. In order to maximize the value of B, α can be chosen as 16, which satisfies the constraints above and results in $B_{\max} = 3$ BSs. On the other hand, $u = 3$ results in $s_{\min} = 85$, which implies that $\alpha = 16$ can support $B_{\max} = 5$ BSs. For $B < B_{\max}$, several choices for α exist. For $B = 2$, α can assume any value between 16 to 42 to satisfy the above constraints, whereas for $B = 3$, α can assume any value between 16 to 28. In order to minimize the IBI, the best α values, denoted as α^* will be the one, which maximizes

Length N	root index u	$s_{\min}$
64	3,5,7	21,13,9
128	3,5,7	43,25,18
256	3,5,7	85,51,36
512	3,5,7	171,103,73
1024	3,5,7	341,205,146

Table 2: Values of root indices and corresponding $s_{\min}$ for different lengths of Zadoff-Chu sequences.

the distance between CIR and leakage regions of different BSs, given as,

$$\alpha^* = \left\lfloor \frac{s_{\min}}{B} \right\rfloor. \tag{77}$$

We enlist some values of u and corresponding s_{min} for different values of length of ZC sequence N in Table 2.

Training Signal Design for ZC Sequences defined in the Sub-carrier Domain: ZC sequences can also be defined in the sub-carrier domain. For example, the PSS in LTE DL transmissions contains ZC sequences modulated on the middle 63 sub-carriers around the DC sub-carrier. If a ZC sequence, with root index u_f, modulates $M < N$ middle sub-carriers around DC sub-carrier, the condition in (65) for cross-correlation of the received training signal with the local copy of a ZC sequence modifies to

$$l - N_{\mathrm{g}} - p - \frac{N}{M} u_f f_b = mN, \tag{78}$$

as shown in Section 3.3.3. This condition is in fact equivalent to (65) as,

$$l - N_{\mathrm{g}} - p - \frac{N}{M} u_f f_b = mN \Leftrightarrow u_f^{-1}(l - N_{\mathrm{g}} - p) - \frac{N}{M} f_b = m u_f^{-1} N \tag{79}$$

where u_f^{-1} is the modular inverse of u_f, i.e., $(u_f u_f^{-1})_N = 1$, and the fact that the DFT of a ZC sequence with root index u_f is another ZC sequence with root index u_f^{-1} [59]. However, the cross-correlation in this case, is over sampled by a factor of $\frac{N}{M}$, which implies that the CIR region does not give an estimate of the CIR for $f_b = 0$.

However, if the received signal is down-sampled by a factor of $\frac{N}{M}$ before computing cross-correlation, the analysis is still applicable with N replaced by M and u replaced by u_f^{-1} in (65).

4.4 Low Complexity CFO Estimation

The complexity of CFO estimation in (68 - 70) is very high due to computation of cross-correlation for each candidate CFO value. We measure the computational complexity in terms of number of complex multiplication required for CFO estimation. For each candidate CFO value, computation of r_{f_c} in (68) requires $NB(|R^b_{CIR}|+|R^b_L|)$ complex multiplications. If the total number of candidate CFO values are N_i, the total cost of the line search-based CFO estimation is

$$N_i \left(B(|R^b_{CIR}| + |R^b_L|)(N+1)\right) = N_i B|u|P(N+1) \tag{80}$$

complex multiplications. In addition, the algorithm requires the inclusion of CS in addition to the CP to transform linear cross-correlation into circular cross-correlation, which increases the training overhead. We now discuss some manipulations to show how the algorithm can be modified to lower the complexity and exclude the need for CS.

4.4.1 FFT-based Implementation

As mentioned in Section 2.1.4, a user must be synchronized to a serving BS before entering into CoMP mode and all BSs signals must be received within ISI-free region. Thus, if timing synchronization corresponding to the serving BS has already been performed, the receiver has an estimate of the symbol boundaries of the received training symbol and circular cross-correlation can instead be performed as

$$\mathbf{r}_{f_c} = \mathbf{X}_c \mathbf{D}_N(f_c)\mathbf{y} \tag{81}$$

where $\mathbf{r}_{f_c} = [r_{f_c}(0), \cdots, r_{f_c}(N-1)]^T$, $\mathbf{X}_c$ is an $N \times N$ circulant matrix with the primary ZC sequence $[1, e^{j\frac{\pi}{N}u}, \cdots, e^{j\frac{\pi}{N}u(N-1)^2}]$ as its first row, $\mathbf{D}_N(f_c)$ is an $N \times N$ diagonal

matrix with $[\mathbf{D}_N(f_c)]_{nn} = e^{-j\frac{2\pi}{N}f_c n}$, $0 \leq n \leq N-1$, and $\mathbf{y} = [y[0], \cdots, y[N-1]]^T$ is the received training symbol. In Eq. (81), explicit circular cross-correlation is computed by circularly shifting the samples of the local copy instead of taking advantage of the circular symmetry of the training signal due to CP and CS. Thus, the CS is not needed in this case, improving the spectral efficiency. However, CP is still needed to avoid ISI in case that the training symbol is transmitted as a midamble or if the CP is used for timing synchronization [79]. Following (81), the cost function for CFO estimation for b^{th} BS can also be expressed in matrix form as,

$$J_b(f_c) = \frac{(\mathbf{C}_b\mathbf{r}_{f_c})^H\mathbf{C}_b\mathbf{r}_{f_c}}{(\mathbf{L}_b\mathbf{r}_{f_c})^H\mathbf{L}_b\mathbf{r}_{f_c}}, \tag{82}$$

where $\mathbf{C}_b(\mathbf{L}_b)$ is an $N \times N$ diagonal matrix whose n^{th} element is unity if $n \in R^b_{CIR}(R^b_L)$ and zero otherwise. As circular correlation in time domain is point-by-point multiplication in frequency domain, DFT can also be used to compute $\mathbf{r}_{f_c}$ in (81). Specifically,

$$\mathbf{r}_{f_c} = \mathbf{F}^H\mathbf{D}_N(\mathbf{X})\mathbf{F}\mathbf{D}_N(f_c)\mathbf{y} \tag{83}$$

where $\mathbf{F}$ is the $N \times N$ DFT matrix, $\mathbf{D}_N(\mathbf{X})$ is an $N \times N$ diagonal matrix containing the DFT of the conjugate of the primary ZC sequence on its diagonal. As DFT can be efficiently computed through FFT, the complexity of FFT-based implementation is much lower than (81). Assuming $\mathbf{D}_N(\mathbf{X})$ can be calculated off-line, the computational complexity of the FFT-based line search is

$$N_i\left(2N + 2N\log_2(N) + B|u|P\right) \tag{84}$$

complex multiplications.

4.4.2 Adaptive Implementation

We now present the adaptive implementation of the proposed CFO estimation based on the gradient descent algorithm [66], in which the CFO of each BS is estimated iteratively as,

$$\hat{f}_b^{i+1} = \hat{f}_b^i - \mu\acute{J}_b(f_c) \tag{85}$$

where $\hat{f}_b^i$ is the CFO estimate of the b^{th} BS at i^{th} iteration, μ is the step-size parameter, and $\acute{J}_b(f_c)$ is the derivative of the cost function given as

$$\acute{J}_b(f_c) = \frac{2\pi}{N} \frac{\Re\left(j\mathbf{f}^H(f_b^i)\mathbf{A}\mathbf{D}_N(n)\mathbf{f}(f_b^i)\right)\mathbf{f}^H(f_b^i)\mathbf{B}\mathbf{f}(f_b^i) - \Re\left(j\mathbf{f}^H(f_b^i)\mathbf{B}\mathbf{D}_N(n)\mathbf{f}(f_b^i)\right)\mathbf{f}^H(f_b^i)\mathbf{A}\mathbf{f}(f_b^i)}{\left(\mathbf{f}^H(f_b^i)\mathbf{B}\mathbf{f}(f_b^i)\right)^2}, \tag{86}$$

where $\mathbf{A} = \mathbf{D}_N^H(\mathbf{y})\mathbf{X}_c^H\mathbf{C}_b^H\mathbf{C}_b\mathbf{X}_c\mathbf{D}_N(\mathbf{y})$, and $\mathbf{B} = \mathbf{D}_N^H(\mathbf{y})\mathbf{X}_c^H\mathbf{L}_b^H\mathbf{L}_b\mathbf{X}_c\mathbf{D}_N(\mathbf{y})$. $\mathbf{f}(f_b^i)$ is an $N \times 1$ vector with $[\mathbf{f}(f_b^i)]_n = e^{j\frac{2\pi}{N}f_b^i n}$, and $\mathbf{D}_N(\mathbf{y})$ is an $N \times N$ diagonal matrix with the received training symbol at the diagonal. If the number of iterations of the gradient descent algorithm is N_{it}, the computational complexity of the adaptive implementation is $2(N^2+N) + BN_{it}(2N^2+N)$ complex multiplications.

We also compare the complexity of the proposed CFO estimation scheme with the algorithms proposed in [39, 75, 90]. The algorithm in [75] is also based on ZC sequences and combines simplified ML CFO estimation with IIC for CFO estimation. Without IIC, it is denoted as RMCE (robust multi-CFO estimation) and with IIC, it is denoted as RMCE-IIC. If the number of iterations of IIC step is N_{IC}, the cost of CFO estimation in [75] is $(N_{IC}+1)(2N+1)N_cBP + 2N_{IC}BNP$ complex multiplications.

The algorithm in [39] is also based on interference cancelation and denoted as PCFE (parallel interference cancelation based channel and frequency estimation). The complexity of PCFE is $NBP + 2N_{IC}(P^2B^2 + BP^2)$ complex multiplications while the complexity of Newton method (NM) for ML CFO estimation in [90] can be approximated as $\mathcal{O}\left(N_i(5B^3N^2P)\right)$.

Figure 16 shows a complexity comparison of the proposed schemes with [39,75,90] against different lengths of the ZC sequence N with $P = \frac{N}{16}$, $u = 3$, $B = 3$ and $N_i = 100$. As shown, the complexity of NM is highest among all the algorithms in consideration due to expensive matrix inversions involved in the algorithm. The complexity of adaptive estimation is highest among the proposed algorithms, while the complexity of adaptive implementation and linear cross-correlation (denoted as

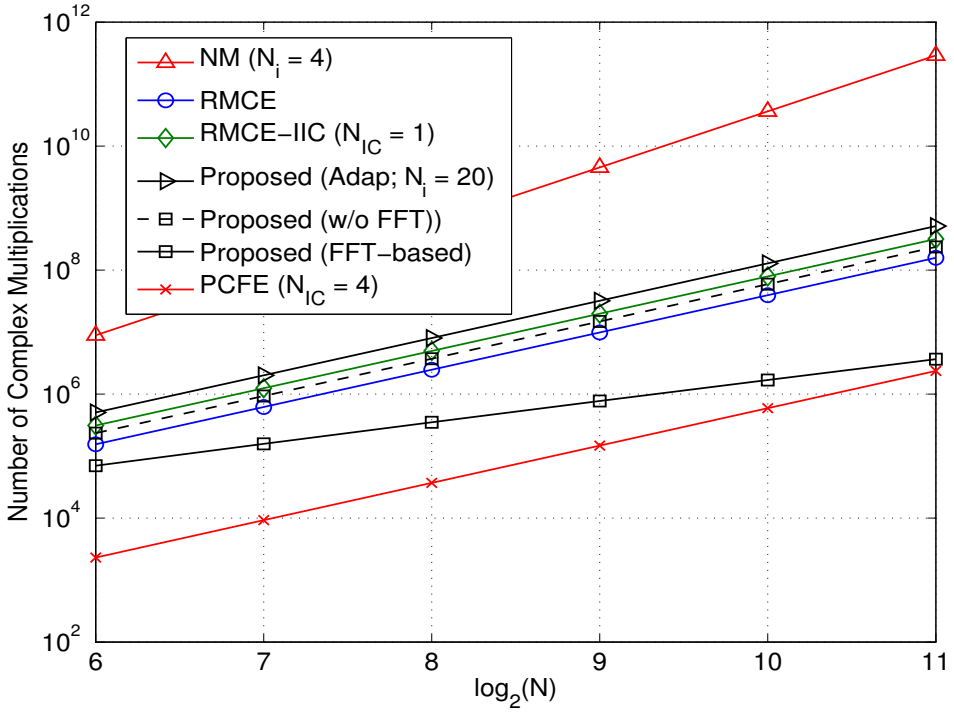

Figure 16: Complexity of the proposed algorithm for different lengths of the ZC sequence.

w/o FFT) in (68 - 70) is comparable to RMCE and RMCE-IIC. Note that $N_{IC} = 1$ for RMCE-IIC and if more IIC steps are added, its complexity will increase even further. The FFT-based implementation has lower complexity than [75, 90] and the other proposed algorithms. PCFE in [39] has lower complexity for smaller values of N but it approaches FFT-based implementation as N increases. However, the lower complexity of PCFE comes at a price of reduced estimation accuracy as shown in Section 4.5.

4.5 Simulation Results

In this section, we present the performance of the proposed CFO estimation scheme in term of MSE of CFO estimation evaluated through Monte Carlo simulations and compare it with some of the existing algorithms. The simulation parameters are as follows: length of ZC sequence $N = 256$, CP length $N_g = 32$, and the sub-carrier spacing of the OFDM system is 15 kHz. The channel is modeled as a Rayleigh fading

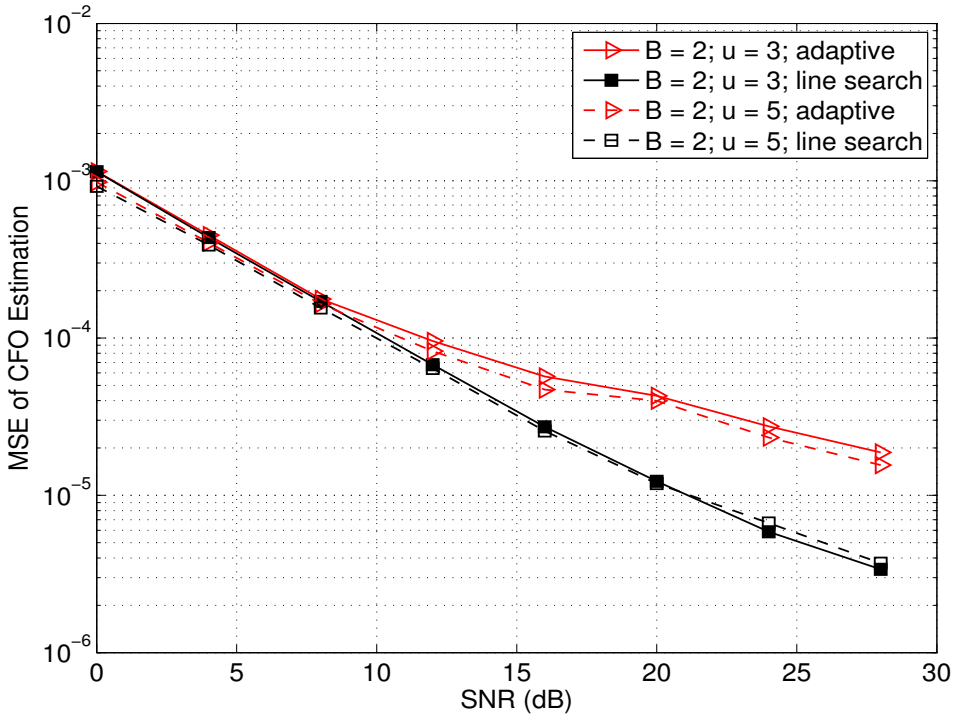

Figure 17: Performance of the proposed algorithms with different parameters of ZC sequence.

channel with PDP taken from the Vehicular-A Channel model [14], which results in $\max_b\{P_b\} = 11$. The maximum TO between BS is taken as $\max_b\{d_b\} = 5$ samples, which implies that $P = 16$. The CFO is modeled as a random variable uniformly distributed from [-0.1,0.1] and the number of candidate CFO values $N_i = 100$. We compare the performance of the proposed schemes with the CoMP CFO estimation algorithms proposed in [39, 75].

4.5.1 Performance of the Proposed Algorithms

Figure 17 shows the performance of FFT-based and adaptive implementations of the proposed algorithm. The number of base-stations is $B = 2$. Two values of root indices $u = 3$ and 5 with $\alpha = 28$ and 21 respectively, are used. $N_i = 20$ iterations of the adaptive implementation are used along with the step size $\mu = 0.001$. As shown, FFT-based implementation has better performance than the adaptive implementation in addition to lower complexity as discussed in Section 4.4. Moroever, the performance

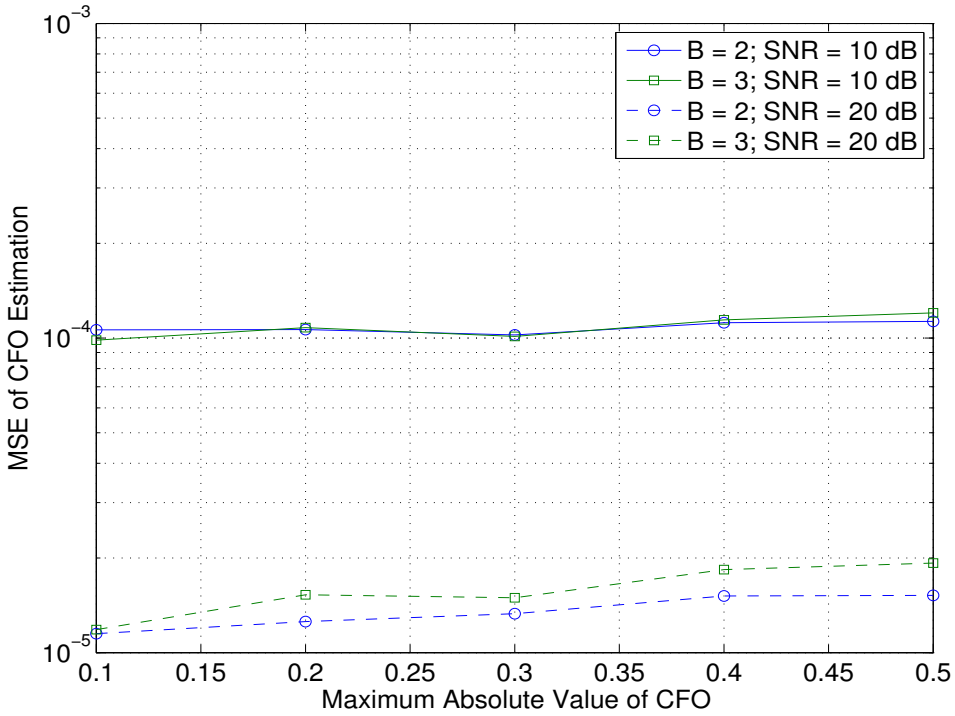

Figure 18: Performance of the proposed algorithm with increasing value of CFO.

of the proposed algorithms for both values of root indices is similar. Hence, in the following simulation results, only FFT-based algorithm is employed.

Figure 18 shows the performance of the proposed algorithm as the maximum absolute value of the CFO changes for $B = 2, 3$ and two values of SNR, i.e., 10 and 20 dB. As shown, the effect of larger CFO on the proposed algorithm is minimal, while the reason for slight degradation in estimation accuracy for higher CFO values is that the number of candidate CFO values for the line search is kept fixed to $N_i = 100$.

4.5.2 Performance Comparison with Existing Algorithms

In this section, we compare the performance of the proposed algorithm with the existing algorithms in the literature including [39, 75]. As the algorithm in [75] is based on ZC sequences, the value of root index used in the simulations of [75] is $u = 3$ along with the optimal circular shifts proposed in [75] for $B = 2, 3$. The value of the root index for the proposed algorithm is also $u = 3$ and the resolution of line search for

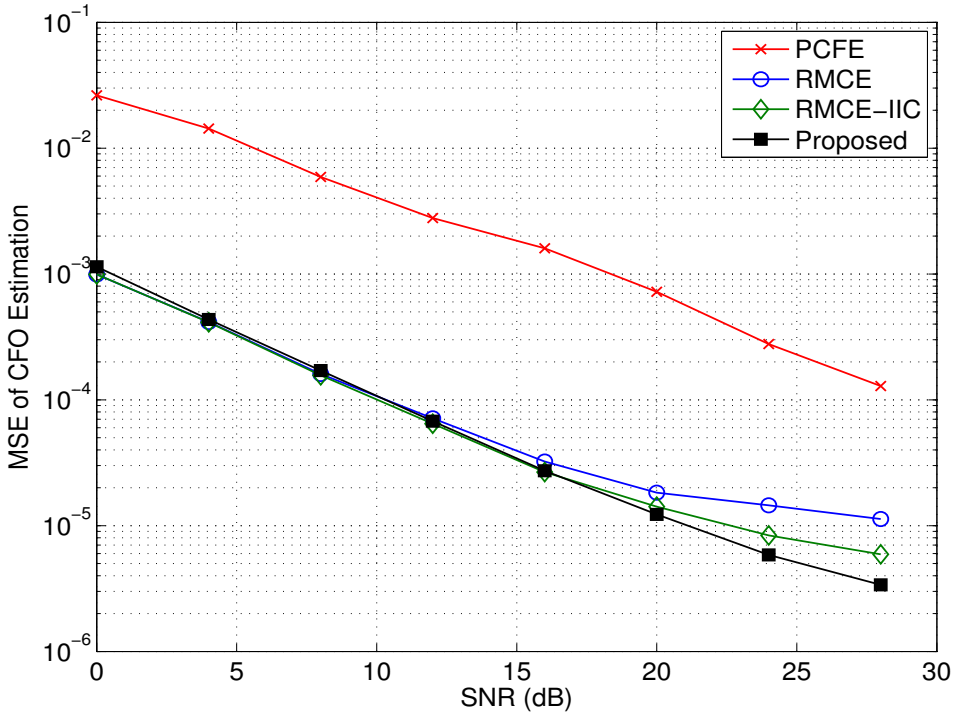

Figure 19: Performance of CFO estimation for $B = 2$.

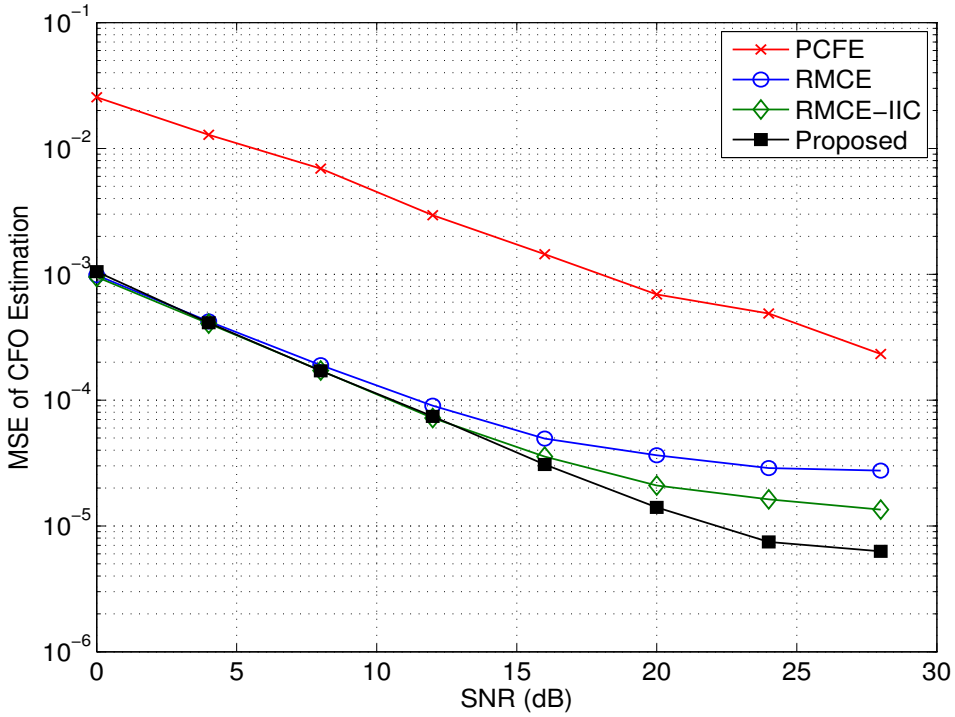

Figure 20: Performance of CFO estimation for $B = 3$.

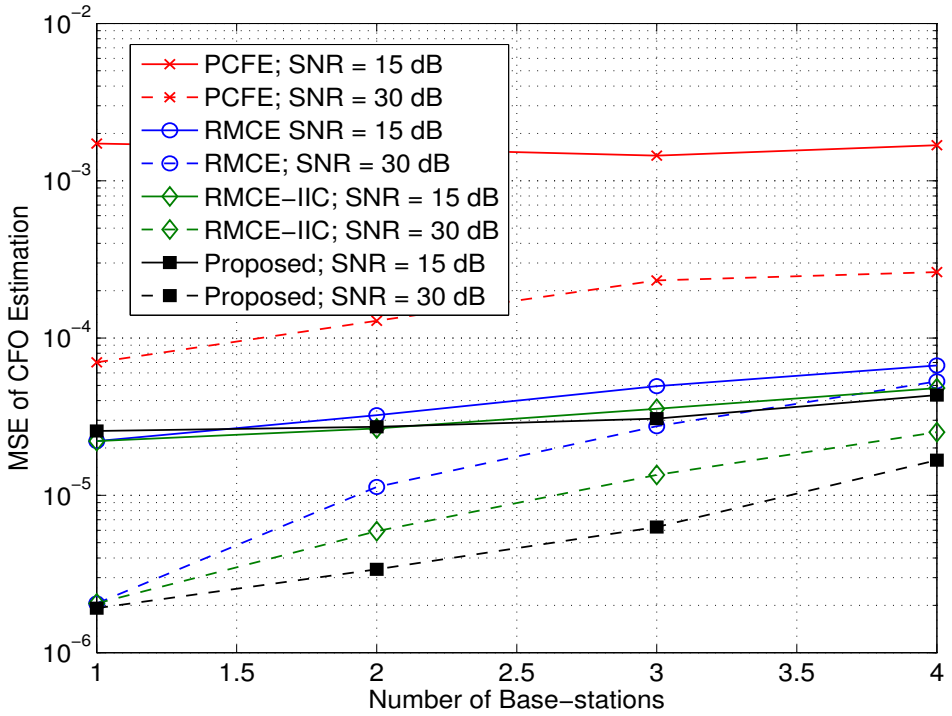

Figure 21: Performance of CFO estimation with increasing number of base-stations.

the proposed algorithm and [75] is kept same ($N_i = 100$). Recall that the algorithm in [75] without IIC is denoted as RMCE, while the performance with IIC ($N_{IC} = 1$ iteration) is denoted as RMCE-IIC. The algorithm in [39] (denoted as PCFE) uses $N_{IC} = 4$ iterations of interference cancelation. Figure 19 and 20 show the performance comparison for $B = 2$ and 3 respectively. As shown, the performance of the proposed algorithm is considerably improved as compared to PCFE [39]. Compared to [75] (RMCE and RMCE-IIC), the performance of the proposed algorithm is similar for lower SNRs and better for higher SNRs. The performance improvement compared to [75] increases as number of BSs increase to $B = 3$ in Figure 20. The performance of RMCE shows an error floor for higher values of SNR, and the error floor reduces when IIC is employed. The performance of RMCE-IIC can be further improved by performing more iterations. However, it further increases the latency and complexity of CFO estimation, which is already higher than the proposed algorithm, as discussed in Section 4.4.

Figure 21 shows the performance comparison as the number of BSs B increases from 1 to 4, for SNRs of 15 and 30 dB. As shown, performance of all algorithms degrades as number of BSs increase due to increased effect of IBI on CFO estimation. However, the proposed algorithms consistently performs better than PCFE, RMCE and RMCE-IIC, which shows the effectiveness of the proposed algorithm.

4.6 Hardware Implementation

This section presents the implementation details of the test-bed developed for CoMP transmissions and the real-time performance measurements taken in the lab to verify the performance of synchronization algorithms developed in this dissertation. We have implemented a 2 BS - 1 MU test CoMP case in which 2 BSs, each with one antenna, coordinate and transmit a space frequency block coded (SFBC) signal to the MU. Thus, the CoMP system acts like a cooperative but distributed transmit diversity system. The implementation has been carried out on the PXI[1]-based hardware platform provided by National Instruments (NI) corporation. The software tools used for programming the hardware components are LabVIEW® and LabVIEW – FPGA®. A brief introduction to the hardware and software features will be provided below. The physical layers parameters for OFDM transmissions used in the implementation are derived from LTE standard [40]. As the focus of this dissertation is synchronization of OFDM transmissions, we will mainly focus on the implementation and results of synchronization blocks in the CoMP transmissions setup. For details on the implementation of all OFDM transmissions blocks as shown in Figure 1, please refer to [23, 86].

[1]PXI stands for PCI eXtensions for Instrumentation, where PCI stands for Peripheral Component Interconnect.

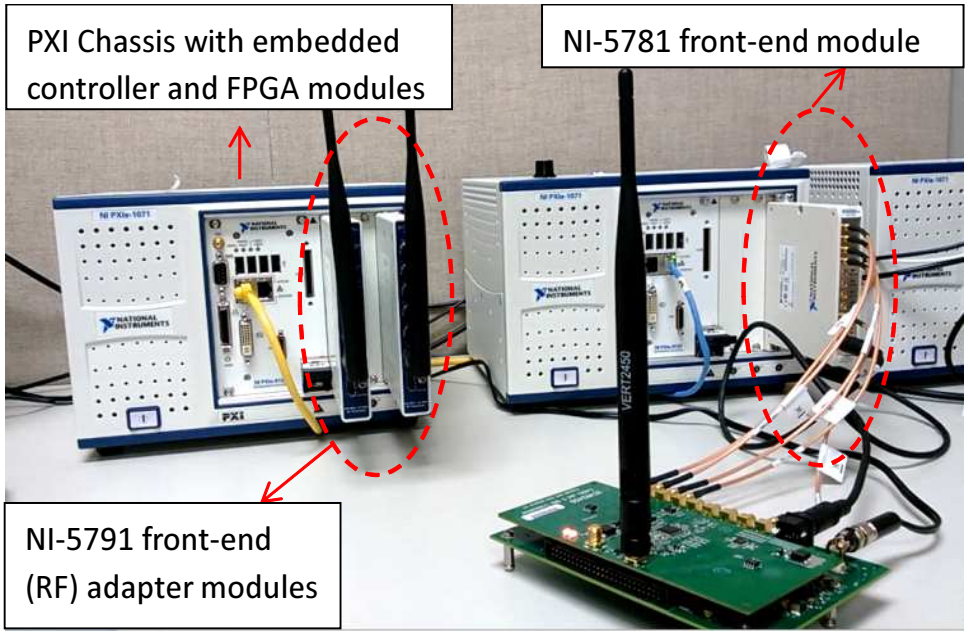

Figure 22: National Instruments' PXI platform used for hardware implementation.

4.6.1 Introduction to National Instruments' PXI Platform

Hardware tools NI's PXI platform is a modular instrumentation system, which consists of a PXI chassis hosting various modules depending on the system configuration. A snapshot of our lab system configuration is shown in Figure 22. As shown in the figure, each chassis contains a NI PXI-e 8133 embedded controller, which runs the LabVIEW real-time operating system. The left chassis in the figure also houses two transceiver chains with each containing a NI 7965R FPGA module paired with a NI 5791 RF transceiver module. The FPGA module contains a Xilinx® Virtex 5 FPGA while the RF transceiver module supports up to 100 MHz bandwidth (BW) with a 130 Mega samples per second (MS/s) sampling rate. The carrier frequency can be configured between 300 MHz to 4.4 GHz range. The right chassis in the figure has a different NI 5781 transceiver module, with 100 MS/s sampling rate and a dual-band $2.4 - 2.5$ GHz, $4.9 - 5.9$ GHz frequency range. Together, these chassis provide a flexible and very capable hardware platform, which can be used for prototyping of various communication systems.

LabVIEW® software is used to program the embedded controller as well as the FPGA module. LabVIEW is a graphical programming language, which uses different function nodes called virtual instruments (VI) connected through wires to create a data flow. The application programming interfaces (API) provided in LabVIEW enable the designer to control different parameters of the RF transceivers, e.g., sampling rate, transmit power, receive attenuation, carrier frequency etc. In addition, APIs for data and control signal hand-shaking between FPGA and embedded controllers are also available, which use the PXI chassis back-plane for communications between hardware modules. The FPGA is also programmed through LabVIEW-FPGA software package, and the resulting LabVIEW code is automatically synthesized into a bit-file to run on the FPGA. Thus, the designer can split the system implementation into different blocks running on either the controller or the FPGA depending on the throughput and the latency requirements of the specific block.

4.6.2 OFDM System Parameters

The physical layer parameters for OFDM used in the test-bed implementation have been derived from LTE DL standard specification [40]. The parameters are listed in Table 3. We also follow the frame structure of LTE DL transmissions, where each frame is divided into 20 slots each of 0.5 ms duration containing 6 OFDM symbols. Thus, each frame, containing 120 OFDM symbols, is of 10 ms duration.

Synchronization Signals LTE standard also specifies the synchronization signals, called primary and secondary synchronization signals for synchronization and cell identification [40]. We have implemented the primary synchronization signal (PSS), which is transmitted in the last OFDM symbol of slot 0 and slot 10 of each down-link frame. As the duration of a down-link frame is 10 ms (307200 samples at 30.72 MS/s) in LTE, PSS is transmitted after every 5 ms (153600 samples) time interval or once in a half-frame. PSS is transmitted on the middle 62 sub-carriers around the DC

Table 3: OFDM physical layer parameters used in the hardware implementation

Parameter	**Value**
Sub-carrier Spacing (Δf)	15 kHz
FFT Size (N)	2048
Cyclic Prefix length (N_g)	512
Sampling frequency (F_s)	30.72 MS/s
Bandwidth	20 MHz
Number of non-zero sub-carriers (R)	1200
Number of data sub-carriers	1000
Number of pilot sub-carriers	200
Supported modulation schemes	QPSK, 16 QAM, 64 QAM

sub-carrier of the OFDM symbol. These sub-carriers are modulated by a Zadoff-Chu sequence given by (23) with $M = 63$. We use two of the three root indices of ZC sequences defined in LTE, i.e, $u = 25, 29$ for the two BSs in the test-bed. DC sub-carrier as well as 5 sub-carriers on either side of the PSS are not modulated in order to facilitate extraction of the PSS through low-pass filtering. The rest of the sub-carriers of the corresponding OFDM symbol, also referred here as the PSS symbol, are data sub-carriers whose number depend on the operating BW. As the PSS is known at the receiver, it can be employed for signal detection and synchronization. For estimation of CFO between BSs in CoMP transmissions, we use the training symbol proposed in this Section 4.3. The proposed training symbol is transmitted in the OFDM symbol after the PSS. Once CFO between the BSs is estimated, the CFO estimate is fedback to the BSs and one of the BS adjusts in carrier frequency to synchronize with the other BS.

4.6.3 Real-time Performance Measurements and Results

We measure the performance of the implementation results in term of error vector magnitude (EVM) [68] of the equalized constellation symbols at the MU. The results are shown in Figure 23 for 16 QAM constellation, which shows the EVM of equalized sub-carriers for different values of CFO against the transmit power per BS. As shown,

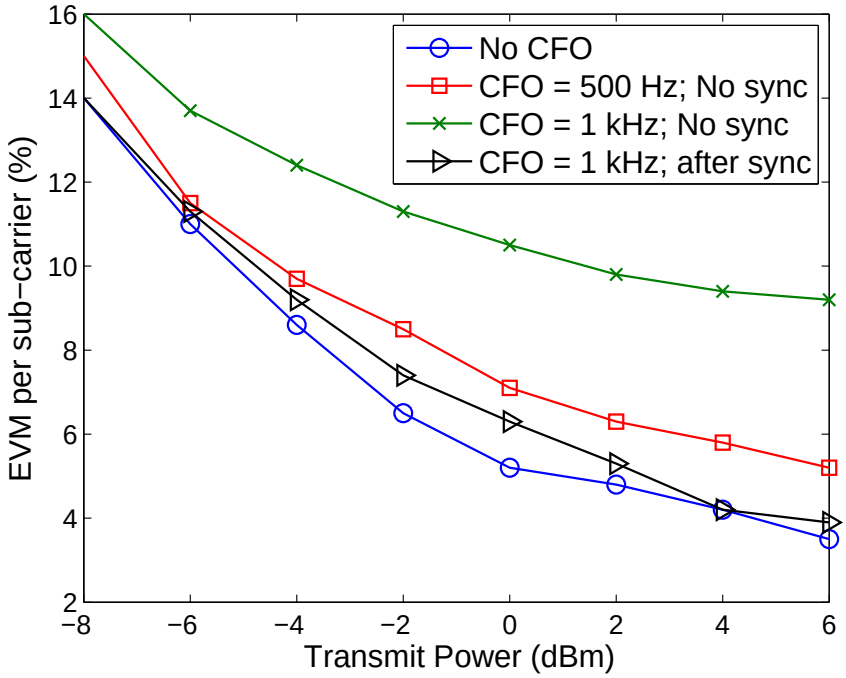

Figure 23: EVM per sub-carrier of the received signal with and without frequency synchronization.

the EVM of equalized sub-carriers decreases as the transmit power increases. Corresponding equalized constellations for transmit powers of 4 and -4 dBm are shown in Figures 24 and 25. For a particular transmit power, the EVM increases as the CFO between the two BSs increases. Without CFO estimation and compensation, non-zero CFO degrades the system performance as shown in Figures 24 and 25 for the cases of 500 Hz and 1 kHz and in Figure 23. However, after CFO estimation and compensation, the EVM of the equalized constellation is very close to the ideal case of no CFO. These real-time measurements results verify the effectiveness and feasibility of proposed CFO estimation algorithm.

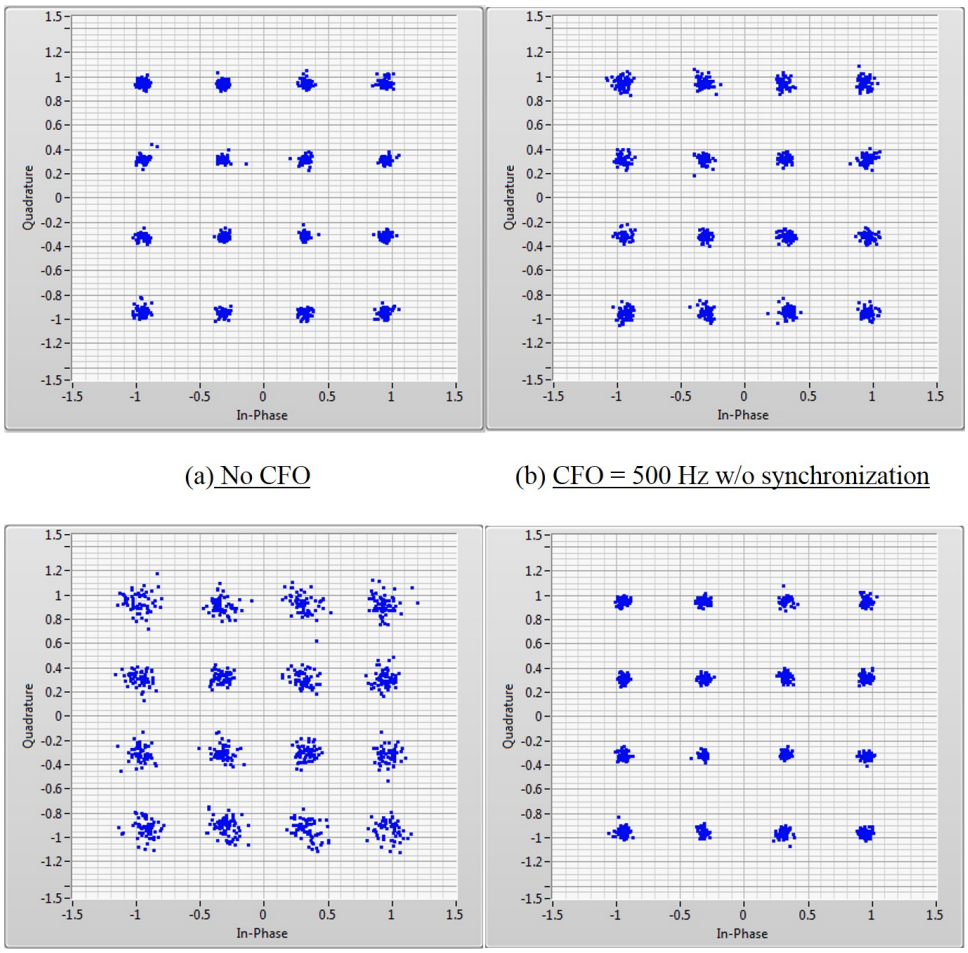

(a) No CFO

(b) CFO = 500 Hz w/o synchronization

(c) CFO = 1 kHz w/o synchronization

(d) CFO = 1 kHz after synchronization

Figure 24: Equalized constellation symbols with and without frequency synchronization with 4 dBm transmit power per BS.

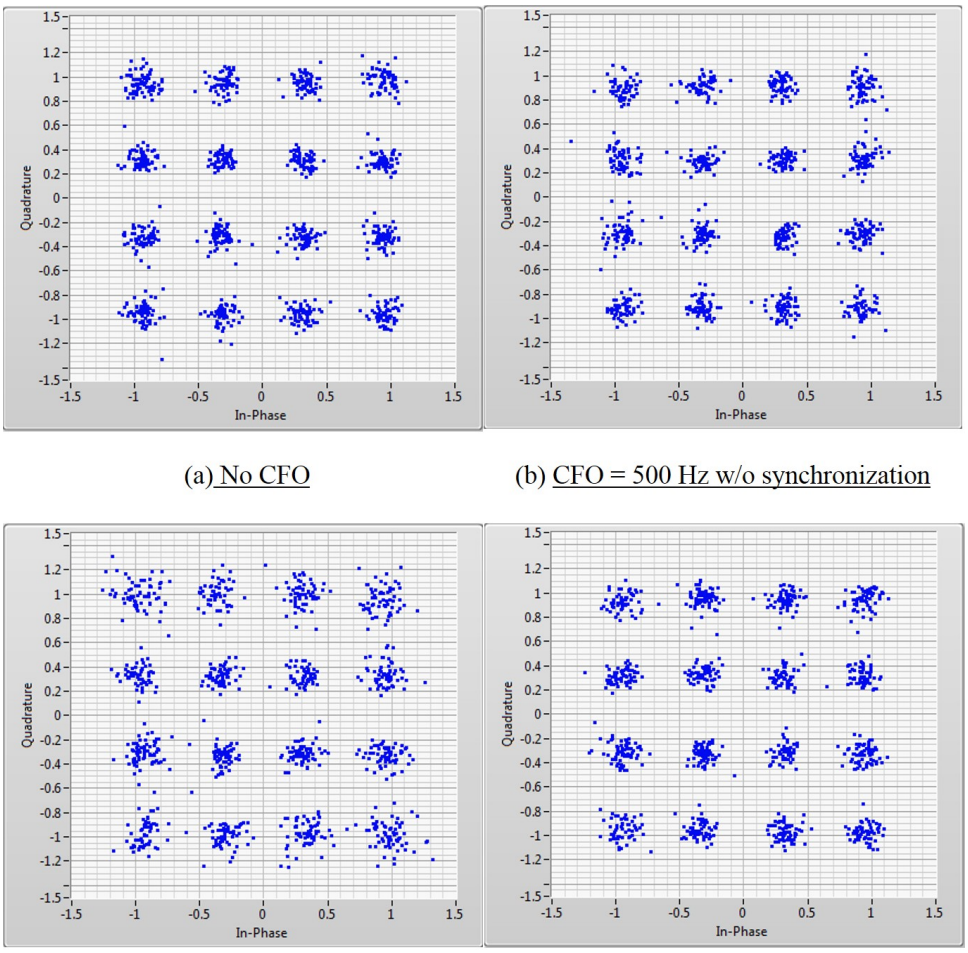

(a) No CFO

(b) CFO = 500 Hz w/o synchronization

(c) CFO = 1 kHz w/o synchronization

(d) CFO = 1 kHz after synchronization

Figure 25: Equalized constellation symbols with and without frequency synchronization with -4 dBm transmit power per BS.

CHAPTER V

FREQUENCY SYNCHRONIZATION FOR UPLINK OFDMA TRANSMISSIONS

In this chapter, we present a CFO estimation algorithm for OFDMA uplink transmissions employing SSAS or GSAS. The proposed algorithms employs null sub-carriers for CFO estimation. Specifically, a certain number of null sub-carriers are inserted in the first tile of the transmitted frame in the case of GSAS while in the case of SSAS, more than one OFDM symbols at the start of the frame contain null sub-carriers for CFO estimation. We design a cost function to estimate the CFOs by minimizing ICI and MUI on the null sub-carriers. The effects of the location of null sub-carriers on the MUI, CFO identifiability, and acquisition range are analyzed. We show that the acquisition range of the algorithm is dependent on the tile (sub-band) size and the placement of the null sub-carriers within the tile (sub-band). We further refine the CFO estimates obtained through null sub-carriers by using pilots sub-carriers for channel estimation. In the end, a comparison with existing approaches in the literature is performed in terms of computational complexity and performance.

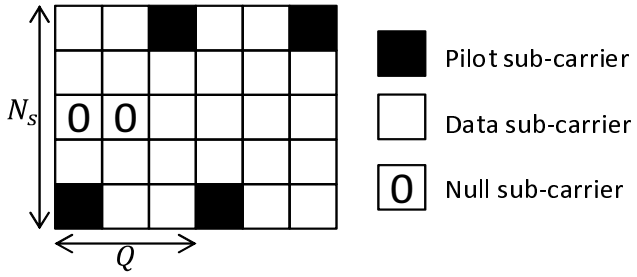

Figure 26: Generalized sub-carrier allocation scheme showing two consecutive tiles, each with $N_{\mathrm{s}} = 5$ sub-carriers and $Q = 3$ OFDM symbols.

5.1 Sub-carrier Allocation and Transmitted Signal Structure

Consider a base-band equivalent model of an OFDMA uplink system as discussed in Section 2.2.1 with N sub-carriers and M active users. The maximum number of users to accommodate is M_u. Resource allocation is carried out in terms of tiles as GSAS is employed. Later in this section, we show that the SSAS can be obtained as a special case of GSAS. The structure of a tile is shown in Figure 26, which shows two consecutive tiles, and each tile is a grid of $N_s \times Q$ sub-carriers, where N_s is the number of sub-carriers and Q is the number of OFDMA symbols. Therefore, there are $S = \left\lfloor \frac{N}{N_\mathrm{s}} \right\rfloor$ tiles available in the system for Q OFDMA symbols, indexed as $s = 0, \ldots, S-1$ and the sub-carriers in the s^{th} tile are $\mathcal{I}_s = \{sN_\mathrm{s}, sN_\mathrm{s}+1, \ldots, (s+1)N_\mathrm{s}-1\}$. The transmission takes place in frames where the total number of OFDMA symbols in a frame is a multiple of Q. Each user m is allocated an exclusive set of tiles denoted as $\mathcal{S}_m$ such that $\mathcal{S}_m \cap \mathcal{S}_{m'} = \phi$ when $m \neq m', m = 0, \ldots, M-1$. We assume that tile allocation for each user remains the same for the frame duration. Hence the sub-carriers allocated to the m^{th} user are defined by the set $\mathcal{I}_m := \bigcup_{s \in \mathcal{S}_m} \mathcal{I}_s$.

Pilot sub-carriers are inserted in each tile to facilitate channel estimation. We assume that the pilot pattern in each tile is the same and the indices of pilot sub-carriers in a tile are given as $\mathcal{I}_p(q) := \{n_0, \ldots, n_{N_p(q)-1} : n_p \in [0, N_s - 1]\}$ where $q = 0, \ldots, Q-1$. For example, the pilot pattern for tiles in Figure 26 is $\mathcal{I}_p(0) = \{0\}$, $\mathcal{I}_p(1) = \phi$ and $\mathcal{I}_p(2) = \{N_s - 1\}$.

Each user employs null sub-carriers in the tiles at the beginning of the frame to perform CFO estimation. Let the indices of null sub-carriers in each tile be denoted as $\mathcal{I}_n(q) := \{n_0, \ldots, n_{N_k-1} : n_k \in [0, N_s - 1]\}$, such that $\mathcal{I}_n(q) \cap \mathcal{I}_p(q) = \phi$. Let $\mathcal{I}_{mn}$, $\mathcal{I}_{mp}$ and $\mathcal{I}_{md}$, be the sets of indices of null sub-carriers (zero-value pilots), non-zero

pilots and data sub-carriers allocated to the m^{th} user, respectively. Then,

$$\mathcal{I}_{mn}(q) = \bigcup_{s \in \mathcal{S}_m} \{sN_s + n_k | n_k \in \mathcal{I}_n(q)\}. \tag{87}$$

Note that the null sub-carriers are inserted only in the beginning of the frame, i.e. only for first $K \leq Q$ symbols ($K = 2$ in Figure 26) while pilot sub-carriers are inserted in each tile through out the frame. A typical value of K is $2, 3$. Therefore, $|\mathcal{I}_{mn}(q)| = N_k|\mathcal{S}_m|$ for $q \leq K-1$ while $|\mathcal{I}_{mn}(q)| = 0$ for $q \geq K$. In the case of GSAS, we use $N_k = 1$. Similarly, $\mathcal{I}_{mp}(q) = \bigcup_{s \in \mathcal{S}_m} \{sN_s + n_p | n_p \in \mathcal{I}_p(q)\}$ with $|\mathcal{I}_{mp}(q)| = N_p(q)|\mathcal{S}_m|$ and $\mathcal{I}_{md}(q) = \mathcal{I}_m \setminus \{\mathcal{I}_{mp}(q) \cup \mathcal{I}_{mn}(q)\}$. We denote the total number of non-zero sub-carriers in the q^{th} OFDMA symbol for m^{th} user as $R(q) = |\mathcal{I}_m| - |\mathcal{I}_{mn}(q)|$. Note that the GSAS degenerates to SSAS when $S = M_u$ with $|\mathcal{S}_m| = 1$, i.e., each user is allocated only one tile (or sub-band in SSAS). However the value of N_s is much larger in SSAS as compared to GSAS.

Each user transmits its data points through its allocated sub-carriers. The q^{th} OFDMA symbol transmitted by the m^{th} user, before inverse discrete Fourier transform (IDFT), is given as

$$\mathbf{X}_m(q) = \mathbf{T}_m(q)\mathbf{S}_m(q), \tag{88}$$

where $\mathbf{S}_m(q)$ is an $R(q) \times 1$ vector which contains the information data and non-zero pilots for the q^{th} symbol of the m^{th} user and, $\mathbf{T}_m(q)$ is the $N \times R(q)$ sub-carrier allocation matrix for the m^{th} user:

$$\mathbf{T}_m(q) = [\mathbf{e}_{n_0}, \mathbf{e}_{n_1}, \ldots, \mathbf{e}_{n_{R(q)-1}}],$$

where $\mathbf{e}_n$ is the n^{th} column of $\mathbf{I}_N$ and n_i is the i^{th} element of $\mathcal{I}_{md}(q) \bigcup \mathcal{I}_{mp}(q)$. In Eq. (88), $\mathbf{S}_m(q)$ is defined as,

$$\mathbf{S}_m(q) = \mathbf{T}_{md}(q)\mathbf{D}_m(q) + \mathbf{T}_{mp}(q)\mathbf{P}_m(q), \tag{89}$$

where $\mathbf{P}_m(q)$ and $\mathbf{D}_m(q)$ are the $|\mathcal{I}_{mp}(q)| \times 1$ and $|\mathcal{I}_{md}(q)| \times 1$ vectors which contain the pilot and data symbols of the m^{th} user, respectively, and $\mathbf{T}_{mp}(q)$ and $\mathbf{T}_{md}(q)$ are

the corresponding $R(q) \times |\mathcal{I}_{mp}(q)|$ and $R(q) \times |\mathcal{I}_{md}(q)|$ mapping matrices, which map the data and pilot sub-carriers on their corresponding positions within the tiles. Note that $\mathbf{T}_{md}$ and $\mathbf{T}_{mp}$ are mutually orthogonal and defined in a similar way as $\mathbf{T}_m$.

We assume quasi-synchronous transmissions as discussed in Section 2.2.1 so that the TO of each MU can be incorporated in its effective channel $h_m[p],\ 0 \leq p \leq P-1$ given in (11). Under this assumption, the q^{th} received signal at the BS can be expressed as,

$$\mathbf{y}(q) = \sum_{m=0}^{M-1} \mathbf{y}_m(q) = \sum_{m=0}^{M-1} e^{j\frac{2\pi}{N} f_m (qN_{\mathrm{t}}+N_{\mathrm{g}})} \mathbf{D}_N(f_m) \mathbf{F}_N^H \mathbf{D}_N(\mathbf{H}_m) \mathbf{X}_m(q) + \mathbf{w}(q),$$

where f_m is the CFO of the m^{th} user and $\mathbf{H}_m$ is the $N \times 1$ vector containing the N-point DFT of the m^{th} MU's effective CIR. $\mathbf{w}(q)$ is the $N \times 1$ vector containing the AWGN samples for the q^{th} symbol. Note that $|f_m| \leq f_{\max}$, where $f_{\max}$ is the maximum CFO. Taking DFT of the received signal at the BS results in

$$\mathbf{Y}(q) = \mathbf{F}_N \mathbf{y}(q) = \sum_{m=0}^{M-1} e^{j\frac{2\pi}{N} f_m (qN_{\mathrm{t}}+N_{\mathrm{g}})} \mathbf{F}_N \mathbf{D}_N(f_m) \mathbf{F}_N^H \mathbf{T}_m \mathbf{D}_R(\bar{\mathbf{H}}_m(q)) \mathbf{S}_m(q) + \mathbf{F}\mathbf{w}(q),$$

where $\bar{\mathbf{H}}_m(q) = \mathbf{T}_m(q)^T \mathbf{H}_m$ is an $R(q) \times 1$ vector containing the channel frequency response at the non-zero sub-carriers of the m^{th} user.

5.2 CFO Estimation Algorithm

In this section, we formulate the null sub-carrier-based method to estimate the CFO of each user separately. The proposed algorithm only makes use of those OFDMA symbols, which contain null sub-carrier (first K symbols). Also the number and location of null sub-carriers within those symbols remains constant. Therefore, we omit the index 'q' from the expressions of $R(q)$, $\mathcal{I}_{mn}(q)$and $\mathbf{T}_m(q)$ for notational simplicity. Also, we use m' to indicate the user for which the CFO estimation is being carried out, and m to indicate the other users.

The autocorrelation matrix of the received symbol, assuming the transmitted symbols are uncorrelated with zero mean and the channel response remains constant for

K symbols, is given as

$$\mathbf{R_{yy}} = E\{\mathbf{y}\mathbf{y}^H\} = \sum_{m=0}^{M-1} \mathbf{D}_N(f_m)\mathbf{F}_N^H\mathbf{T}_m\mathbf{D}_R(\bar{\mathbf{H}}_m)\mathbf{R}_{\mathbf{S}_m\mathbf{S}_m}\mathbf{D}_R^H(\bar{\mathbf{H}}_m)\mathbf{T}_m^H\mathbf{F}_N\mathbf{D}_N^H(f_m) + \sigma_w^2\mathbf{I}_N, \tag{90}$$

where $\mathbf{R}_{\mathbf{S}_m\mathbf{S}_m}$ and $\sigma_w^2\mathbf{I}_N$ are the autocorrelation matrices of $\mathbf{S}_m(q)$ and $\mathbf{w}(q)$, respectively. Note that in the absence of noise, the Fourier transform vector corresponding to each null sub-carrier of the m'^{th} user is orthogonal to the autocorrelation matrix when $f_m = 0$ for each m, i.e., $\mathbf{f}_N^H(i)\mathbf{R_{yy}} = \mathbf{0}_{1\times N}$ for each $i \in \mathcal{I}_{mn}$ when $f_m = 0$. In other words, in a synchronized system, the energy (or interference) falling onto null sub-carriers of each user should be zero. Thus, a cost function for the m'^{th} user employing its null sub-carriers can be formed as,

$$J_{m'}(f_o) = \sum_{i\in\mathcal{I}_{m'n}} \mathbf{f}_N^H(i)\,\mathbf{D}_N^H(f_o)\mathbf{R_{yy}}\mathbf{D}_N(f_o)\mathbf{f}_N(i)\,, \tag{91}$$

which is a measure of interference on null sub-carriers of the m'^{th} user for a candidate CFO estimate $|f_o| \le f_{\max}$. The cost function in (91) is used for each user employing its own null sub-carriers only, and the value of f_o that minimizes the cost function is taken as the estimate of the CFO for the m'^{th} user:

$$\hat{f}_{m'} = \arg\min_{f_o}\left(J_{m'}(f_o)\right).$$

Using (90), the cost function in (91) can be rewritten as a sum of an ICI term, also referred here as the 'self interference' (SI) term, and the MUI term as follows:

$$J_{m'}(f_o) = J_{m',\mathrm{SI}}(f_o) + J_{m',\mathrm{MUI}}(f_o), \tag{92}$$

where

$$J_{m',\mathrm{SI}}(f_o) = \sum_{i\in\mathcal{I}_{m'n}} \mathbf{f}_N^H(i - f_{m'} + f_o)\,\mathbf{F}_N^H\mathbf{T}_{m'}\mathbf{D}_R(\bar{\mathbf{H}}_{m'})\mathbf{R}_{\mathbf{S}_{m'}\mathbf{S}_{m'}}\mathbf{D}_R^H(\bar{\mathbf{H}}_{m'})\mathbf{T}_{m'}^H \times \mathbf{F}_N\mathbf{f}_N(i - f_{m'} + f_o) + \sigma_w^2,$$

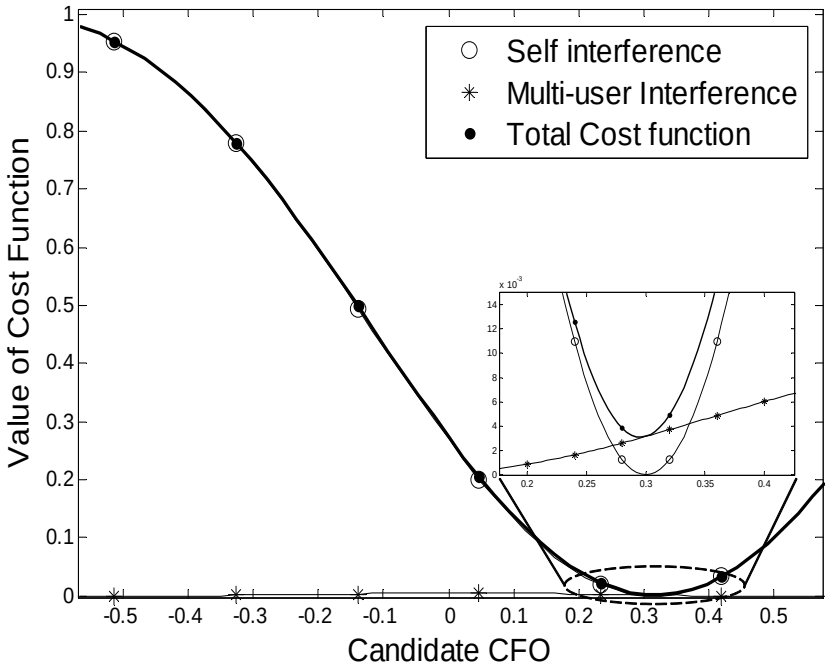

Figure 27: A typical plot showing the SI, MUI, and the total cost function for CFO estimation ($f_{m'} = 0.3$).

since $\mathbf{f}_N^H(a_1)\,\mathbf{D}_N(a_2) = \mathbf{f}_N^H(a_1 - a_2)$ for any real a_1 and a_2 and,

$$J_{m',\mathrm{MUI}}(f_o) = \sum_{m=0, m\neq m'}^{M-1} \tilde{J}_{m',m}(f_o),$$

with

$$\tilde{J}_{m',m}(f_o) = \sum_{i\in\mathcal{I}_{m'n}} \mathbf{f}_N^H(i - f_m + f_o)\,\mathbf{F}_N^H\mathbf{T}_m\mathbf{D}_R(\bar{\mathbf{H}}_m)\mathbf{R}_{\mathbf{S}_m\mathbf{S}_m}\mathbf{D}_R^H(\bar{\mathbf{H}}_m)\mathbf{T}_m^H \times \mathbf{F}_N\mathbf{f}_N(i - f_m + f_o) + \sigma_w^2.$$

As the noise term σ_w^2 is independent of the CFO, it can be dropped from the cost function. Note that when the candidate CFO value is equal to the true CFO value of the desired user m', i.e., $f_o = f_{m'}$ in (92), the SI term will be zero whereas the MUI term can still be non-zero because the other users can have different CFOs. This non-zero MUI term can change the minimum of the cost function. If we can minimize the MUI for null sub-carriers, the effect of this MUI on CFO estimation will

be minimized. Hence, the main idea behind our CFO estimation method is that we search for the CFO value, which minimizes the SI and simultaneously mitigate the MUI by optimizing the location of null sub-carriers within the tile, so that the total cost function still reaches the global minimum when $f_o = f_{m'}$. Figure 27 shows a typical plot for the SI and MUI terms along with the total cost function. We observe that SI dominates the cost function, but MUI may affect the global minimum as well.

In practice, $\mathbf{R_{yy}}$ is replaced by its sample estimate

$$\hat{\mathbf{R}}_{\mathbf{yy}} = \frac{1}{K} \sum_{q=1}^{K} \mathbf{y}(q)\mathbf{y}^H(q), \tag{93}$$

using the received OFDMA symbols containing null sub-carriers.

5.3 Identifiability and Acquisition Range Analysis

Identifiability means uniqueness of the CFO estimates, which ultimately defines the acquisition range of the algorithm. The cost function in (91) is affected by channel nulls as well as MUI. Hence, an identifiability analysis of the proposed CFO estimation algorithm is a critical task and a major part of our research on UL OFDMA transmissions. The identifiability analysis of null sub-carrier-based CFO estimation for DL OFDM transmissions has been carried out in [43]. However, the identifiability analysis of the null sub-carrier-based CFO estimation for OFDMA has not been presented before. In this section, we analyze the effects of MUI, null sub-carrier position and channel nulls on the cost function in (91). We show that null sub-carrier positions play an important role in determining the acquisition range of the algorithm and prove the identifiability of CFO estimation.

5.3.1 Effect of SI on Identifiability and Acquisition Range

At first, consider the effect of the SI term only and ignore the effects of MUI and channel nulls by assuming that $\mathbf{D}_R(\bar{\mathbf{H}}_{m'})$ is full rank . Then, the SI term in (92) is

zero if and only if,

$$\mathbf{f}_N^H \left(i - f_{m'} + f_o\right) \mathbf{F}_N^H \mathbf{T}_{m'} = \mathbf{0}^T, \forall i \in \mathcal{I}_{m'n},$$

or equivalently by using (87),

$$\mathbf{f}_N^H \left(s'N_s + n_k - f_{m'} + f_o\right) \mathbf{F}_N^H \mathbf{T}_{m'} = \mathbf{0}^T, \forall (s'N_s + n_k) \in \mathcal{I}_{m'n}, \tag{94}$$

which means that $\mathbf{f}_N^H \left(s'N_s + n_k - f_{m'} + f_o\right)$ should lie in the left null space (LNS) of $\mathbf{F}_N^H \mathbf{T}_{m'}$. As $\mathbf{F}_N^H \mathbf{T}_{m'}$ only contains the Fourier transform vectors corresponding to the non-zero sub-carriers of the m'^{th} user, its LNS contains the Fourier transform vectors corresponding to two sub-carrier groups: the null sub-carriers of the m'^{th} user ($\mathcal{I}_{m'n}$) as well as all the sub-carriers of other users ($\{\bigcup_{m \neq m'} \mathcal{I}_m\} \setminus \mathcal{I}_{m'}$). Therefore, (94) is satisfied for $f_o = f_{m'}$ as $(s'N_s + n_k - f_{m'} + f_o) \in \mathcal{I}_{m'n}$, for each $s' \in \mathcal{S}_{m'}$ and for each $n_k \in \mathcal{I}_n$. However, as f_o is varied, (94) may again be satisfied if $(s'N_s + n_k - f_{m'} + f_o) \in (\bigcup \mathcal{I}_m \setminus \mathcal{I}_{m'})$, for some $s' \in \mathcal{S}_{m'}$ and $n_k \in \mathcal{I}_n$. which can result in multiple minima of the cost function. Therefore, CFO is uniquely identifiable as the true $f_{m'}$ if $(s'N_s + n_k - f_{m'} + f_o)$ is restricted to the sub-carrier indices of its corresponding tile only, i.e. if,

$$s'N_s - 1 < s'N_s + n_k - f_{m'} + f_o < (s' + 1)N_s,$$

or if,

$$n_k - N_s < f_{m'} - f_o < n_k + 1, \tag{95}$$

for each $s' \in \mathcal{S}_{m'}$. Since $|f_{m'}| \leq f_{\max}$ as mentioned before, $|f_{m'} - f_o| \leq 2f_{\max}$. Therefore, considering the SI only, the maximum uniquely identifiable CFO is given as,

$$f_{\max} = \frac{1}{2} \min_k \left(|n_k + 1|, |n_k - N_s|\right). \tag{96}$$

As (96) does not depend on the number of tiles allocated to the m'^{th} user, it applies equally for GSAS and SSAS, bearing in mind that N_s represents the sub-band size for SSAS as mentioned earlier.

5.3.2 Effect of MUI on Identifiability and Acquisition Range

Now we consider the effect of MUI on the acquisition range and the identifiability. We deal with the identifiability issues caused by the channel in the next sub-section and thus, assume here that the channel matrix $\mathbf{D}_R(\bar{\mathbf{H}}_m)$ has full rank. For simplicity, we will consider that each user is assigned only one tile and the system is fully loaded, i.e. $M = M_u = S$. This assumption models a worst case scenario as assigning multiple tiles for the user in consideration can only decrease the MUI. Moreover, multiple tiles for an interfering user can be considered as different users with one tile per user but with same CFO. Hence, it is sufficient to prove the identifiability of an arbitrary user with only one tile assigned to it. As each user in SSAS contains one tile or sub-band by definition, the analysis is directly applicable to SSAS as well. If the number of tiles is equal to number of users we can assume, without loss of generality, that the m^{th} user is assigned to the m^{th} tile so that $\mathcal{S}_m = \{m\}$ for all $m = 0, \ldots, M-1$.

Under these assumptions and after some algebraic manipulations, the SI and MUI terms in (92) can be rewritten as,

$$J_{m',\mathrm{SI}}(f_o) = \frac{1}{N^2} \sum_{k=0}^{N_\mathrm{k}-1} \sum_{r=0, r\neq n_k}^{N_s-1} \sigma^2_{\mathbf{x}_{m'}} |[\mathbf{H}_{m'}]_{m'N_s+r}|^2 \psi^2_{\Delta m', \Delta r}(f_{m'} - f_o), \tag{97}$$

and

$$\tilde{J}_{m',m}(f_o) = \frac{1}{N^2} \sum_{k=0}^{N_\mathrm{k}-1} \sum_{r=0, r\neq n_k}^{N_s-1} \sigma^2_{\mathbf{x}_{m}} |[\mathbf{H}_{m}]_{mN_s+r}|^2 \psi^2_{\Delta m, \Delta r}(f_{m} - f_o), \tag{98}$$

where we assumed that the data symbols transmitted by each user are uncorrelated from each other and from different users and thus, $\mathbf{R}_{\mathbf{S}_m\mathbf{S}_m} = \sigma^2_{S_m}\mathbf{I}$. $\psi_{\Delta m, \Delta r}(x) = \frac{\sin(\pi x)}{\sin\left(\frac{\pi}{N}(x + N_s\Delta m + \Delta r)\right)}$ with $\Delta m = m - m'$ and $\Delta r = r - n_k$ represents the normalized interference caused by the r^{th} sub-carrier of the m^{th} user on the null sub-carrier (n_k) of the m'^{th} user due to the difference 'x' between the candidate CFO and the m^{th} user's CFO.

$\psi^2_{\Delta m, \Delta r}(f_m - f_o)$ is a sinc-over-sinc squared function with period N. Its magnitude is maximum (equal to N^2) at the center of its main lobe, i.e., when $f_m - f_o + N_s\Delta m +$

Δr in the denominator is an integer multiple of N, and it is zero when $f_m - f_o + N_s\Delta m + \Delta r$ is an integer other than a multiple of N . Therefore, as the candidate CFO f_o is varied, the value of MUI also varies. As $|\Delta r| \leqslant N_s - 1$, the normalized MUI terms in (98) are dominant for $\Delta m = \pm 1$, which correspond to the adjacent users $(m' \pm 1)$. Eq. (98) also suggests that given f_m and f_o, the interference caused by the $(m'+1)^{st}$ user on the null sub-carrier n_k of the m'^{th} user is greater than the $(m'-1)^{st}$ user if the null sub-carrier is closer to the $(m'+1)^{st}$ user and vice versa. Consequently, total MUI is minimized if the null sub-carrier for each user is placed at the center of its sub-band.

As the MUI term, in (92), is non-zero and varies with f_o, it can affect the uniqueness of the cost function which is a sum of both SI and MUI. We show that this effect depends on whether the MUI has a sample from the main lobe of $\psi^2_{\Delta m,\Delta r}(f_m - f_o)$ or not. We discuss these two cases separately below.

Case 1 (Refined acquisition range) When $f_m - f_o > 2f_{max} - 1$ for $\Delta m = -1$ or $f_m - f_o < -2f_{max} + 1$ for $\Delta m = 1$ where $f_{\max}$ is given by (96), (98) suggests that the MUI for one of the adjacent users will attain its maximum value as $J_{m',\mathrm{MUI}}(f_o)$ will have a sample from the main lobe of $\psi^2_{\Delta m,\Delta r}(f_m - f_o)$, depending on the null sub-carrier index n_k. If f_o is close to $f_{m'}$ at the same time, the maximum of MUI and the minimum of SI occur simultaneously and the minimum of the cost function can change or become non-unique. This extreme case of MUI occurs when $f_{m'}$ is close to $\pm f_{\max}$ and $f_{m'\pm 1}$ is close to $-f_{m'}$ according to (96). Figure 28 shows an example of such a case for $N_s = 2$. As shown, the minimum of SI at $f_{m'} = 0.3$ gets vanished due to MUI from a user with $f_{m'+1} = -0.4$ and the total cost function reaches a minimum at a wrong CFO value. Hence the uniqueness of the CFO estimate cannot be guaranteed in this case and the maximum identifiable CFO range will be reduced

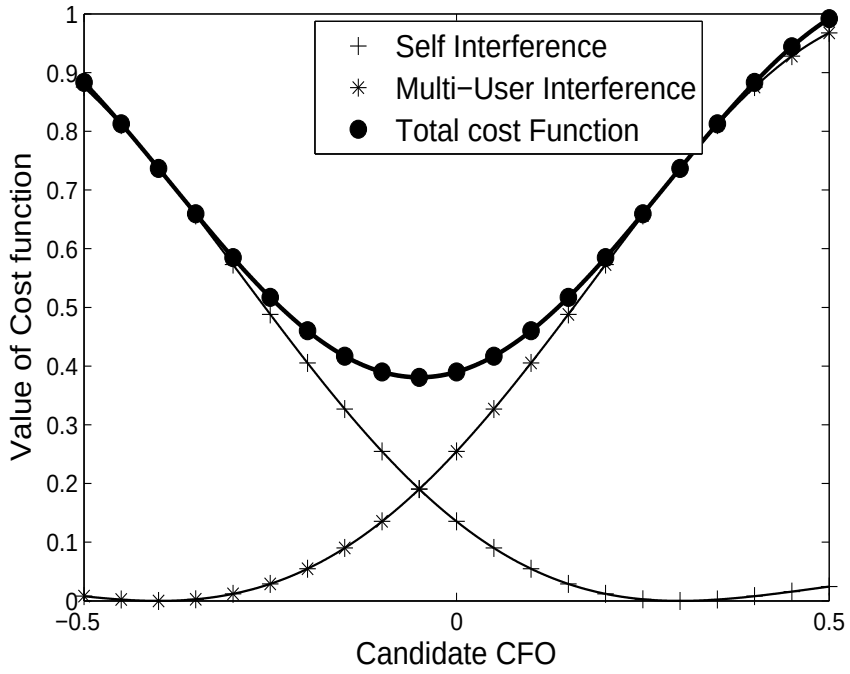

Figure 28: Ambiguity in CFO estimation when $f_{m'} = 0.3$, $f_m = -0.4$, $N_s = 2$, $N_{\mathrm{k}} = 1$, and $n_k = 1$.

to,

$$f_{\max} = \frac{1}{2}\left(\min_k \left(|n_k + 1|, |n_k - N_s|\right)\right) - c. \tag{99}$$

In this refined acquisition range, $0 \leq c \leqslant \frac{1}{2}$ is a constant whose value depends on the specific values of CFO of all the users, and it is chosen such that the MUI term for each interfering user can have samples from the first side lobe of $\psi^2_{\Delta m,\Delta r}(x)$ at most. As the values of CFO are not known beforehand, we choose $c = \frac{1}{2}$ as a sufficient condition in (99) as it ensures that MUI will never contain samples from the main lobe of $\psi^2_{\Delta m,\Delta r}(x)$, irrespective of the CFO values of all the users.

Case 2 (Identifiability for refined acquisition range) The refined acquisition range in (99) always avoids Case 1 but one may argue that as MUI is non-negative, it can still result in multiple minima of the cost function. Figure 29 shows a hypothetical scenario in which MUI adds to the SI and the total cost function has two minima. As

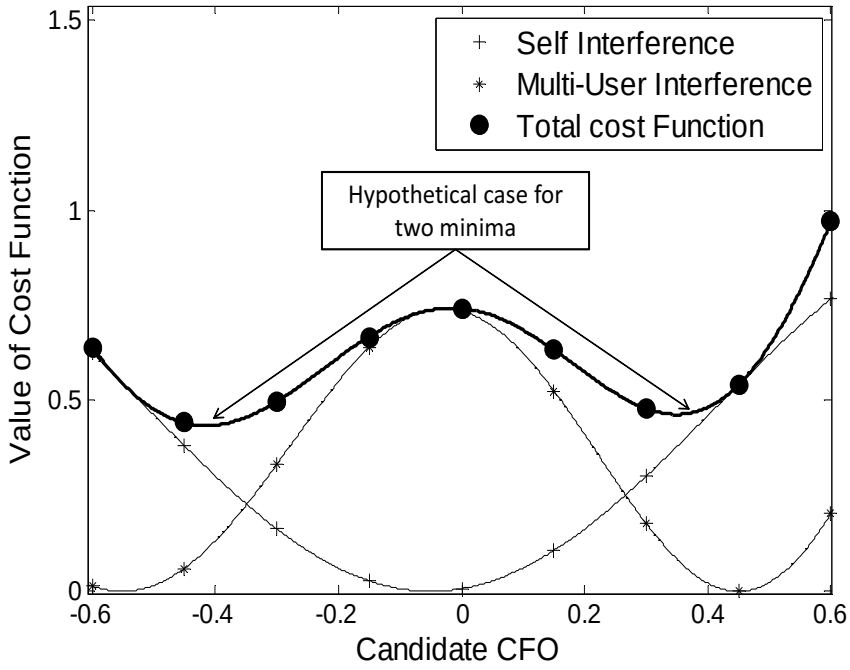

Figure 29: A hypothetical worst case MUI scenario causing ambiguity in CFO estimation for $f_{m'} = -0.05$.

shown, the MUI term does not have a very large magnitude as in Case 1 but, it has a more sharp peak as compared to the SI term and raises the minimum of SI term at $f_o = -0.05$ to cause two minima in the cost function. However, we now prove the non-existence of this case under the refined acquisition range of (99). The idea behind the proof is to use the concept of curvature. As the curvature signifies the measure of the peak of a curve [36], the case shown in Figure 29 can never occur if the curvature of the SI term at its minimum is greater than the curvature of the MUI term.

Proposition 4: If the maximum allowable CFO range is given by (99), the curvature of the normalized MUI term is always less than the curvature of the SI term at its minimum, given $N_s \geq 3$, and thus, the identifiability of the CFO estimation for the acquisition range in (99) is always guaranteed.

Proof: Assume that all the users have equal power. We will analyze the effect of

un-equal power through simulation results in Sec 5.6. Note that the curvature of the MUI term at positions other than the minimum of the SI term does not cause any identifiability problem. Therefore, we model a worst case MUI scenario in which the MUI has the maximum curvature at the minimum of the SI. We then prove that the curvature of this worst case MUI is less than the curvature of the SI at its minimum, and thus, the CFO estimate is unique. Based on (98), let us define normalized MUI $\mathcal{J}_{m',\mathrm{MUI}}(f_o)$ with M_u active users as,

$$\mathcal{J}_{m',\mathrm{MUI}}(f_o) = \sum_{m=0,m\neq m'}^{M_u-1} \tilde{\mathcal{J}}_{m',m}(f_o),$$

where

$$\tilde{\mathcal{J}}_{m',m}(f_o) = \frac{1}{N^2} \sum_{r=0,r\neq n_k}^{N_s-1} \psi^2_{\Delta m,\Delta r}(f_m - f_o). \tag{100}$$

The curvature of the normalized MUI at any point is given as [36],

$$\kappa_{\mathcal{J}_{m',\mathrm{MUI}}}(f_o) = \frac{\left|\frac{\partial^2 \mathcal{J}_{m',\mathrm{MUI}}(f_o)}{\partial f_o^2}\right|}{\left(1 + \left(\frac{\partial \mathcal{J}_{m',\mathrm{MUI}}(f_o)}{\partial f_o}\right)^2\right)^{\frac{3}{2}}}.$$

Similarly the curvature $\kappa_{\mathcal{J}_{m',\mathrm{SI}}}(f_o)$ of the SI term can be derived by defining normalized SI $\mathcal{J}_{m',\mathrm{SI}}(f_o) = \tilde{\mathcal{J}}_{m',m'}(f_o)$. The curvature of $\tilde{\mathcal{J}}_{m',m}(f_o)$ for each m in (100) is maximum when an extreme point of a side lobe of $\psi^2_{\Delta m,\Delta r}(f_m - f_o)$ is sampled. This happens whenever $f_m - f_o = i$ or $f_m - f_o = i \pm \frac{1}{2}$ in (100), for a particular value of Δm and Δr, where i is an integer. We are interested in the case when $f_m - f_0 = i \pm \frac{1}{2}$ because in that case, the maximum of the side lobe is sampled. At a maximum point of $\psi^2_{\Delta m,\Delta r}(f_m - f_o)$, larger magnitude of the second derivative implies larger curvature. As the width of each side lobe is constant, a side lobe with larger maximum magnitude will have larger curvature. As a side lobe closer to the main lobe has a larger maximum magnitude, the curvature of $\tilde{\mathcal{J}}_{m',m}(f_o)$ for each m will be maximum for $f_m - f_0 = \pm(2f_{\max} - \frac{1}{2})$ as this value, for a given Δm and Δr, provides a sample from a side lobe closest to the main lobe. Therefore, if all interfering users have

the same f_m namely $\bar{f}$, all the $\tilde{\mathcal{J}}_{m',m}(f_o)$ terms will be coherent and, a candidate CFO value f_o will satisfy $f_m - f_0 = \pm 2f_{\max} - \frac{1}{2}, \forall m \neq m'$ simultaneously, for which curvature of $\tilde{\mathcal{J}}_{m',m}(f_o)$ for each $m \neq m'$ will be maximum and add up to give an MUI with maximum curvature. Therefore,

$$\max\left(\kappa_{\mathcal{J}_{m',\mathrm{MUI}}}(f_o)\right) = \kappa_{\mathcal{J}_{m',\mathrm{MUI}}}(f_o)|_{(f_m=\bar{f},\forall m\neq m')},$$

for f_o satisfying $f_m - f_o = \pm(2f_{\max} - \frac{1}{2})$.

In order to disturb the uniqueness of the CFO estimate, this maximum curvature of the MUI should occur at the minimum of the SI term. This condition is satisfied in two cases: First, when $f_m = f_{\max}$ for all the interfering users and $f_{m'} = -f_{\max} + \frac{1}{2}$ for $n_k < \frac{N_s}{2}$, and second, when $f_m = -f_{\max}$ for all the interfering users and $f_{m'} = f_{\max} - \frac{1}{2}$ for $n_k \geq \frac{N_s}{2}$. In both cases, the minimum of the SI term occurs at $f_o = f_{m'}$ and at the same point $f_m - f_o = \pm(2f_{\max} - \frac{1}{2})$ is also satisfied and therefore, the worst case of the MUI term has the maximum curvature at the minimum of the SI term. We prove the identifiability for this worst case by showing in the appendix D that $\kappa_{\mathcal{J}_{m',\mathrm{SI}}}(f_o = f_{m'}) > \max\left(\kappa_{\mathcal{J}_{m',\mathrm{MUI}}}(f_o)\right)$ for $N_s \geq 3$.■

Thus, the acquisition range of CFO estimation is given by (99). As the value of $f_{\max}$ in (99) changes as the null sub-carrier position n_k changes, the acquisition range is dependent on the null sub-carrier position. Eq. (99) shows that non-zero acquisition range can be obtained if each null sub-carrier, placed with in a tile, has at least one data sub-carrier on its either side, i.e. $(N_s - 1) < n_k < 1$ for all $n_k \in \mathcal{I}_n$. Maximum acquisition range is achieved for $N_k = 1$ with $n_k = \lfloor \frac{N_s}{2} \rfloor$, i.e., when the null sub-carrier is at the middle of a tile. This shows that the null sub-carrier in the middle of the sub-band not only results in lower MUI as discussed in the previous section but also results in a larger acquisition range. As the CFOs on the uplink are usually fractional, i.e., $f_{\max} \leq 0.5$, (99) also shows that the proposed null sub-carrier CFO estimation can work for any tile size with $N_s \geq 3$ and with null sub-carriers placed anywhere except the edges. Moreover, considering the effect of MUI only, the optimal

position for a null sub-carrier is the middle of the tile. However, this null placement strategy may not be optimal in the presence of frequency selective channel, as the next section will show. Note that if users have different tile sizes N_s, their CFO acquisition ranges can be different. Eq. (99) also shows that if $N_s \geq 5$, the proposed algorithm is capable of estimating integer CFOs as well. For example, with $N_s = 5$, $N_k = 1$, and $n_k = 2$, the acquisition range based on (99) will be ± 1. Although the need for integer CFO estimation does not arise in uplink communications, it may be needed in multi-point to multi-point communications, e.g., wireless mesh networks [32, 38].

5.3.3 Effect of Channel Frequency Selectivity on Identifiability

In the previous sections, we ignored the effect of channel frequency selectivity by assuming that the channel matrix $\mathbf{D}_R(\bar{\mathbf{H}}_{m'})$ has full rank, i.e., there is no channel null corresponding to the non-zero sub-carriers of the m'^{th} user. We now consider the effect of these channel nulls on the identifiability because if the channel has nulls at one or more of the non-zero sub-carriers of a user, it may cause an identifiability issue [43]. In (92), the SI term is zero if,

$$\sum_{s' \in \mathcal{S}_{m'}} \sum_{k=1}^{N_{\mathrm{k}}} \mathbf{f}_N^H \left(s' N_s + n_k - f'_m + f_o \right) \mathbf{F}_N^H \mathbf{T}_{m'} \mathbf{D}_R(\bar{\mathbf{H}}_{m'}) = \mathbf{0}^T. \tag{101}$$

Now, let us suppose that the channel for the m'^{th} user has N_{i} nulls at $\{\gamma_{m',i}\}_{i=1}^{N_{\mathrm{i}}}$ sub-carriers where each $\gamma_{m',i} \subset \mathcal{I}_{m'}$. As CIR for the m'^{th} user is of order $P_{m'}$, $N_i \leq P_{m'}$. Then the condition in (101) is satisfied if

$$\{s' N_s + n_k - f_{m'} + f_o\} \subset \{\gamma_{m',i}\}_{i=1}^{N_{\mathrm{i}}} \bigcup \mathcal{I}_{m'n}, \forall s' \in \mathcal{S}_{m'}, n_k \in \mathcal{I}_n. \tag{102}$$

This condition is clearly satisfied for $f_o = f_{m'}$. But it can also be satisfied for other values of f_o as well. As the CFO on the uplink is only fractional, i.e. $f_{\max} \leq 0.5$ as mentioned above, $|f_o - f_{m'}| \leq 2f_{\max} \leq 1$, a channel null index satisfying $n_k - 2f_{\max} \leq \gamma_{m',i} \leq n_k + 2f_{\max}$, i.e. channel nulls at or adjacent to each null sub-carrier, can cause (101) to be zero for $f_o \neq f_{m'}$.

We prove that, in order to avoid identifiability loss, it is sufficient to have enough number of null sub-carriers ($> N_i$) with a judicious placement within the tile. From (99), it is clear that the null sub-carriers must not be placed on the edge of the tile in order to ensure identifiability and non-zero acquisition range. Therefore, if the number of tiles, i.e. $|\mathcal{S}_{m'}|$ allocated to m'^{th} user is greater than $P_{m'}$ with $N_k = 1$, the condition in (102) can only be satisfied for $f_o = f_{m'}$ and thus, identifiability is maintained. However, if $|\mathcal{S}_{m'}| < P_m$, which is usually the case for GSAS with a large value of N_s, and for SSAS with $|\mathcal{S}_{m'}| = 1$, a judicious null sub-carrier placement is required. We propose to use non-consecutive null sub-carriers in each tile or sub-band starting from the middle of the tile. In this way, the condition in (102) can be avoided and thus, identifiability will be maintained, provided $|\mathcal{S}_{m'}|N_k \geq P_{m'} \geq N_i$. This is because, if the number of null sub-carriers is greater than the channel order with at least one data sub-carrier between every two null sub-carriers and $n_k \neq 0, N_s - 1$, the set on the L.H.S in (102) must have some elements from $\mathcal{I}_{m'n}$. As $|f_o - f_{m'}| \leq 1$, it is possible only if $f_o = f_{m'}$.

This completes the discussion on the identifiability of null sub-carrier-based CFO estimation. We have shown that the number and placement of null sub-carrier plays an important role in the acquisition range and identifiability of CFO estimation in the presence of MUI and channel frequency selectivity. Thus, a designer can interleave data, pilot, and null sub-carriers to satisfy other system requirement, while following the guidelines of this contribution to guarantee identifiability and the required acquisition range. We have also shown that the algorithm is suited for both SSAS and GSAS. Null sub-carrier-based CFO estimation has also been proposed in [7] for SSAS. The null sub-carriers are used as guard-bands at the edges of the sub-band of each user to minimize the MUI and separate the users' signals through band-pass filtering. However, the presence of guard-band reduces the spectral efficiency of the OFDMA system. Moreover, its extension to GSAS is not straightforward because it

will lead to more complex filtering requirements and further reduction in the spectral efficiency. Also, [7] lacks rigorous analysis on the effect of MUI on the CFO estimation and the identifiability.

5.4 Refined CFO Estimation

In this section, we discuss the refined CFO estimation algorithm, which employs the channel estimation pilot sub-carriers in the OFDMA symbols. Pilot-aided CFO tracking or refined CFO estimation schemes have been proposed earlier in different contributions in the literature including [17,45,73]. However, these schemes have been used in single-user OFDM transmissions. The main advantage of pilot-aided CFO tracking is that no extra overhead is required for refined CFO estimation. Instead, already available pilot sub-carriers are used for CFO estimation, in addition to channel estimation.

As the proposed CFO estimation is performed before taking DFT at the receiver, CFO compensation can be performed before or after DFT. After CFO compensation and MUI cancelation, the BS proceeds with channel estimation using the pilot symbol inserted in each tile. Various CFO compensation algorithms proposed in the literature [11,29,47,89] can be used for this purpose. If the CFO estimation is accurate enough, these aforementioned schemes can be employed to minimize the MUI to a negligible level. Hence, for the ease of discussion, we ignore the effect of residual MUI after CFO compensation. The estimate of the received signal of the m'^{th} user, denoted as $\hat{\mathbf{Y}}_{m'}(q)$, can then be approximated as,

$$\hat{\mathbf{Y}}_{m'}(q) \approx e^{j\frac{2\pi}{N}(f_{m'}-\hat{f}_{m'})(qN_{\mathrm{t}}+N_{\mathrm{g}})}\mathbf{T}_{m'}^{H}\mathbf{F}_{N}\mathbf{D}_{N}(f_{m'}-\hat{f}_{m'})\mathbf{F}_{N}^{H}\mathbf{D}_{N}(\mathbf{H}_{m'})\mathbf{T}_{m'}\mathbf{S}_{m'}(q), \quad (103)$$

As CFO estimation cannot be perfect, the residual CFO error $(f_{m'}-\hat{f}_{m'})$ appears in (103). Although, $\mathbf{D}_N(f_{m'}-\hat{f}_{m'})$ in (103) can be approximated as an identity matrix for each symbol, provided the CFO estimation is accurate enough, the phase component $e^{j\frac{2\pi}{N}(f_{m'}-\hat{f}_{m'})(qN_{\mathrm{t}}+N_{\mathrm{g}})}$ increases as the symbol index increases, which severely

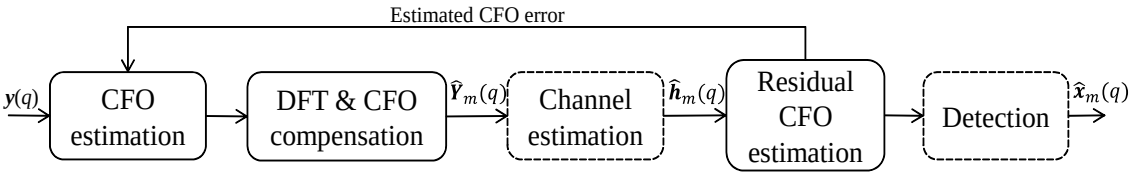

Figure 30: Block diagram of proposed CFO estimation.

affects the symbol detection performance. We propose to use the pilots sub-carriers to estimate this phase component arising due to residual CFO error, in addition to channel estimation. Moreover, we use the phase estimate to calculate the residual CFO error, which is used to update the CFO estimate of each user as shown in Figure 30.

Using (89), the received pilot sub-carriers $\mathbf{z}_{m'}(q)$ for the q^{th} received symbol of the m'^{th} user are extracted as,

$$\mathbf{z}_{m'}(q) = \mathbf{T}^{H}_{m'p}(q)\hat{\mathbf{Y}}_{m'}(q).$$

These received pilot symbols are used to perform channel estimation for the q^{th} OFDMA symbol in the tile. Various channel estimation techniques available in the literature [56] can be employed for this purpose. The phase rotation appearing in (103) for the q^{th} symbol is absorbed by the channel estimate for its corresponding symbol. However, for residual CFO estimation, we employ the channel estimate of the previous OFDMA symbol to equalize the pilot sub-carriers of the current symbol. Taking the example of the tile shown in Figure 31 for which pilot sub-carriers are present for $q = 1, Q-1$, let us denote the channel estimate of the first OFDMA symbol as $\hat{\mathbf{H}}_m(q=0)$. This channel estimate absorbs the phase rotation due to residual CFO error up till its corresponding OFDMA symbol. If we equalize the pilot sub-carriers of the $Q-1^{th}$ OFDMA symbol by $\hat{\mathbf{h}}_m(q=0)$, the equalized pilot sub-carriers will be given as,

$$\tilde{\mathbf{p}}_m(Q-1) = \mathbf{D}_P^{-1}(\hat{\mathbf{H}}_m(0))\mathbf{z}_m(Q-1) = e^{j\frac{2\pi}{N}(f_{m'}-\hat{f}_{m'})((Q-1)N_t)}\mathbf{p}_m(q),$$

As $\mathbf{p}_m(Q-1)$ is known at the BS, we can estimate the residual phase as,

$$\hat{\theta}(Q-1) = \sum_{i=0}^{N_{\mathrm{p}}|\mathcal{S}_m|-1} \mathrm{Im}\left(\ln \frac{[\tilde{\mathbf{p}}_m(Q-1)]_i}{[\mathbf{p}_m(Q-1)]_i}\right), \tag{104}$$

where $\mathrm{Im}(\cdot)$ represents the imaginary part. Note that this residual phase $\hat{\theta}$ can be used to estimate the residual CFO error as,

$$f_{m'} - \hat{f}_{m'} = \hat{\theta}(Q-1)\frac{N}{2\pi(Q-1)N_{\mathrm{t}}},$$

which is fed back to the CFO estimation block as shown in Figure 30 to refine the CFO estimate. We will show through simulation results in Section 5.6 that significant performance improvement can be achieved through residual CFO estimation, which shows that the approximation used in (103) for simplification in deriving the refined CFO estimation scheme has negligible implications in practice.

5.5 Adaptive Implementation and Computational Complexity

As the proposed algorithm employs line search for CFO estimation, the computational requirements can be very intense, as we will show later. However, adaptive estimation as suggested in [7,43] can also be used. Specifically, a gradient descent algorithm [66] is applied in order to find the CFO estimate iteratively as,

$$f_o(i+1) = f_o(i) - \mu\frac{\partial J_{m'}(f_o)}{\partial f_o} \tag{105}$$

where i is the iteration index and μ is the step size parameter. $\frac{\partial J_{m'}(f_o)}{\partial f_o}$ denotes the first order partial derivative of $J_{m'}(f_o)$ given as,

$$\frac{\partial J_{m'}(f_o)}{\partial f_o} = \frac{4\pi}{N}\mathrm{Re}\left[\mathbf{f}_N^H(f_o)\left(\sum_{i\in\mathcal{I}_{m'n}} \mathbf{D}_N^H(i)\mathbf{R}_{\mathbf{yy}}\mathbf{D}_N^H(i)\mathbf{D}_N(n)\right)\mathbf{f}_N^H(f_o)\right] \tag{106}$$

where $\mathbf{D}_N(n)$ is a diagonal matrix with vector $[0,\ldots,N-1]^T$ at its diagonal. The computational complexity of this adaptive implementation is much lower than the

line search-based implementation while the performance is comparable to line search as will be shown in Section 5.6. We now calculate the computational complexity of the proposed line search-based and adaptive CFO estimation algorithms in terms of number of complex multiplications required. We will also compare the complexity with [74]. Calculation of the sample estimate of the autocorrelation matrix in (90), using the first K OFDMA symbols containing the null sub-carriers, requires $\frac{1}{2}K(N^2+N)$ complex multiplication as it is a Hermitian matrix. The factor $\mathbf{D}_N^H(f_o)\mathbf{R_{yy}}\mathbf{D}_N(f_o)$ in (91) needs to be calculated once for each candidate CFO and requires $2N^2$ complex multiplications. Calculating the quadratic form corresponding to a null sub-carrier in (91) then requires N^2+N complex multiplications. If the number of candidate CFO values in the line search are N_c, the computation of the cost function in (91) for all users and for all candidate CFO values thus requires $2N_cN^2+\sum_{m=0}^{M-1}|\mathcal{S}_m|N_k(N^2+N)$ complex multiplications. Residual CFO estimation in Section 5.4 requires $\sum_{m=0}^{M-1}|\mathcal{S}_m|N_p$ complex multiplications. So, the total number of complex multiplications required for the line search-based CFO estimation are

$$2N_cN^2+N_k(N^2+N)\sum_{m=0}^{M-1}|\mathcal{S}_m|+N_p\sum_{m=0}^{M-1}|\mathcal{S}_m|+\frac{1}{2}K(N^2+N).$$

On the other hand, adaptive estimation in (106) requires $2N_kN^2\sum_{m=0}^{M-1}|\mathcal{S}_m|+MN_{it}(N^2+N)$ complex multiplications where N_{it} is the number of iterations. We use $N_{it}=20$ in our simulations. Thus the total computational requirement for adaptive estimation is

$$2N_kN^2\sum_{m=0}^{M-1}|\mathcal{S}_m|+MN_{it}(N^2+N)+N_p\sum_{m=0}^{M-1}|\mathcal{S}_m|+\frac{1}{2}K(N^2+N).$$

On the other hand, iterative CFO estimation proposed in [74] requires

$$N_i\left(N_cN(N_p\sum_{m=0}^{M-1}|\mathcal{S}_m|+1)+\mathcal{O}(N^3)\right),$$

complex multiplications. The typical value of N_i suggested in [74] is 2. A reasonable value for N_c is 1000 in order to ensure satisfactory CFO estimation accuracy for line

search. As an example, for the tile structure shown in Figure 26 with $N = 128$, $M = 4$, $K = 2$,and $\mathcal{S}_m = 6$ for each m, adaptive implementation provides 93% savings as compared to line search and 80% savings as compared to [74]. On the other hand, CFO estimation in [74] requires 68% less computations than the line search-based CFO estimation. It is also important to note that [74] does not include the complexity of computing N_c number of $N \times N$ complex valued matrices assuming that these matrices can be pre-calculated and pre-stored for CFO estimation. However, for large values of N_c (around 1000) and N (which is usually the case in OFDMA systems), the memory requirements for pre-storage can be prohibitively large. If we consider on-line computation of these matrices, the complexity of [74] is higher than the proposed line search-based algorithm as well. However, [74] requires less pilot over-head as it does not require dedicated pilot sub-carriers for CFO estimation because pilots inserted for channel estimation are used for CFO estimation as well.

5.6 Simulation Results

In this section, we evaluate the performance of the proposed algorithm and compare it with the existing approaches in the literature through Monte Carlo simulations. The simulation parameters are given as follows: the total number of sub-carriers $N = 128$, sub-carrier spacing $\Delta f = 15$ kHz, the number of users $M_u = M = 4$, and CP length $N_{\mathrm{g}} = \frac{N}{8}$. The modulation type is QPSK. Each user's channel is modeled as an independent Rayleigh fading channel with exponential PDP and order $L_m = 6$. The CFO f_m for each user is generated as a uniform random variable from $[-0.4, 0.4]$. We use two different IEEE 802.16 like, tile structures shown in Figure 31 with number of OFDMA symbols $Q = 3$, number of sub-carriers $N_s = 5, 4$, and number of tiles $|S_m| = 6, 8$ for each user, respectively. The tiles of different users are interleaved into each other. The number of candidate CFO values used in the line search is 1000. Each uplink frame contains 36 OFDMA symbols, with null sub-carriers in the first two

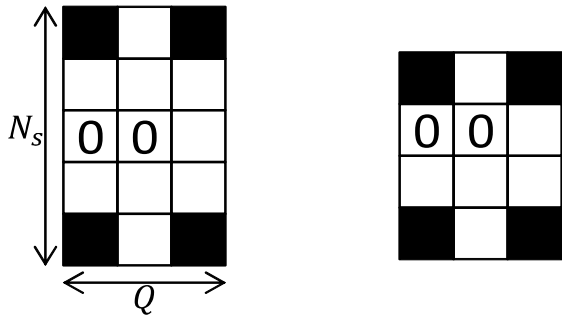

Figure 31: Tile structures used in the simulations.

symbols, as $K = 2$ in Figure 31. For residual CFO estimation, CFO compensation scheme proposed in [11] is employed.

5.6.1 Performance of CFO Estimation

The accuracy of the proposed line search-based and adaptive CFO estimation is shown using MSE of the CFO estimation in Figure 32 for the two tile configurations. As the tile configuration with $N_s = 4$ contains more null and pilot sub-carrier, it has better performance as compared to $N_s = 5$. Moreover, the performance of adaptive estimation is worse than the line search for lower SNRs ($0 - 5$ dB) while it matches the line search at moderate and high SNRs. The figure also shows the significant effect of residual CFO estimation using the pilot sub-carriers. Note that refined CFO estimation uses the already available pilot sub-carriers in the first tile. Hence the extra overhead required in the proposed CFO estimation is only the null sub-carriers in the first K OFDMA symbols. If there are N_o OFDMA symbols in the frame, the total null sub-carrier overhead is only $\frac{M|S_m|N_kK}{N_oN}$ which, in the simulation setup, amounts to less than 2% overhead for both tile configurations.

Effect of increasing acquisition range Figure 33 shows the effect of increasing the maximum possible CFO value, i.e., $f_{\max}$ on CFO estimation for the tile with $N_s = 5$ and two different SNR values. The CFO of each user for each $f_{\max}$ is a uniform random variable chosen from $[-f_{\max}, f_{\max}]$. Large $f_{\max}$ increases the MUI on the null

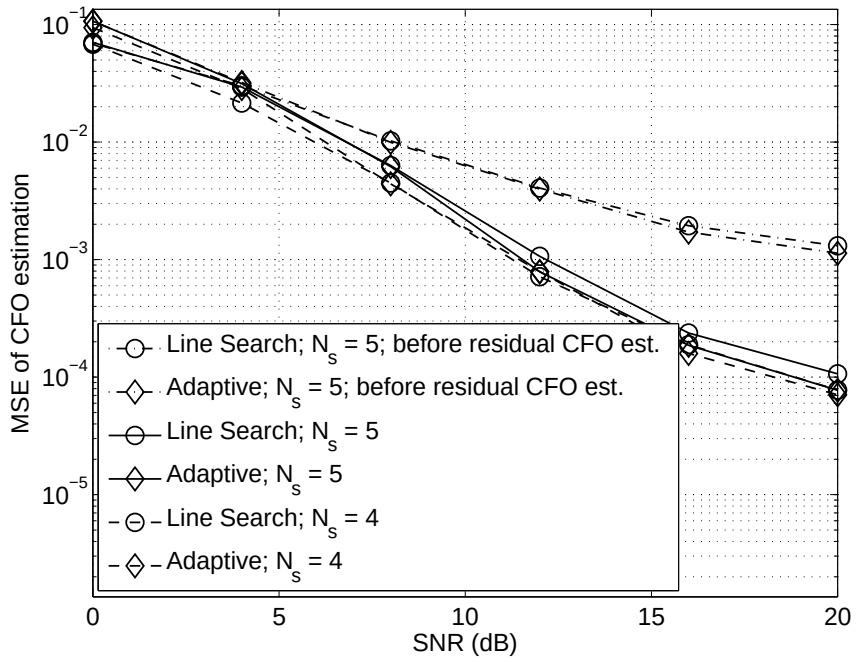

Figure 32: Performance of the proposed CFO estimation for different tile configurations.

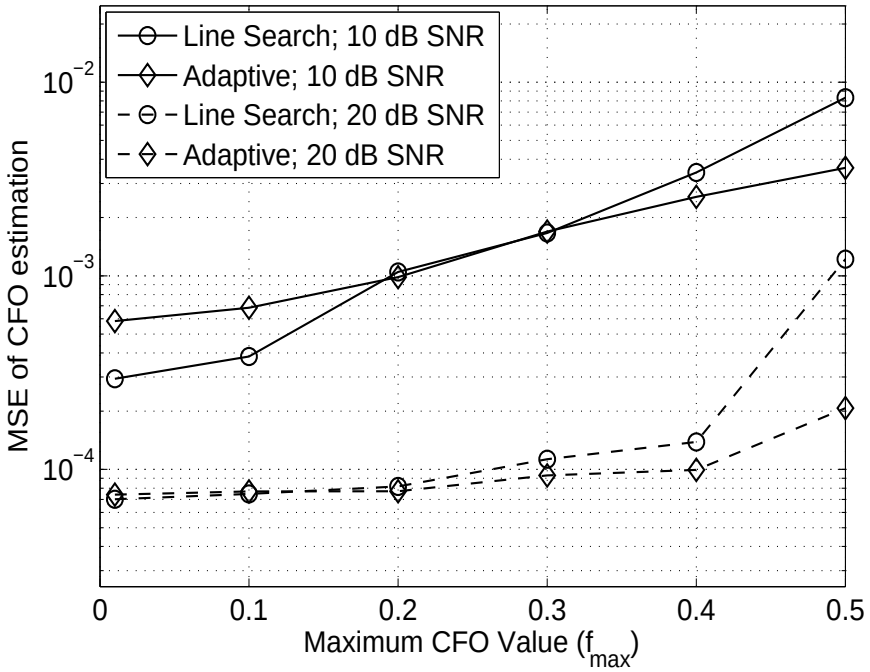

Figure 33: Effect of increasing acquisition range on CFO estimation performance.

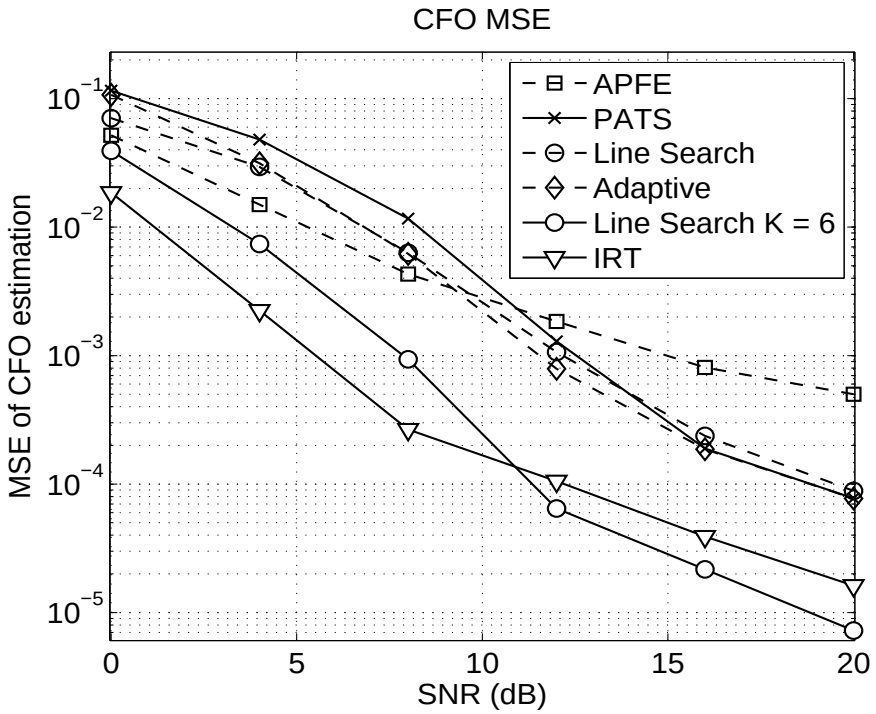

Figure 34: Performance comparison of the proposed CFO estimation with [74] and [61] in the presence of equal power users.

sub-carriers and thus, the CFO estimation performance degrades. However, as shown in the figure, adaptive estimation is more robust to change in $f_{\max}$ as compared to line search. This is because the number of candidate CFO values is fixed for line search. Therefore, the accuracy of line search decrease as the $f_{\max}$ increases. The performance of line search can be improved at higher $f_{\max}$ by increasing the number of candidate CFO values but, at a price of higher computational complexity.

Performance comparison with equal power users Figure 34 shows the performance comparison of the proposed CFO estimation schemes with the existing schemes proposed in [61,65,74] for the tile with $N_s = 5$. It is assumed that the power of all users is same. [61] uses the first OFDMA symbol as a training symbol and the proposed scheme is denoted as the Alternating-Projection Frequency Estimator (APFE). [74] proposes pilot-based CFO estimation (denoted as PATS) and the null sub-carriers shown in Figure 31 are replaced by the pilot sub-carriers for fair comparison. When

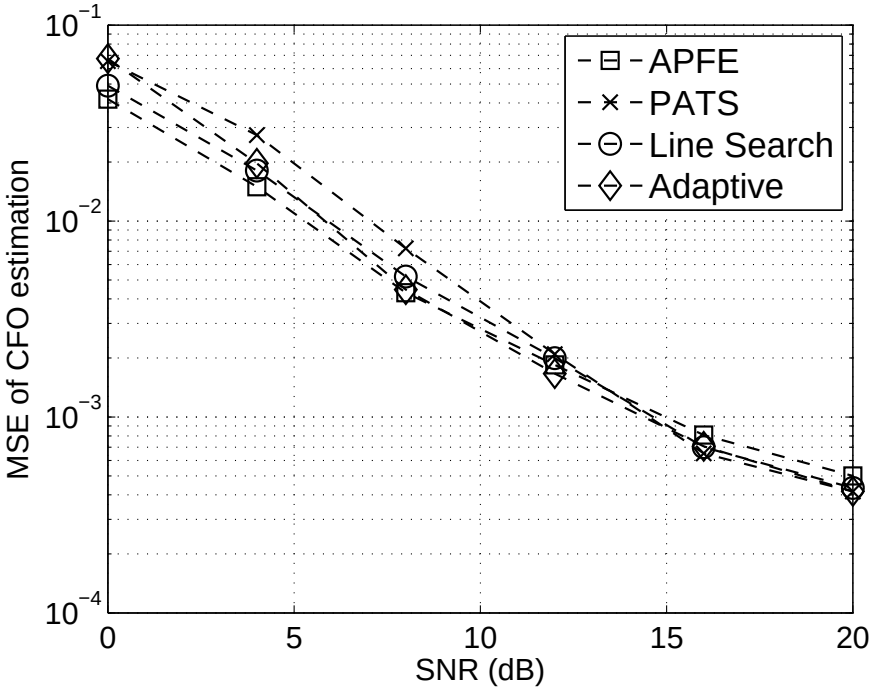

Figure 35: Performance comparison of the proposed CFO estimation with [74] and [61] in the presence of near-far effect.

compared to APFE, the performance of the proposed CFO estimation is better at moderate and high SNRs while APFE is better for low SNRs. On the other hand, proposed CFO estimation performs better than PATS for low and moderate SNRs while the performance is comparable at high SNRs. The method proposed in [65] (denoted as IRT) uses at least two identical training symbols with sub-carriers designed to reduce the MUI in the presence of CFOs. We use $K = 6$ while comparing the performance with [65] for fair comparison as two training symbols required in [65] imply larger number of training sub-carriers as compared to $K = 2$. As shown, the performance of IRT is better for low SNRs while the performance of the proposed algorithm is better for higher SNRs.

Performance comparison with near-far effect We now compare the performance of the proposed schemes in the presence of users with un-equal power. For each iteration of Monte Carlo simulation, two randomly chosen users have 6 dB more

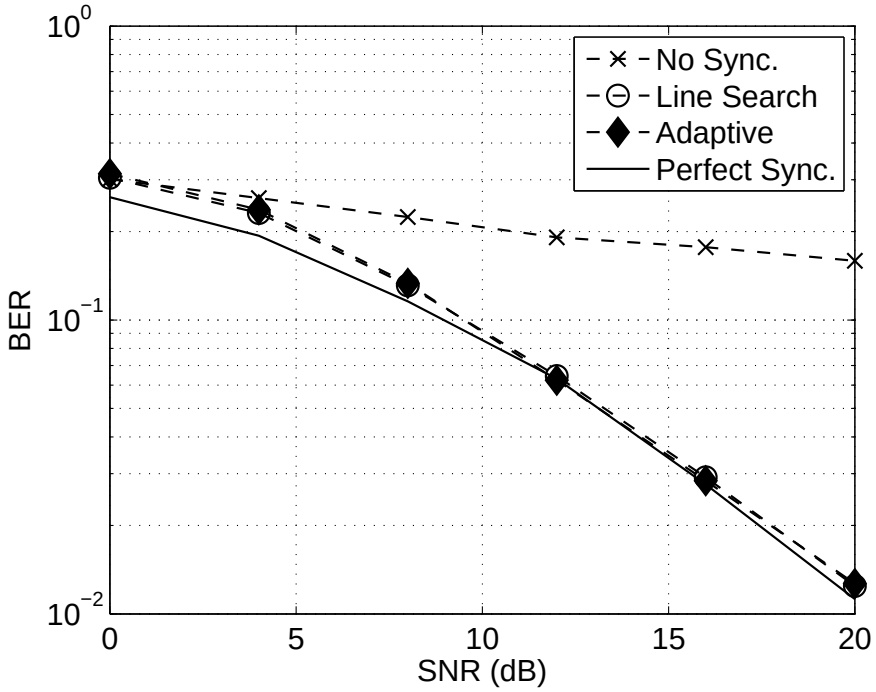

Figure 36: BER comparison of the proposed CFO estimation.

power than the other two. Figure 35 shows the performance comparison for the tile with $N_s = 5$. As shown in the figure, the performance of all schemes is slightly affected by the un-equal power of the users at high SNRs. However, the performance trends are similar to the equal power case. This shows the effectiveness of the proposed CFO estimation scheme.

5.6.2 Bit Error Rate Performance

In Figure 36, we evaluate the performance of the proposed algorithm in term of BER. We also show the performance with no synchronization, i.e., without CFO estimation and compensation, and with ideal synchronization in which the BS knows the exact value of CFO of each user. As shown, the BER of the proposed algorithms exhibits about dB gap from the ideal case for low SNRs while catches up at moderate and high SNRs. Also, the BER difference between line search and adaptive estimation is almost negligible. This shows the effectiveness of the proposed schemes as they

perform fairly close to the ideal transmission scenario.

CHAPTER VI

FREQUENCY SYNCHRONIZATION FOR UPLINK SC-FDMA TRANSMISSIONS

This Chapter presents a joint CFO estimation and compensation scheme for SC-FDMA UL transmissions with ISAS using parallel-factor (PARAFAC) analysis method [18]. PARAFAC, an extension of matrix decomposition to tensors, has found numerous applications in signal processing including multi-user detection [55, 71], array signal processing [70], and CFO estimation for DL OFDM systems [31]. Employing identical training symbols and exploiting the structure of transmitted SC-FDMA signals, we show that in the presence of CFOs, the signal received at the BS can be formulated as the PARAFAC model. This key observation allows us to apply tensor decomposition methods to jointly retrieve the estimates of CFO and the MUI-free received training symbol corresponding to each user. The formulation also allows us to perform low-complexity CFO compensation for subsequent data symbols. We prove that the proposed algorithm guarantees the identifiability of CFO estimation while allowing the system to operate on full load as opposed to [12, 37, 92]. In addition, the proposed algorithm can be readily extended to multi-antenna BS reception and offers better performance as compared to the existing approaches in the literature.

6.1 SC-FDMA Signal Description

Consider a baseband equivalent system model of SC-FDMA UL transmissions as described in Section 2.2.1 where M active users transmit to a BS using ISAS. Maximum number of users allowed in the system is denoted as M_u. Total number of sub-carriers is denoted as N while number of sub-carriers allocated to each user is $R = \frac{N}{M_u}$. The

transmission takes place in the form of frames where each frame contains a block of Q identical SC-FDMA training symbols followed by data symbols. The block diagram of the SC-FDMA system is shown in Figure 3.

6.1.1 Transmitted Signal Structure

As ISAS is employed, the exclusive set of sub-carriers allocated to the m^{th} user, $0 \leq m \leq M-1$ is denoted as $\mathcal{I}_m := \{v_m + rM_u \mid 0 \leq r \leq R-1\}$, where v_m is the unique starting index of the m^{th} user. The q^{th} SC-FDMA training symbol contains R training points, which are pre-coded by an R point DFT and then mapped to the sub-carriers allocated to the m^{th} user. Thus, the k^{th} sub-carrier, $0 \leq k \leq N-1$, of the q^{th} training symbol transmitted by the m^{th} user is given as,

$$X_m[q,k] = \begin{cases} \frac{1}{\sqrt{R}} \sum_{r'=0}^{R-1} s_m[r'] e^{-j\frac{2\pi}{R}r'\left(\frac{k-v_m}{M_u}\right)} & k \in \mathcal{I}_m, \\ 0 & k \notin \mathcal{I}_m, \end{cases} \tag{107}$$

As the Q training symbols are identical, we drop the index q in $s_m[r']$. A N point IDFT of $X_m[q,k]$, $0 \leq k \leq N-1$, is then computed to generate the q^{th} SC-FDMA training symbol in time domain with n^{th} sample given as,

$$x_m[q,n] = \frac{1}{\sqrt{N}} \sum_{k=0}^{N-1} X_m[q,k] e^{j\frac{2\pi}{N}kn}, \quad 0 \leqslant n \leqslant N-1. \tag{108}$$

As $X_m[q,k]$ is non-zero only for $k \in \mathcal{I}_m$,

$$x_m[q,n] = \frac{1}{\sqrt{N}} \sum_{r=0}^{R-1} X_m[q, v_m + rM_u] e^{j\frac{2\pi}{N}(v_m + rM_u)n}, \quad 0 \leqslant n \leqslant N-1. \tag{109}$$

Using (107), (109) can be written as,

$$\begin{aligned} x_m[q,n] &= \frac{1}{\sqrt{NR}} e^{j\frac{2\pi}{N}v_m n} \sum_{r'=0}^{R-1} s_m[r'] \sum_{r=0}^{R-1} e^{j\frac{2\pi}{R}(n-r')r} \\ &= \frac{1}{\sqrt{M_u}} e^{j\frac{2\pi}{N}v_m n} \sum_{r'=0}^{R-1} s_m[r'] \delta\left[(n)_R - r'\right] \\ &= \frac{1}{\sqrt{M_u}} e^{j\frac{2\pi}{N}v_m n} s_m[(n)_R], \quad 0 \leqslant n \leqslant N-1. \end{aligned} \tag{110}$$

Eq. (110) shows that the transmitted SC-FDMA signal of the m^{th} user contains M_u copies of the original signal $s_m[r], 0 \leq r \leq R-1$ scaled by the phase term corresponding to the starting index of the user.

6.1.2 Received Signal Structure

We assume quasi-synchronous transmissions as discussed in Section 2.2.1 so that the TO of each MU can be incorporated in its effective channel $h_m[p],\ 0 \leq p \leq P-1$ given in (11). Thus, after CP removal, the n^{th} sample of the q^{th} received SC-FDMA symbol at the BS is the sum of the M SC-FDMA symbols transmitted by the MUs and given as

$$y[q,n] = \sum_{m=0}^{M-1} e^{j\frac{2\pi}{N} f_m (qN_t + N_g + n)} \sum_{p=0}^{P-1} h_m[p] x_m[q, (n-p)_N] + w[q,n], \tag{111}$$

where f_m is the CFO between the m^{th} user and the BS, $N_t = N + N_g$, and $w[q,n]$ represents the corresponding AWGN sample. We assume that $|f_m| < 0.5,\ \forall m$. Using (110), (111) can be written as,

$$y[q,n] = \frac{1}{\sqrt{M_u}} \sum_{m=0}^{M-1} e^{j\frac{2\pi}{N} f_m (qN_t + N_g + n)} e^{j\frac{2\pi}{N} v_m n} \sum_{p=0}^{P-1} h_m[p] e^{-j\frac{2\pi}{N} v_m p} s_m[(n-p)_R] + w[q,n]. \tag{112}$$

If the effective channel length $P \leq R$, the inner sum in (112) is also periodic with period R. If we denote

$$y_m[r] = \frac{1}{\sqrt{M_u}} \sum_{p=0}^{P-1} h_m[p] e^{-j\frac{2\pi}{N} v_m p} s_m[(r-p)_R], \tag{113}$$

which is the circular convolution of the scaled channel, i.e., $h_m[p]e^{-j\frac{2\pi}{N} v_m p}$, and the training symbol $s_m[r], 0 \leq r \leq R-1$, then (112) can be written as

$$y[q,n] = \sum_{m=0}^{M-1} e^{j\frac{2\pi}{N} q f_m N_t} e^{j\frac{2\pi}{N} \gamma_m} e^{j\frac{2\pi}{N} \phi_m n} y_m[(n)_R] + w[q,n] \tag{114}$$

where $\phi_m = f_m + v_m$ and $\gamma_m = f_m N_g$. Thus, the received signal is also periodic except for the phase terms introduced by the CFOs and the starting indices. This periodicity

helps to formulate the received signal as PARAFAC analysis model as described in the next section.

6.2 CFO Estimation and Compensation for SC-FDMA UL with ISAS

In this section, we present the proposed CFO estimation and compensation algorithms for SC-FDMA UL transmissions. As the proposed scheme is based on PARAFAC analysis, we start by showing that the received signal in (114) can be formulated as a PARAFAC model, which will allow us to apply tensor decomposition algorithms to estimate the CFO and the MUI-free signal of each user. For an introduction to PARAFAC, refer to [18, 71].

6.2.1 SC-FDMA UL as a PARAFAC model

If we stack the periods of the q^{th} received signal in (114) in an $M_u \times R$ matrix

$$\mathbf{Y}(q) = \begin{bmatrix} y[q,0] & y[q,1] & \dots & y[q,R-1] \\ y[q,R] & y[q,R+1] & \dots & y[q,2R-1] \\ \cdot & \cdot & \dots & \cdot \\ \cdot & \cdot & \dots & \cdot \\ y[q,N-R] & y[q,N-R+1] & \dots & y[q,N-1] \end{bmatrix}_{M_u \times R},$$

then $\mathbf{Y}(q)$ can be expressed as

$$\mathbf{Y}(q) = \mathbf{A}\mathbf{D}_M(q)\mathbf{C}^T + \mathbf{W}(q), \tag{115}$$

where

$$\mathbf{A} = \begin{bmatrix} 1 & 1 & \dots & 1 \\ e^{j\frac{2\pi}{M_u}\phi_0} & e^{j\frac{2\pi}{M_u}\phi_1} & \dots & e^{j\frac{2\pi}{M_u}\phi_{M-1}} \\ \cdot & \cdot & \dots & \cdot \\ \cdot & \cdot & \dots & \cdot \\ e^{j\frac{2\pi}{M_u}\phi_0(M_u-1)} & e^{j\frac{2\pi}{M_u}\phi_1(M_u-1)} & \dots & e^{j\frac{2\pi}{M_u}\phi_{M-1}(M_u-1)} \end{bmatrix}_{M_u \times M}, \tag{116}$$

$$\mathbf{C} = \begin{bmatrix} e^{j\frac{2\pi}{N}\gamma_0} y_0[0] & \dots & e^{j\frac{2\pi}{N}\gamma_{M-1}} y_{M-1}[0] \\ e^{j\frac{2\pi}{N}(\phi_0+\gamma_0)} y_0[1] & \dots & e^{j\frac{2\pi}{N}(\phi_{M-1}+\gamma_{M-1})} y_{M-1}[1] \\ . & \dots & . \\ . & \dots & . \\ e^{j\frac{2\pi}{N}((R-1)\phi_0+\gamma_0)} y_0[R-1] & \dots & e^{j\frac{2\pi}{N}((R-1)\phi_{M-1}+\gamma_{M-1})} y_{M-1}[R-1] \end{bmatrix}_{R\times M}, \tag{117}$$

and $\mathbf{D}_M(q)$ is a $M \times M$ diagonal matrix with diagonal entries $e^{j\frac{2\pi}{N} f_m q N_t} \quad 0 \leqslant m \leqslant M-1$, and $\mathbf{W}(q)$ is an $M_u \times R$ matrix containing the corresponding AWGN samples.

As the Q training symbols are identical, stacking all $\mathbf{Y}(q)$ matrices corresponding to the Q received training symbols results in a $QM_u \times R$ matrix expressed as

$$\mathbf{Y}^Q = \begin{bmatrix} \mathbf{Y}(0) \\ \mathbf{Y}(1) \\ . \\ . \\ \mathbf{Y}(Q-1) \end{bmatrix} = \begin{bmatrix} \mathbf{A}\mathbf{D}_M(0) \\ \mathbf{A}\mathbf{D}_M(1) \\ . \\ . \\ \mathbf{A}\mathbf{D}_M(Q-1) \end{bmatrix} \mathbf{C}^T + \begin{bmatrix} \mathbf{W}(0) \\ \mathbf{W}(1) \\ . \\ . \\ \mathbf{W}(Q-1) \end{bmatrix}, \tag{118}$$

or

$$\mathbf{Y}^Q = (\mathbf{B} \odot \mathbf{A})\mathbf{C}^T + \mathbf{W}^Q, \tag{119}$$

where $\odot$ represents the Khatri-Rao product [18] and

$$\mathbf{B} = \begin{bmatrix} 1 & \dots & 1 \\ e^{j\frac{2\pi}{N} f_0 N_t} & \dots & e^{j\frac{2\pi}{N} f_{M-1} N_t} \\ . & \dots & . \\ . & \dots & . \\ e^{j\frac{2\pi}{N} f_0 (Q-1) N_t} & \dots & e^{j\frac{2\pi}{N} f_{M-1}(Q-1) N_t} \end{bmatrix}. \tag{120}$$

is a $Q \times M$ matrix with q^{th} row containing the diagonal entries of $\mathbf{D}_M(q)$. Similarly it can be shown that

$$\mathbf{Y}^R = (\mathbf{C} \odot \mathbf{B})\, \mathbf{A}^T + \mathbf{W}^R, \tag{121}$$

where $\mathbf{Y}^R$ is a $RQ \times M_u$ matrix, which is a concatenation of R matrices with r^{th} matrix given as

$$\begin{bmatrix} y[0,r] & y[0,r+R] & \dots & y[0,r+(M_u-1)R] \\ y[1,r] & y[1,r+R] & \dots & y[1,r+r+(M_u-1)R] \\ \cdot & \cdot & \dots & \cdot \\ \cdot & \cdot & \dots & \cdot \\ y[Q-1,r] & y[Q-1,r+R] & \dots & y[Q-1,r+(M_u-1)R] \end{bmatrix}_{Q\times M_u},$$

and

$$\mathbf{Y}^{M_u} = (\mathbf{A} \odot \mathbf{C})\,\mathbf{B}^T + \mathbf{W}^{M_u}, \tag{122}$$

where $\mathbf{Y}^{M_u}$ is an $M_u R \times Q$ matrix with $Y^{M_u}[n,q] = y[q,n]$. In the absence of noise, (119), (121), and (122) form the PARAFAC model of three-way tensors with rank M [18], which allows us to apply tensor decomposition algorithms to obtain estimates of $\mathbf{A}$, $\mathbf{B}$, and $\mathbf{C}$, denoted as $\hat{\mathbf{A}}$, $\hat{\mathbf{B}}$, and $\hat{\mathbf{C}}$, respectively. The details of the algorithms along with the discussion on computational requirements is deferred to Section 6.4. The CFO estimate and the MUI-free received signal estimate corresponding to each user can then be extracted from $\hat{\mathbf{A}}$, $\hat{\mathbf{B}}$, and $\hat{\mathbf{C}}$ as discussed in the following sections. We refer to (119), (121), and (122) collectively as the PARAFAC model. A key advantage of employing the PARAFAC model is that the uniqueness of the signal decomposition in the PARAFAC model and thus, identifiability of CFO estimation can be guaranteed.

6.2.2 Identifiability of CFO Estimation

We now discuss the conditions, which guarantee the identifiability of CFO estimation by using the uniqueness properties of the PARAFAC model. Identifiability refers to the uniqueness of the CFO estimates. Guaranteeing the identifiability of CFO estimation is an important requirement as channel frequency selectivity as well as MUI can affect the identifiability of CFO estimation as shown in Chapter 5 and [22, 43].

A key advantage of applying the PARAFAC model is that its uniqueness can be guaranteed. A sufficient condition is presented in [35], which says that the decomposition in (119) is unique up to scaling and column permutation if

$$k_{\mathbf{A}} + k_{\mathbf{B}} + k_{\mathbf{C}} \geq 2(M+1), \tag{123}$$

where $k_{\mathbf{A}}$ denotes the k-rank of $\mathbf{A}$. Specifically, if rank($\mathbf{A}$) $= M$ and every $l \leq M$ columns of $\mathbf{A}$ are linearly independent, then the k-rank of $\mathbf{A}$ is l [71]. We now investigate the k-rank of the matrices involved in the proposed PARAFAC model for the SC-FDMA UL in (119). Recall that $\phi_m = v_m + f_m$ in (116). As the CFO of each user in UL transmissions is fractional, i.e., $f_m < 0.5\ \forall m$ as mentioned in Section 6.1, and the starting index v_m of each user is unique, $v_m - 0.5 < \phi_m < v_m + 0.5$ in (116) lies in a unique interval for each user. Moreover, as the CFO is a continuous random variable, the probability that the CFOs of two different user is same is zero. Therefore, using the fact that $\mathbf{A}$ and $\mathbf{B}$ are Vandermonde matrices, both matrices have full k-rank, i.e., $k_{\mathbf{A}} = \min(M_u, M) = M$ and $k_{\mathbf{B}} = \min(Q, M)$. Similarly it can be shown that the matrix $\mathbf{C}$ in (117) has full k-rank if the training symbols $s_m(r), 0 \leq r \leq R-1$ and channel of different users are un-correlated from each other. In that case, $k_{\mathbf{C}} = \min(R, M)$. If $R \geq M$, which is usually the case in broadband wireless systems, the condition in (123) can be satisfied for $Q \geq 2$. Thus, provided $R \geq M$, $\mathbf{A}$, $\mathbf{B}$ and $\mathbf{C}$ can be uniquely estimated up to scaling and column permutation by transmission of only two identical training symbols. For BSs equipped with multiple antennas, the condition $R \geq M$ can be relaxed as discussed in Section 6.3.

As the PARAFAC decomposition is unique only up to scaling and column permutations, matching the columns to the respective users is required once the estimates of the matrices are available. Also the scaling of $\hat{\mathbf{C}}$ must be identified and corrected. As each entry of $\mathbf{A}$ and $\mathbf{B}$ is a complex exponential, any scaling of columns of $\hat{\mathbf{A}}$ and $\hat{\mathbf{B}}$ can be easily identified. The scaling of the columns of $\hat{\mathbf{C}}$ can then be rectified by

dividing each column with the product of the scaling of respective columns of $\hat{\mathbf{A}}$ and $\hat{\mathbf{B}}$. As $\phi_m = v_m + f_m$ lies in a unique interval for each user, as discussed earlier, any column permutation can also be easily identified through $\hat{\mathbf{A}}$. Specifically, the index of the column of $\hat{\mathbf{A}}$ corresponding to the m^{th} user, denoted as c_m is give as

$$c_m = \arg\min_{m'} \left| \frac{M_u}{2\pi} \angle \left(\frac{1}{M_u - 1} \sum_{u=1}^{M_u - 1} \frac{\hat{A}[u, m']}{\hat{A}[u-1, m']} \right) - v_m \right| \tag{124}$$

6.2.3 CFO Estimation Using PARAFAC

As both $\mathbf{A}$ and $\mathbf{B}$ depend on CFO, $\hat{\mathbf{A}}$ and/or $\hat{\mathbf{B}}$ can be employed for CFO estimation after correction of scaling and column permutation. We use the entries of $\hat{\mathbf{B}}$, and the CFO of the m^{th} user is estimated as,

$$\hat{f}_m = \frac{N}{2\pi N_t} \angle \left(\frac{1}{Q-1} \sum_{q=1}^{Q-1} \frac{\hat{B}[q, m]}{\hat{B}[q-1, m]} \right) \tag{125}$$

Thus, the acquisition range of CFO estimation is $f_{\max} = \frac{N}{2N_t}$ sub-carrier spacings.

The CFO estimation schemes proposed in [12,37,92] cannot operate on fully loaded systems and require either CP extension or multiple antenna-BSs to support full load. However, the proposed CFO estimation is independent of the number of active user and thus, provides better spectral efficiency as compared to existing algorithms.

It is now clear that the proposed CFO estimation only requires the transmissions of at least two identical training symbols. The idea of identical training signals has been employed before in timing and carrier synchronization for OFDM system, e.g., see [67]. Also, two out of four preambles employed in random-access in LTE-Advanced contain two identical symbols [40]. However, it is important to note that the knowledge of actual data transmitted on the sub-carriers of the training signals is not required for CFO estimation. Thus, the proposed scheme can be refered as a semi-blind CFO estimation and the training signal can be designed to optimize other receiver tasks such as timing synchronization and/or channel estimation.

6.2.4 CFO Compensation for the Training Symbol

Apart from CFO estimates obtained through $\hat{\mathbf{A}}$ and $\hat{\mathbf{B}}$, the PARAFAC model also provides the estimate of $\mathbf{C}$, whose columns contain MUI-free received signals corresponding to each user. Thus, another advantage of PARAFAC decomposition is that it automatically decouples user's received training signals, and CFO compensation can be performed for each user separately to recover $y_m[r]$ $0 \leq r \leq R-1$ in (113). Specifically

$$\hat{y}_m[r] = e^{-j\frac{2\pi}{N}(r\phi_m+\gamma_m)}\hat{C}[r,m] \tag{126}$$

Once the CFO compensated training signal of each user is available, it can be employed for channel estimation. Standard channel estimation techniques, like least squares (LS) or minimum mean squared error (MMSE) channel estimation [56] are applicable to the estimate of the received training signal in (126).

6.2.5 CFO Compensation for the Data Symbols

In this section, we present the CFO compensation scheme for SC-FDMA data symbols following the training symbols. As the proposed PARAFAC model requires multiple identical training symbols, PARAFAC decomposition algorithms cannot be employed for CFO compensation of data symbols following the training, for data symbols cannot be identical. However, the received data symbols still satisfy (115) with $\mathbf{C}$ replaced by a symbol-dependent matrix $\mathbf{C}(q)$ whose columns contain the q^{th} MUI-free received data symbols of the MUs. As the receiver has already estimated the CFOs, it has the knowledge of $\hat{\mathbf{A}}$ and $\hat{\mathbf{D}}_M(q)$ in (115), and $\mathbf{C}(q)$ for the q^{th} data SC-FDMA symbol can estimated as

$$\hat{\mathbf{C}}(q) = \left(\mathbf{D}_M^{-1}(q)\hat{\mathbf{A}}^{\dagger}\mathbf{Y}(q)\right)^T, \tag{127}$$

where $\mathbf{A}^{\dagger}$ denotes the pseudo-inverse of $\mathbf{A}$. CFO compensation for each user can then be performed separately using (126). Thus, the formulation of the received signal in

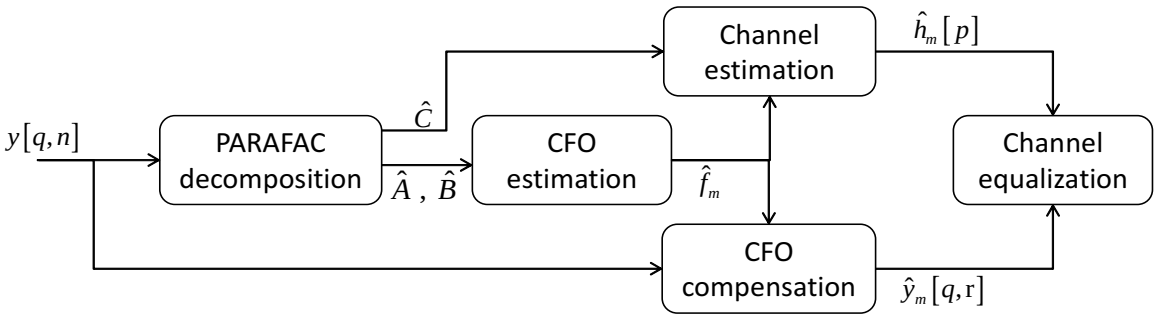

Figure 37: Block diagram of the proposed SC-FDMA UL receiver.

(115), leading to the PARAFAC model, also allows us to design a time-domain CFO compensation scheme for data symbols using (127) and (126).

Complexity analysis of CFO compensation We now calculate the computational requirements of the proposed CFO compensation scheme under full load and compare it with some of the existing schemes in the literature. Complexity analysis of PARAFAC decomposition for CFO estimation is discussed in Section 6.4. Calculation of $\hat{\mathbf{C}}(q)$ in (127) requires inversion of $\hat{\mathbf{A}}$, which can be efficiently implemented using the fact that $\mathbf{A}$ is Vandermonde matrix and a closed form solution for its inverse exists with a complexity of only $O(M_u^2)$ operations [21]. Thus, the total computational load of (127) and (126) is $O((N+1)M_u + M_u^2)$. In contrast, the time-domain CFO compensation scheme in [94] requires the inversion of an $N \times N$ block-diagonal matrix with $O(M_u^2 N + N^2)$ operations while the linear de-correlation-based frequency-domain CFO compensation scheme in [11] requires inversion of an $N \times N$ matrix with $O(N^3)$ operations. The complexity of CFO compensation in [11] can be lowered by a banded-matrix approximation at the cost of performance degradation. Thus, compared with the existing schemes, the proposed CFO compensation has the advantage of significantly reduced computational complexity.

This completes the discussion on the proposed CFO estimation and compensation techniques, and the block diagram of the proposed algorithms is shown in Figure 37. We now discuss the extension of the proposed algorithm to multi-antenna BS

reception.

6.3 Extension to Multi-Antenna BS Case

In this section, we show that the proposed synchronization schemes can be readily extended to the case where the BS has multiple antennas. Specifically, if the BS has N_r receive antennas, we denote the parameters associated with the t^{th} antenna by using the subscript 't'. Thus, $y[q,n]$, $y_m[r]$ and $h_m[p]$ in (113) and (114) are replaced by $y_t[q,n]$, $y_{t,m}[r]$, and $h_{t,m}[p]$, respectively. We assume that the channels between a user and different receive antennas are independent. However, receive antennas are collocated, and all receive chains are assumed to employ a common clock, which implies that the CFO across receiver chains remains constant. This allows us to employ the PARAFAC model in (119) for the multi-antenna BS case with $\mathbf{A}$ and $\mathbf{B}$ unchanged as in (116) and (120), respectively, while $\mathbf{Y}^Q$ in (119) is updated as

$$\mathbf{Y}^Q = \begin{bmatrix} \mathbf{Y}_0(0) & \mathbf{Y}_1(0) & \dots & \mathbf{Y}_{N_r-1}(0) \\ \mathbf{Y}_0(1) & \mathbf{Y}_1(1) & \dots & \mathbf{Y}_{N_r-1}(1) \\ . & . & \dots & . \\ . & . & \dots & . \\ \mathbf{Y}_0(Q-1) & \mathbf{Y}_1(Q-1) & \dots & \mathbf{Y}_{N_r-1}(Q-1) \end{bmatrix}_{M_u \times N_r R}, \tag{128}$$

which is a concatenation of $Y_t(q)$ in (115) corresponding to different receiver antennas. Correspondingly, $\mathbf{C}$ in (117) is updated as

$$\mathbf{C} = \begin{bmatrix} \mathbf{C}_0 \\ \mathbf{C}_1 \\ . \\ . \\ \mathbf{C}_{N_r-1} \end{bmatrix}_{N_r R \times M}, \tag{129}$$

with the element in r^{th} row and m^{th} column of $\mathbf{C}_t$ given as

$$C_t[r,m] = e^{j\frac{2\pi}{N}((r-1)\phi_{m-1}+\gamma_{m-1})} y_{t,m-1}[r-1].$$

Thus, the PARAFAC model is still applicable to the multi-antenna BS reception, and tensor decomposition can still be applied to jointly estimate the CFOs and MUI-free received signal corresponding to different users and receive antennas. A better CFO estimation performance is expected in this case due to more information brought by the additional receive chains at the cost of increased computational complexity.

As the dimensions of $\mathbf{C}$ in (129) grow to $N_r R \times M$ for multi-antenna BS as opposed to $R \times M$ in (117) for single-antenna BS, the k-rank of $\mathbf{C}$ is given as $k_{\mathbf{C}} = \min(N_r R, M)$. Thus, according to the discussion in Section 6.2.2, identifiability of CFO estimation in multi-antenna BS case is guaranteed if $N_r R \geq M$, which is a less restrictive condition as compared to $R \geq M$ for single-antenna BS. Moreover, the CFO compensation scheme presented in Section 6.2.5 is also applicable to multi-antenna reception. Since $\mathbf{A}$ and $\mathbf{B}$ remain un-changed, $\mathbf{A}^{\dagger}$ in (127) needs to be calculated only once for CFO compensation corresponding to all receive antennas. Thus, the complexity of CFO compensation increases only linearly with respect to the number of receive antennas.

6.4 Tensor Decomposition Algorithms and the Associated Computational Complexity

In this section, we discuss how to estimate the matrices involved in the proposed PARAFAC model in Section 6.2.1. Various tensor decomposition algorithms proposed in the literature can be employed for estimation of $\mathbf{A}$, $\mathbf{B}$ and $\mathbf{C}$ matrices of the proposed PARAFAC model. The examples include alternating least squares (ALS), gradient descent algorithm, conjugate gradient algorithm, and the Levenberg-Marquardt algorithm. For a description of these algorithms in the context of PARAFAC, please refer to [18].

6.4.1 PARAFAC Decomposition Using Alternating Least Squares Algorithm

ALS is one of the most popular algorithms for PARAFAC, which we briefly describe here in the context of SC-FDMA CFO estimation.

Given the three equivalent forms of PARAFAC model in (119), (121), and (122), $\mathbf{A}$, $\mathbf{B}$ and $\mathbf{C}$ matrices can be estimated by minimizing either of the following cost functions

$$J^Q = \|\mathbf{Y}^Q - (\mathbf{B} \odot \mathbf{A})\mathbf{C}^T\|^2,$$
$$J^{M_u} = \|\mathbf{Y}^{M_u} - (\mathbf{A} \odot \mathbf{C})\mathbf{B}^T\|^2,$$
$$J^R = \|\mathbf{Y}^R - (\mathbf{C} \odot \mathbf{B})\mathbf{A}^T\|^2.$$

The idea of ALS is to iteratively solve these three cost function, and update one of the three matrices while keeping the other two constant. Thus, for iteration i, given $\hat{\mathbf{A}}^{(i-1)}$ and $\hat{\mathbf{B}}^{(i-1)}$, $\hat{\mathbf{C}}^i$ is calculated as the LS solution of J^Q given as

$$\hat{\mathbf{C}}^{(i)} = \left(\left(\hat{\mathbf{B}}^{(i-1)} \odot \hat{\mathbf{A}}^{(i-1)}\right)^{\dagger} \mathbf{Y}^Q\right)^T. \tag{130}$$

Similarly, $\hat{\mathbf{A}}^{(i)}$ and $\hat{\mathbf{B}}^{(i)}$ are then updated as

$$\hat{\mathbf{B}}^{(i)} = \left(\left(\hat{\mathbf{A}}^{(i-1)} \odot \hat{\mathbf{C}}^{(i)}\right)^{\dagger} \mathbf{Y}^{M_u}\right)^T, \tag{131}$$

and

$$\hat{\mathbf{A}}^{(i)} = \left(\left(\hat{\mathbf{C}}^{(i)} \odot \hat{\mathbf{B}}^{(i)}\right)^{\dagger} \mathbf{Y}^R\right)^T, \tag{132}$$

respectively, and the algorithm moves on to next iteration. The initial values, i.e., $\hat{\mathbf{A}}^{(0)}$ and $\hat{\mathbf{B}}^{(0)}$ required for starting the algorithm are computed by setting the CFO of each user to zero, i.e., $f_m = 0\ \forall m$ in (116) and (120), respectively. The effect of number of iterations on the convergence of the algorithm will be shown through simulation results in Section 6.5.

6.4.2 Computational Complexity of PARAFAC Decomposition

The computational complexity of ALS is dominated by the pseudo-inverse calculations required in (130), (131), and (132) for each iteration. Thus, the computational complexity is given by $O\left(N_i\left((QM_u + N + QR)(M^2 + M) + NQM\right)\right)$ operations [18], where N_i is the number of iterations of ALS. As a comparison, the complexity of data-aided ML CFO estimation in [61] is $O(MN_cN_i(P^3 + PN^2))$ where N_c is the number of candidate CFO values used in the line search, which is significantly higher than the proposed algorithm. On the other hand, the complexity of blind ESPRIT-based CFO estimation in [37] is $O(M_u^3 + M_u^2N)$, which is about the same complexity order as the proposed algorithm. However, the performance of the proposed algorithm is significantly better than [37] as shown in Section 6.5.

6.5 Simulation Results

In this section, we evaluate the performance of the proposed algorithms through Monte Carlo simulations and compare it with some of the existing schemes in the literature. For CFO estimation, we compare with the algorithms in [12, 37, 61], and for CFO compensation, we compare with the CFO compensation scheme in [11]. The simulation parameters are as follows: total number of sub-carriers $N = 128$, length of CP $N_g = 16$, maximum number of users $M_u = 8$, active users $M = 4$, number of sub-carrier allocated to each user $R = \frac{N}{8} = 16$, and the channel length for each user $P_m = 6$. For each iteration of the simulation, the CFO of each user is modeled as a random variable uniformly distributed between $[-f_{\max}, f_{\max}]$ with $f_{\max} = 0.4$. The modulation scheme is QPSK. The transmission is modeled in the form of frames, where each frame contains Q identical training symbols in the beginning followed by 20 SC-FDMA symbols carrying data. CFO and channel estimation is carried out using the training symbols, and the estimates are employed to decode all the data symbols in that frame. For comparison, Q symbols are also employed for CFO

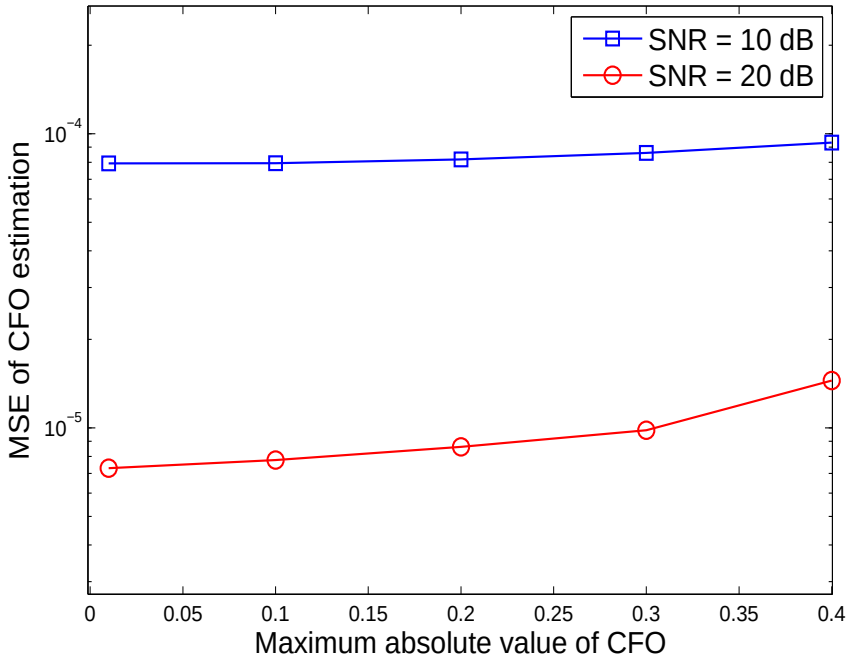

Figure 38: Effect of increasing value of CFO on proposed CFO estimation.

estimation using [12, 37, 61].

6.5.1 Performance of Proposed CFO Estimation

CFO Estimation Performance with Increasing value of CFO Figure 38 shows the performance of the proposed CFO estimation in terms of MSE of CFO estimation with increasing value of $f_{\max}$, i.e., the maximum absolute CFO at an SNR of 20 dB. The rest of the simulation parameters are as given in the beginning of this section. As the maximum CFO increases, ICI and MUI increase, and we expect to see degradation in CFO estimation performance. This trend is visible in Figure 38 for both values of simulated SNR as the MSE of CFO estimation increases slightly as $f_{\max}$ increases. Note that only 5 iterations of ALS algorithms are performed in each case, and the performance for larger values of CFOs can be improved by performing more iterations of ALS algorithm.

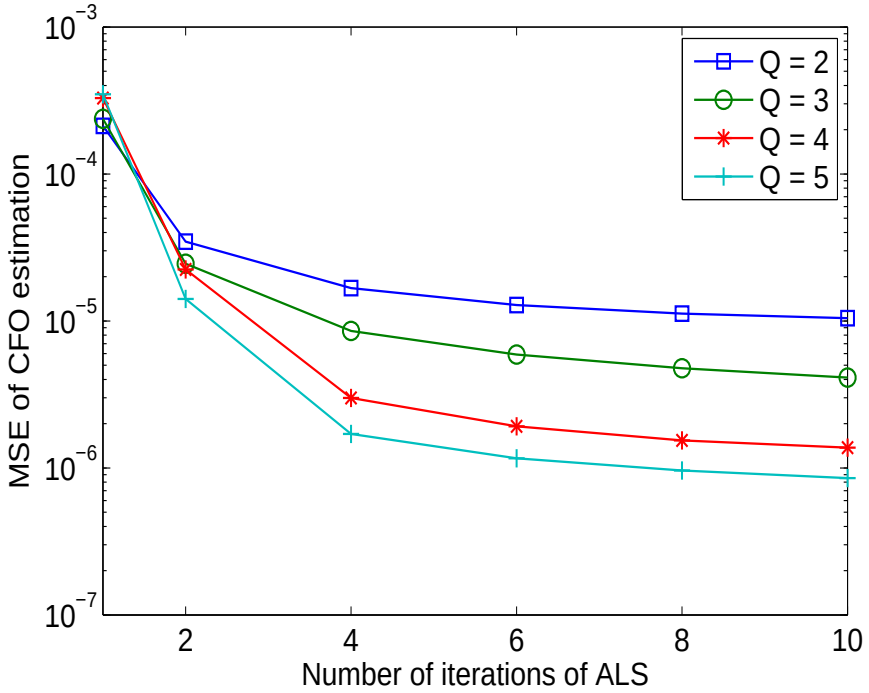

Figure 39: Effect of number of training symbols and iterations of ALS algorithm on proposed CFO estimation.

Effect of Number of Training Symbols on CFO Estimation We now evaluate the effect of number of training symbols Q and the number of iterations of ALS on the MSE of CFO estimation at an SNR of 20 dB. The values of Q range from 2 to 5 and the results are shown in Figure 39. As shown, the MSE of CFO estimation decreases as more training symbols and/or more iterations of ALS are employed for CFO estimation. However, the price for the increase in CFO estimation accuracy is decreased spectral efficiency due to more training symbols and/or increased complexity and latency of CFO estimation due to more iteration of ALS. Thus, there exists a trade-off between CFO estimation performance and spectral efficiency/complexity. Figure 39 also shows that the improvement in performance of CFO estimation is negligible after about $4-6$ iterations of ALS. Thus, in the following simulations, only 5 iterations of ALS are employed.

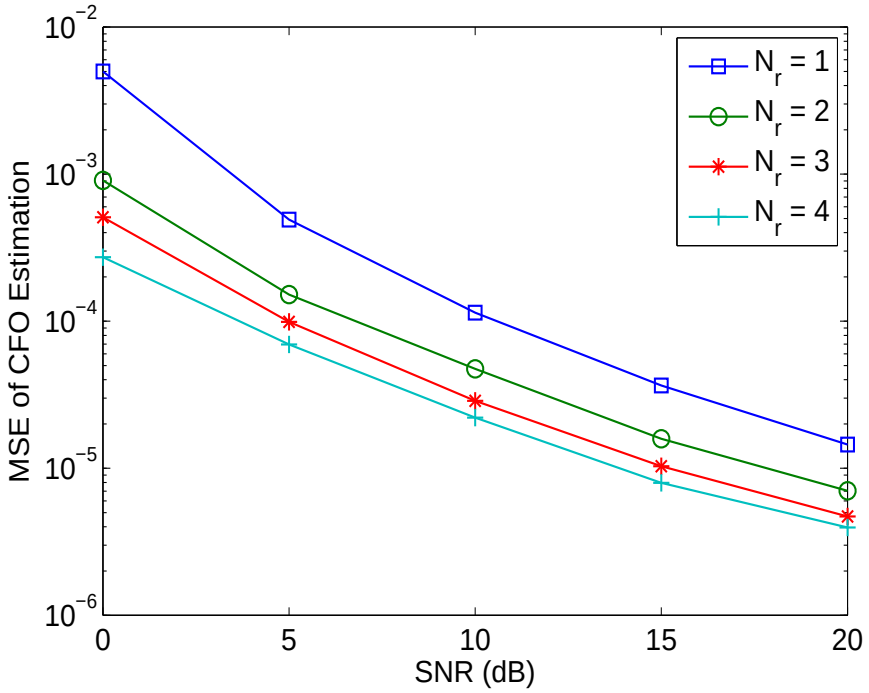

Figure 40: Effect of number of receive antennas on proposed CFO estimation.

CFO estimation performance for multi-antenna BS In this section, we evaluate the performance of the CFO estimation for multi-antenna BS reception. As the CFO remains constant across receiver antennas at the BS, the performance of CFO estimation is expected to improve as more antennas are employed at the BS. This trend is clearly visible in Figure 40, which shows the MSE of CFO estimation for multi-antenna BS reception. As number of receive antennas N_r is increased from 1 to 4, about 7 dB improvement in performance is observed.

6.5.2 Performance Comparison with Existing Algorithms

CFO Estimation In this section, we compare the performance of the proposed CFO estimation for single-antenna BS case with the schemes in [12,37,61] denoted as 'MUSIC' and 'ESPRIT', and 'APFE', respectively. Same number of symbols $Q = 2$ are employed for CFO estimation in all schemes although both schemes in [12, 37] are truly blind schemes and do not require knowledge of the training symbols. The

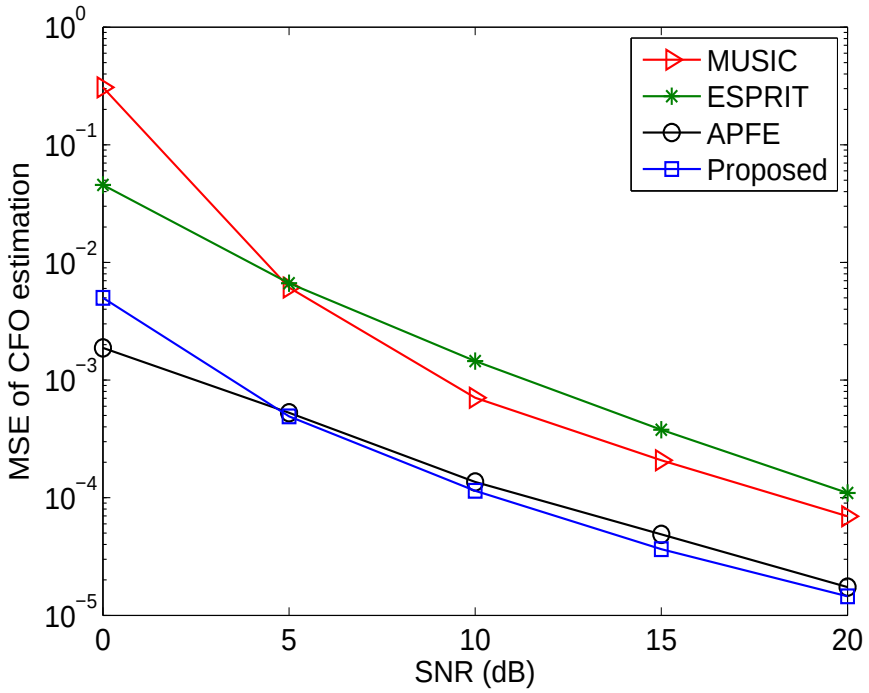

Figure 41: Comparison of proposed CFO estimation with existing schemes.

proposed scheme is semi-blind as discussed in Section 6.2 because it does not require the knowledge of the training symbols and only requires that the $Q = 2$ training symbols are identical. The scheme in [61] is data-aided and requires the knowledge of all training symbols. The number of candidate CFO values employed in the line search used in MUSIC and APFE is 1000. The comparison, given in Figure 41, shows that the performance of the proposed scheme is significantly better ($8 - 10$ dB improvement) than the MUSIC and ESPRIT schemes. The performance of ESPRIT is better than MUSIC for lower SNR while the opposite is true for higher SNR. As both MUSIC and ESPRIT are blind CFO estimation algorithms, CFO estimation accuracy can be increased by employing data symbols for CFO estimation. However, it will increase the complexity and latency of CFO estimation. Compared to APFE, the proposed algorithm offers about 1 dB performance improvement for SNR > 5 dB. However, it should be noted that the complexity of the proposed algorithm is significantly less than APFE as discussed in Section 6.4. The complexity of CFO

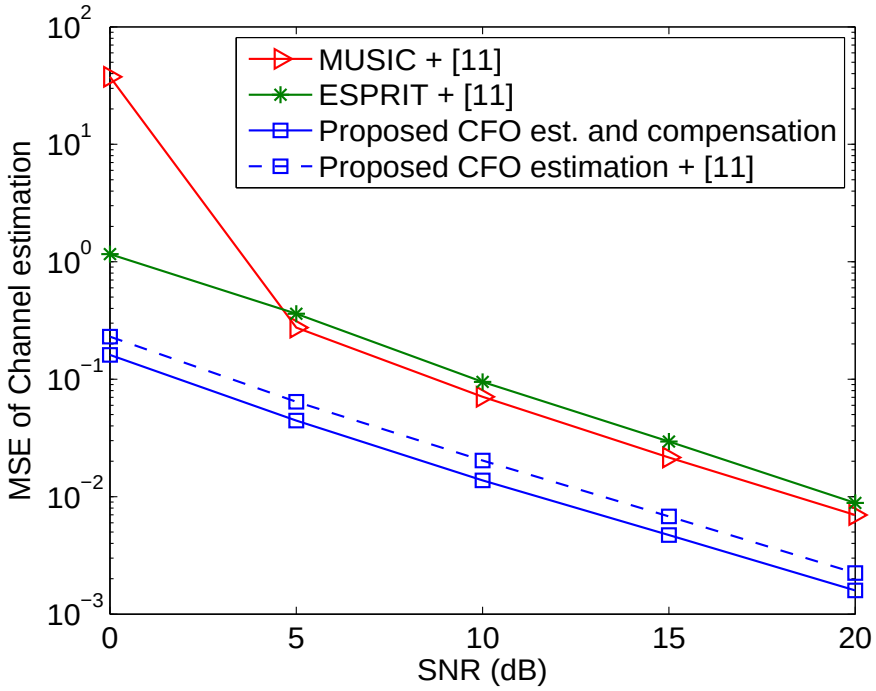

Figure 42: Comparison of proposed CFO compensation with existing schemes.

estimation in [61] can be lowered by using sub-optimal algorithms at the cost of degradation of CFO estimation accuracy.

CFO compensation and Channel Estimation We now compare the performance of the proposed CFO compensation algorithm with the one proposed in [11]. The performance is evaluated in terms of MSE of channel estimation performed after CFO compensation. LS channel estimation [56] is employed in each case. A better CFO compensation scheme will result in less residual ICI and MUI, which will improve the channel estimation accuracy. We compare the performance of the proposed CFO estimation and compensation with three different combinations of CFO estimation and compensation. CFO estimation algorithms in [12, 37], combined with the CFO compensation in [11] are denoted as 'MUSIC + [11]' and 'ESPRIT + [11]'. As the CFO estimation accuracy for MUSIC and ESPRIT in worse than the proposed algorithm as shown in the previous section, we also evaluate the performance of CFO

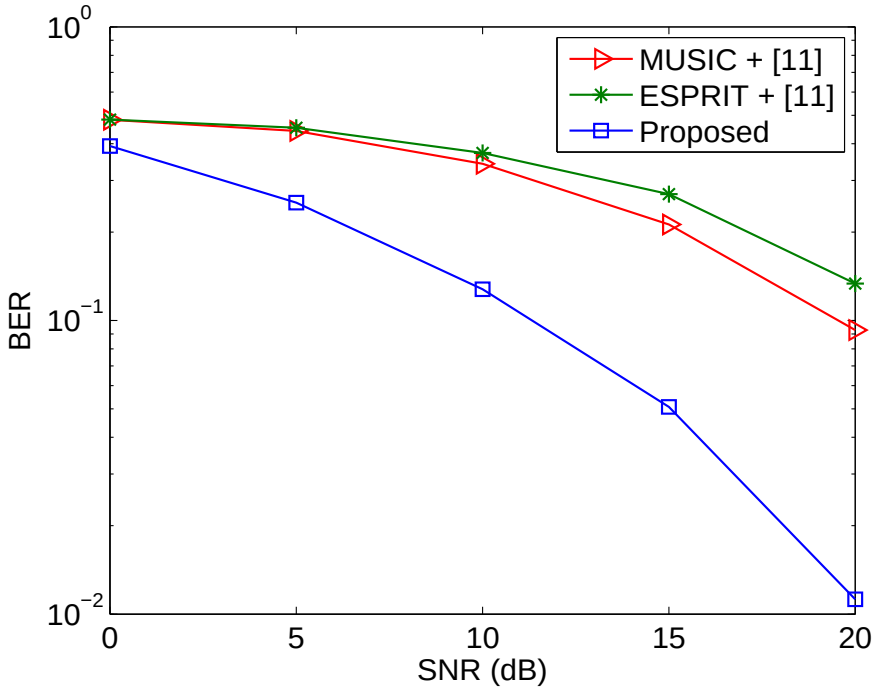

Figure 43: BER comparison of the proposed CFO estimation and compensation methods with existing schemes.

compensation in [11] combined with the proposed CFO estimation scheme for fair comparison of the proposed and [11]-based CFO compensation schemes. Fig. 42 shows the MSE for channel estimation for all scenarios. As shown, the performance of 'MUSIC + [11]' and 'ESPRIT + [11]' is worse than the proposed schemes. Moreover, the performance of the proposed CFO estimation and compensation is better (about 2 dB improvement in performance) than the proposed CFO estimation combined with [11], which shows that the proposed CFO compensation schemes does a better job of extracting the interference-free received signal.

Bit Error Rate Performance Fig. 43 shows the BER performance of the proposed CFO estimation and compensation algorithms and their comparison with CFO estimation schemes in [12, 37] combined with CFO compensation scheme in [11]. It is clear from the figure that the proposed CFO estimation and compensation schemes outperform both MUSIC and ESPRIT based CFO estimation combined with CFO

compensation in [11], which shows the effectiveness of the proposed schemes. These simulation results show that the proposed CFO estimation and compensation schemes offer significant performance improvements in both CFO estimation accuracy and estimation of MUI-free received signals corresponding to different users.

CHAPTER VII

CONCLUDING REMARKS

In this dissertation, we have presented timing and frequency synchronization schemes for OFDM-based transmissions. We have shown that OFDM transmissions are sensitive to synchronization impairments while DL and UL transmissions have different synchronization requirements and challenges. Multiple CFOs generated by multiple BSs in cooperative DL transmissions or multiple MUs in UL transmissions generate IBI or MUI in addition to the ICI. These interferences violate the orthogonality of OFDM sub-carriers and degrade system performance. Thus, the objective of the proposed research was to design, analyze, and implement synchronization techniques for DL and UL OFDM transmissions. The main contributions of this dissertation are summarized below:

- We proposed a training-assisted coarse TO and CFO estimation method for DL OFDM transmissions. The training block, consisting of two suitably chosen ZC sequences, provides robustness to CFOs and allows coarse TO estimate to reside within the ISI-free region. We presented the criterion to select the root indices of the ZC sequences. We also presented a training block detection test and its approximation to alleviate the dependency on the multi-path channel profile and the CFO. The proposed synchronization schemes are based on a common cross-correlation-based architecture conducive to hardware implementation. Moreover, the proposed detection and synchronization schemes offer better performance than the existing schemes in the literature.

- We proposed a training-assisted CFO estimation algorithm for DL CoMP transmissions employing ZC sequences. We presented the design procedure for proposed training signals, which enable decoupling of BSs' signals resulting in a low-complexity CFO estimation scheme. Comparisons with the existing approaches in the literature revealed that the proposed algorithm offers lower complexity and better performance.

- We presented a null sub-carrier-based CFO estimation technique for OFDMA UL systems employing either SSAS or GSAS. In the proposed scheme, CFO of each user is estimated by observing the amount of interference at the predefined null sub-carrier positions. We investigated the identifiability of the CFO estimation under the effect of MUI. In addition, we discussed the effect of null sub-carrier position and MUI on the acquisition range of the CFO estimation. We proved that the identifiability of CFO estimation is guaranteed for the supported CFO acquisition range. We also proposed pilot-based residual CFO estimation for further enhancement of CFO estimation performance. Simulation results demonstrated the superior performance of the proposed algorithm as compared to existing schemes in the literature.

- We presented CFO estimation and compensation algorithms for SC-FDMA UL transmissions with ISAS. The proposed algorithms are based on PARAFAC analysis and guarantee the identifiability of CFO estimation. Moreover, the proposed scheme allows the system to operate on full load gaining better spectral efficiency. Comparisons with the existing schemes in the literature demonstrate that the proposed algorithms have lower complexity and offer considerable performance improvements for both CFO estimation and compensation in SC-FDMA UL receivers.

- We developed a hardware test-bed for real-time implementation of CoMP transmissions. The physical layer parameters of the OFDM-based CoMP transmissions are based on the LTE standard. This implementation allows us to obtain real-time measurements results for co-channel interference scenarios in cellular systems and evaluate the performance of the proposed algorithms in real-world conditions.

7.1 Future Research Topics

Synchronization is the first and foremost task of any communication receiver and reliable synchronization is one of the major requirement of any communications network. As wireless communications standards continue to evolve, new and challenging network topologies and transmissions scenario emerge, which require efficient and reliable synchronization with low-complexity, low-latency, and low-overhead. This dissertation has dealt with some of these challenging scenarios and requirements. However, following research directions can be explored based on the research work described in this dissertation.

- We have presented the analysis on sensitivity of ZC sequences to CFOs. Based on the analysis, we have designed robust synchronization schemes for DL OFDM transmissions. We have also exploited this sensitivity to design CFO estimation schemes for DL CoMP transmissions. However, the extension of the analysis to UL transmissions will be an interesting research direction. Apart from synchronization, identifying MUs in UL transmissions is also an important requirement. As the ZC sequences are circularly uncorrelated, and ZC sequences with different root-indices have low cross-correlation, user separation in UL transmissions can be carried out in two ways. Different MUs can transmit same ZC sequence with different circular shifts or ZC sequences with different root-indices. The analysis on sensitivity of ZC sequences to CFOs can be employed to identify

the values of root-indices and circular shifts, which enable MU de-coupling in addition to CFO robustness.

- Current research trends for fifth generation (5G) of cellular networks imply that 5G networks will be heterogeneous in nature consisting of a macro-cell operating in existing 4G spectrum with an abundance of small-cells operating in the millimeter-wave (mm-wave) frequency band. The effect of oscillator instabilities at mm-wave $(30 - 300$ GHz) band will further aggravate the problem of frequency synchronization due to amplified CFOs and phase noise. In addition, increased attenuation of radio waves at mm-wave frequencies will require beam-forming. BS discovery in mm-wave band, hand-offs from macro-cell to small-cells operating in different frequency bands, and cooperation between small-cells; all these scenarios require synchronization between different small-cells and macro-cells and design of reliable synchronization schemes with as small over-head as possible, is an interesting research direction to pursue.

- We have developed a test-bed for OFDM-based transmissions. As the test-bed in based on NI's hardware and software solutions, anyone interested in prototyping using NI tools can use the basic building blocks implemented during the test-bed development. We have a point-to-point OFDM link implementation, which can be used as the starting point for further development. Furthermore, we have developed the hardware architecture for synchronization among different transmit chains in CoMP transmissions. This hardware architecture can be further extended to heterogeneous network prototyping to realize different transmissions scenarios identified above and perform real-time performance evaluations.

APPENDIX A

PROOF OF PROPOSITION 1

$l_2 = l_1 + (l_1 - N_g - d)$ satisfies the claim as

$$\begin{aligned} u(l_2 - N_g - d) + 2 &= u(l_1 + (l_1 - N_g - d) - N_g - d) + 2 \\ &= 2u(l_1 - N_g - d) + 2 = 2m_1 N = m_2 N. \end{aligned}$$

Similarly,

$$\begin{aligned} u(l_{i+1} - N_g - d) + i + 1 &= u(l_i + (l_1 - N_g - d) - N_g - d) + i + 1 \\ &= u(l_i - N_g - d) + i + m_1 N \\ &= u(l_{i-1} - N_g - d) + i - 1 + 2m_1 N \\ &\vdots \\ &= u(l_1 - N_g - d) + 1 + im_1 N = (i+1)m_1 N. \blacksquare \end{aligned}$$

APPENDIX B

PROOF OF PROPOSITION 2

Assume that there exists an index l_{i1} such that,

$$u(l_{i1} - N_g - d) + i = m_{i1}N,$$

for some integer m_{i1} while l_{i1} lies in $\mathcal{R}_{\text{cc}}$, i.e., $d \leq l_{i1} \leq d + 2N_g$, and $N_g < \frac{N}{2}$, which is usually the case. Now assume that there exists another l_{i2} such that

$$u(l_{i2} - N_g - d) + i = m_{i2}N$$

for the same i, but some integer $m_{i2} \neq m_{i1}$. Then,

$$u(l_{i2} - l_{i1}) = (m_{i2} - m_{i1})N$$

or

$$\frac{u}{N} = \frac{m_{i2} - m_{i1}}{l_{i2} - l_{i1}}.$$

As u is relatively prime to N, the minimum possible value of $(l_{i2} - l_{i1})$ is $\pm N$ or $l_{i2} = l_{i1} \pm N$. Therefore, both l_{i2} and l_{i2} cannot lie in $\mathcal{R}_{\text{cc}}$ at the same time while outside $\mathcal{R}_{\text{cc}}$, the linear correlation is no longer equal to the circular correlation. Hence, the indices in $\mathcal{R}_{\text{CIR}}$ are unique.■

APPENDIX C

PROOF OF PROPOSITION 3

As the ZC sequence is periodic with N, it is unique only for $-(N-1) \leq u \leq N-1$. Let us define $s = l - d - N_{\mathrm{g}}$. If $(us + f_b)_N \approx 0$, then $((-u)(-s) + f_b)_N \approx 0$, which implies that the leakage region for $-u$ is at same distance s from CIR region but in opposite direction. Thus, we only consider $1 \leq u \leq N-1$. As $\Psi(\cdot)$ in (64) is periodic with N, a sample close to the center of a main lobe is obtained when

$$(us + f_b)_N \approx 0. \tag{133}$$

As $|f_b| < 0.5$ and $\gcd(u, N) = 1$, the condition is satisfied for $s = 0$, which corresponds to the CIR region, as $N_{\mathrm{g}} < N$.

Theorem: u is relatively prime to N ($\gcd(u, N) = 1$) if and only if there exists an integer s such that $(us)_N = 1$.

Proof: See theorem 3.4.4 [6, p. 56].

The first side lobe of $\Psi(us + f_b)$ is sampled when $(us + f_b)_N \approx 1$ implying that a leakage region is obtained at $l = (d + N_{\mathrm{g}} + s)_N$ for a root index u. As $|f_b| < 0.5$, s is the value, which satisfies $(us)_N = 1$. Moreover, if $(us + f_b)_N \approx 1$, then $(uts + f_b)_N \approx t$ where t is an integer, implying that the t^{th} side lobe is sampled, and the t^{th} leakage region is obtained at $l = (d + N_{\mathrm{g}} + ts)_N$ for the root index u. However t is only unique from $t = 1, \ldots, |u| - 1$ as value of $t \geq u$, say $u+1$ implies $(uts)_N = (u\{(u+1)s\})_N \approx 1$, which is same as the first leakage region. Hence, a root index $\pm u$ provides $t = |u| - 1$ root indices. ■

APPENDIX D

PROOF OF PROPOSITION 4

For the worst case interference scenario discussed in Section 5.3.2, $f_m - f_o = \pm(2f_{\max} - \frac{1}{2})$ and $f_o = f_{m'}$. Note that the normalized MUI in (100) can be written as

$$\mathcal{J}_{m',\mathrm{MUI}}(f_o) = \frac{1}{N^2} \sum_{m=0}^{M_{\max}-1} \sum_{r=0, r\neq n_k}^{N_s-1} \frac{1-\cos\left(2\pi\{f_m - f_o + N_s\Delta m + \Delta r\}\right)}{1-\cos\left(\frac{2\pi}{N}\{f_m - f_o + N_s\Delta m + \Delta r\}\right)}. \tag{134}$$

We represent the normalized MUI and SI, by Taylor series about their extreme points denoted by a_m where, $a_{m'} = 2\pi\left(f_{m'} - f_o + \Delta r\right)|_{f_o = f_{m'}} = 2\pi\Delta r$ for the SI term. For the MUI term, $a_m = 2\pi\left(r - \frac{1}{2} + N_s\Delta m\right)$, when $n_k < \frac{N_s}{2}$ and $f_{\max} = \frac{n_k}{2}$. Similarly $a_m = 2\pi\left(N_s(\Delta m - 1) + \frac{3}{2} + r\right)$, for $n_k \geq \frac{N_s}{2}$.

Representing the normalized MUI in (134) through Taylor series at $x = a_m$ gives,

$$\begin{aligned}
\mathcal{J}_{m',\mathrm{MUI}}(f_o) = \frac{1}{N^2} \sum_{m=0, m\neq m'}^{M_{\max}-1} \sum_{r=0, r\neq n_k}^{N_s-1} & \frac{1-\cos(a_m)}{1-\cos(\frac{a_m}{N})} + \frac{(x-a_m)}{1-\cos(\frac{a_m}{N})}\sin(a_m) \\
& - \frac{(x-a_m)}{1-\cos(\frac{a_m}{N})}\frac{1}{N}\frac{\sin(\frac{a_m}{N})(1-\cos(\frac{a_m}{N}))}{(1-\cos(\frac{a_m}{N}))} + \frac{(x-a_m)^2}{1-\cos(\frac{a_m}{N})}\frac{\cos(a_m)}{2!} \\
& - \frac{(x-a_m)^2}{1-\cos(\frac{a_m}{N})}\left(\frac{1}{N^2}\frac{1-\cos(a_m)}{1-\cos(\frac{a_m}{N})}\left[\frac{\cos(\frac{a_m}{N})}{2!} - \frac{\sin^2(\frac{a_m}{N})}{1-\cos(\frac{a_m}{N})}\right]\right) \\
& - \frac{(x-a_m)^2}{1-\cos(\frac{a_m}{N})}\frac{1}{N}\frac{\sin(a_m)\sin(\frac{a_m}{N})}{(1-\cos(\frac{a_m}{N}))} + O\left((x-a_m)^3\right),
\end{aligned}$$

where $x = 2\pi\left(f_m - f_o + N_s\Delta m + \Delta r\right)$. We then evaluate the second derivative of the worst case MUI at $x = a_m$ which becomes,

$$\begin{aligned}
\frac{\partial^2 \mathcal{J}_{m',\mathrm{MUI}}(f_o)}{\partial f_o^2} = \frac{8\pi^2}{N^2} \sum_{m=0, m\neq m'}^{M_{\max}-1} \sum_{r=0, r\neq n_k}^{N_s-1} & \frac{\cos(a_m)}{2\left(1-\cos(\frac{a_m}{N})\right)} - \frac{1}{N^2}\frac{1-\cos(a_m)}{\left(1-\cos(\frac{a_m}{N})\right)^2} \\
& \times \left(\frac{\cos(\frac{a_m}{N})}{2} - \frac{\sin^2(\frac{a_m}{N})}{1-\cos(\frac{a_m}{N})}\right) - \frac{1}{N}\frac{\sin(a_m)\sin(\frac{a_m}{N})}{\left(1-\cos(\frac{a_m}{N})\right)^2},
\end{aligned}$$

and reduces to,

$$\frac{\partial^2 \mathcal{J}_{m',\mathrm{MUI}}(f_o)}{\partial f_o^2} = \frac{8\pi^2}{N^2} \sum_{m=0,m\neq m'}^{M_{\max}-1} \sum_{r=0,r\neq n_k}^{N_s-1} -\frac{1}{2\left(1-\cos(\frac{a_m}{N})\right)} + \frac{1}{N^2}\frac{1}{\left(1-\cos(\frac{a_m}{N})\right)^2} \times \left(2+\cos(\frac{a_m}{N})\right). \tag{135}$$

Similarly the second derivative of the SI term is calculated through Taylor series about its extreme point or minimum, i.e., $a_{m'}$. The curvatures of the worst case normalized MUI and SI are given by absolute value of their second derivatives at their respective extreme points. Thus,

$$\kappa_{\mathcal{J}_{m',\mathrm{MUI}}(f_o)} = \left|\frac{\partial^2 \mathcal{J}_{m',\mathrm{MUI}}(f_o)}{\partial f_o^2}\right| < \frac{4\pi^2}{N^2} \sum_{m=0,m\neq m'}^{M_{\max}-1} \sum_{r=0,r\neq n_k}^{N_s-1} -\frac{1}{1-\cos(\frac{a_m}{N})},$$

which for $n_k < \frac{N_s}{2}$ becomes

$$\frac{2\pi^2}{N^2} \sum_{m=0,m\neq m'}^{M_{\max}-1} \sum_{r=0,r\neq k}^{N_s-1} \csc^2\left(\frac{2\pi(r-\frac{1}{2}+N_s\Delta m)}{N}\right) < \frac{2\pi^2}{N^2} \sum_{r'=N_s}^{MN_s-1} \csc^2\left(\frac{2\pi(r'-\frac{1}{2})}{N}\right).$$

As

$$\sum_{n=0}^{N-1} \csc^2\left(\frac{\pi n}{N}+z\right) = N^2\csc^2(Nz),$$

$$\kappa_{\mathcal{J}_{m',\mathrm{MUI}}(f_o)} = \frac{2\pi^2}{N^2}\left(N^2\csc^2\left(\frac{-\pi}{2}\right) - \sum_{r'=0}^{N_s-1}\csc^2\left(\frac{2\pi r'-\pi}{2N}\right)\right) < 4,$$

for $N_s > 2$. Here we use the fact that $\csc(x) \approx \frac{1}{x}$ for small x. Similar result is obtained for $n_k \geq \frac{N_s}{2}$. On the other hand, the curvature of the SI at its minimum becomes,

$$\begin{aligned}\kappa_{\mathcal{J}_{m',\mathrm{SI}}(f_o)} &= \frac{4\pi^2}{N^2} \sum_{r=0,r\neq n_k}^{N_s-1} \frac{1}{1-\cos(\frac{2\pi(\Delta r)}{N})} \\ &= \frac{2\pi^2}{N^2} \sum_{r=0,r\neq n_k}^{N_s-1} \csc^2\left(\frac{2\pi\,(r-n_k)}{2N}\right) \geq 4,\end{aligned}$$

for $N_s > 2$. Hence it is proved that the curvature of MUI term is always less than the curvature of SI term, at the minimum of the cost function and thus, the identifiability of CFO estimation is always guaranteed.■

REFERENCES

[1] "IEEE standard for information technology–Telecommunications and information exchange between systems local and metropolitan area networks–Specific requirements Part 11: Wireless LAN medium access control (MAC) and physical layer (PHY) specifications," *IEEE Std 802.11-2012*, pp. 1–2793, Mar. 2012.

[2] "IEEE Standard for Local and Metropolitan Area Networks Part 16: Air Interface for Fixed and Mobile Broadband Wireless Access Systems Amendment 2: Physical and Medium Access Control Layers for Combined Fixed and Mobile Operation in Licensed Bands and Corrigendum 1," *IEEE Std 802.16e-2005 and IEEE Std 802.16-2004/Cor 1-2005 (Amendment and Corrigendum to IEEE Std 802.16-2004)*, pp. 1–822, Feb. 2006.

[3] Abdzadeh-Ziabari, H. and Shayesteh, M., "A novel preamble-based frame timing estimator for OFDM systems," *IEEE Communications Letters*, vol. 16, pp. 1121–1124, May 2012.

[4] Ahmed, S., Lambotharan, S., Jakobsson, A., and Chambers, J., "MIMO frequency-selective channels with multiple-frequency offsets: estimation and detection techniques," *IEE Proceedings-Communications*, vol. 152, pp. 489–494, Aug. 2005.

[5] Al-Kamali, F. S., Dessouky, M., Sallam, B., Shawki, F., Al-Hanafy, W., and El-Samie, F., "Joint low-complexity equalization and carrier frequency offsets compensation scheme for MIMO SC-FDMA systems," *IEEE Transcations on Wireless Communications*, vol. 11, pp. 869–873, Mar. 2012.

[6] Ash, R. B., *A primer of abstract mathematics*. Mathematical Association of America, 1998.

[7] Barbarossa, S., Pompili, M., and Giannakis, G., "Channel-independent synchronization of orthogonal frequency division multiple access systems," *IEEE Journal on Selected Areas in Communications*, vol. 20, no. 2, pp. 474–486, Feb. 2002.

[8] Besson, O. and Stoica, P., "On parameter estimation of MIMO flat-fading channels with frequency offsets," *IEEE Transactions on Signal Processing*, vol. 51, pp. 602–613, Feb. 2003.

[9] Bladsjo, D., Hogan, M., and Ruffini, S., "Synchronization aspects in LTE small cells," *IEEE Communications Magazine*, vol. 51, pp. 70–77, Sept. 2013.

[10] Bolcskei, H., "Blind estimation of symbol timing and carrier frequency offset in wireless OFDM systems," *IEEE Transactions on Wireless Communications*, vol. 49, pp. 988–999, June 2001.

[11] Cao, Z., Tureli, U., and Yao, Y.-D., "Low-complexity orthogonal spectral signal construction for generalized OFDMA uplink with frequency synchronization errors," *IEEE Transactions on Vehicular Technology*, vol. 56, pp. 1143–1154, May 2007.

[12] Cao, Z., Tureli, U., and Yao, Y., "Deterministic multiuser carrier-frequency offset estimation for interleaved OFDMA uplink," *IEEE Transactions on Communications*, vol. 52, no. 9, pp. 1585–1594, Sept. 2004.

[13] Chang, A.-C. and Yang, S.-H., "An iterative MVDR CFO estimation for interleaved OFDMA uplink systems," in *Computing, Communications and IT Applications Conference (ComComAp)*, pp. 153–158, Apr. 2013.

[14] "3rd generation partnership project (3GPP); Technical specification group radio access network; Evolved universal terrestrial radio access (E-UTRA); User equipment (UE) radio transmission and reception (Release 10)," *3GPP TR 36.101, V7.1.0*, Mar. 2012.

[15] Chen, J., Wu, Y.-C., Chan, S., and Ng, T.-S., "Joint maximum-likelihood CFO and channel estimation for OFDMA uplink using importance sampling," *IEEE Transactions on Vehicular Technology*, vol. 57, no. 6, pp. 3462–3470, Mar. 2008.

[16] Chu, D., "Polyphase codes with good periodic correlation properties," *IEEE Transactions on Information Theory*, vol. 18, pp. 531–532, July 1972.

[17] Classen, F. and Meyr, H., "Frequency synchronization algorithms for OFDM systems suitable for communication over frequency selective fading channels," in *IEEE* 44^{th} *Vehicular Technology Conference*, pp. 1090–3038, June 1994.

[18] Comon, P., Luciani, X., and De Almeida, A. L., "Tensor decompositions, alternating least squares and other tales," *Journal of Chemometrics*, vol. 23, pp. 393–405, Apr. 2009.

[19] Coulson, A., "Maximum likelihood synchronization for OFDM using a pilot symbol: algorithms," *IEEE Journal on Selected Areas in Communications*, vol. 19, pp. 2486–2494, Dec. 2001.

[20] D'Andrea, A., Mengali, U., and Reggiannini, R., "The modified Cramer-Rao bound and its application to synchronization problems," *IEEE Transcations on Communications*, vol. 42, pp. 1391–1399, Feb. 1994.

[21] Eisinberg, A. and Fedele, G., "On the inversion of the vandermonde matrix," *Applied mathematics and computation*, vol. 174, pp. 1384–1397, Mar. 2006.

[22] Gul, M., Lee, S., and Ma, X., "Carrier frequency offset estimation for OFDMA uplink using null sub-carriers," *Digital Signal Processing*, vol. 29, pp. 127–137, June 2014.

[23] Gul, M., Lee, S., and Ma, X., "Developing a SIMO-OFDM link using National Instruments' LabVIEW and lead user platform," *Georgia Tech Research Report*, pp. 1–29, latest version published on Mar. 2014.

[24] Gul, M., Lee, S., and Ma, X., "Timing and frequency synchronization for OFDM downlink transmissions using Zadoff-Chu sequences," *IEEE Transactions on Wireless Communications*, submitted Oct. 2013, revised Apr. 2014.

[25] Gul, M. and Ma, X., "Synchronization for CoMP transmissions with multiple carrier frequency offsets," *IEEE Globecom*, submitted Apr. 2014.

[26] Gul, M., Ma, X., and Lee, S., "PARAFAC-based frequency synchronization for SC-FDMA uplink transmissions," *EURASIP Journal on Advances in Signal Processing*, submitted Apr. 2014.

[27] Gul, M., Lee, S., and Ma, X., "Robust synchronization for OFDM employing Zadoff-Chu sequence," in *Proc.* 46^{th} *Annual Conference on Information Sciences and Systems (CISS)*, (Princeton, NJ), pp. 1–6, Mar. 2012.

[28] Hsieh, H.-T. and Wu, W. R., "Blind maximum-likelihood carrier-frequency-offset estimation for interleaved OFDMA uplink systems," *IEEE Transactions on Vehicular Technology*, vol. 60, pp. 160–173, Jan. 2011.

[29] Huang, D. and Letaief, K., "An interference-cancellation scheme for carrier frequency offsets correction in OFDMA systems," *IEEE Transactions on Communications*, vol. 53, pp. 1155–1165, July 2005.

[30] "Guidelines for evaluation of radio transmission technologies for IMT-2000," *ITU Recommendations M.1225*, 1997.

[31] Jiang, T. and Sidiropoulos, N., "A direct blind receiver for SIMO and MIMO OFDM systems subject to unknown frequency offset and multipath," in 4^{th} *IEEE Workshop on Signal Processing Advances in Wireless Communications*, pp. 358–362, Jun. 2003.

[32] Kas, M., Yargicoglu, B., Korpeoglu, I., and Karasan, E., "A survey on scheduling in IEEE 802.16 mesh mode," *IEEE Communications Surveys and Tutorials*, vol. 12, pp. 205–221, 2^{nd} quarter 2010.

[33] Kay, S., *Fundamentals of statistical signal processing, Volume II: Detection theory*. Upper Saddle River (New Jersey), 1998.

[34] Kotzsch, V. and Fettweis, G., "On synchronization requirements and performance limitations for CoMP systems in large cells," in *Proc.* 8^{th} *International Workshop on Multi-Carrier Systems Solutions (MC-SS)*, (Herrsching, Germany), pp. 1–5, May 2011.

[35] Kruskal, J. B., "Rank, decomposition, and uniqueness for 3-way and n-way arrays," *Multiway data analysis, North-Holland, Amsterdam*, vol. 33, pp. 7–18, 1989.

[36] Larson, R. and Edwards, B., *Calculus*. Brooks/Cole Pub. Co., 9^{th} ed., 2009.

[37] Lee, J., Lee, S., Bang, K., Cha, S., and Hong, D., "Carrier frequency offset estimation using ESPRIT for interleaved OFDMA uplink systems," *IEEE Transactions on Vehicular Technology*, vol. 56, pp. 3227–3231, Sept. 2007.

[38] Lee, S. and Ma, X., "Timing adjustment techniques to mitigate interference between multiple nodes in OFDMA mesh networks," in *Proc. IEEE International Conference on Acoustics, Speech and Signal Processing (ICASSP)*, pp. 3508–3511, May 2011.

[39] Liang, Y.-J., Stuber, G., Chang, J.-F., and Yang, D.-N., "A joint channel and frequency offset estimator for the downlink of coordinated MIMO-OFDM systems," *IEEE Transactions on Wireless Communications*, vol. 11, pp. 2254–2265, May 2012.

[40] "3rd Generation Partnership Project (3GPP); Technical Specification Group Radio Access Network; Physical layer aspects for evolved Universal Terrestrial Radio Access (UTRA) (Release 7)," *3GPP TR 25.814, V7.1.0*, Sept. 2006.

[41] "3^{rd} generation partnership project (3GPP); Technical specification group radio access network; Coordinated Multi-Point Operation for LTE; Physical layer aspects (Release 11)," *3GPP TR 36.819, V1.1.0*, Aug. 2011.

[42] Luise, M., Marselli, M., and Reggiannini, R., "Low-complexity blind carrier frequency recovery for OFDM signals over frequency-selective radio channels," *IEEE Transactions on Communications*, vol. 50, pp. 1182–1188, Nov. 2002.

[43] Ma, X., Tepedelenlioğlu, C., Giannakis, G., and Barbarossa, S., "Non-data-aided carrier offset estimators for OFDM with null subcarriers: identifiability, algorithms, and performance," *IEEE Journal on Selected Areas in Communications*, vol. 19, no. 12, pp. 2504–2515, Dec. 2001.

[44] Ma, X., Giannakis, G., and Barbarossa, S., "Non-data-aided frequency-offset and channel estimation in OFDM and related block transmissions," in *Proc. IEEE International Conference on Communications*, vol. 6, (Helsinki, Finland), pp. 1866–1870 vol.6, 2001.

[45] Ma, X., Oh, M.-K., Giannakis, G., and Park, D.-J., "Hopping pilots for estimation of frequency-offset and multiantenna channels in MIMO-OFDM," *IEEE Transactions on Communications*, vol. 53, pp. 162–172, Jan. 2005.

[46] Manolakis, K., Gutierrez Estevez, D., Jungnickel, V., Xu, W., and Drewes, C., "A closed concept for synchronization and cell search in 3GPP LTE systems," in *Proc. IEEE Wireless Communications and Networking Conference*, pp. 1–6, Apr. 2009.

[47] Marabissi, D., Fantacci, R., and Papini, S., "Robust multiuser interference cancellation for OFDM systems with frequency offset," *IEEE Transactions on Wireless Communications*, vol. 5, pp. 3068–3076, Nov. 2006.

[48] Marsch, P. and Fettweis, G. P., *Coordinated multi-point in mobile communications: from theory to practice*. Cambridge University Press, 2011.

[49] Minn, H., Bhargava, V., and Letaief, K., "A robust timing and frequency synchronization for OFDM systems," *IEEE Transactions on Wireless Communications*, vol. 2, pp. 822–839, July 2003.

[50] Moose, P. H., "A technique for orthogonal frequency division multiplexing frequency offset correction," *IEEE Transactions on Communications*, vol. 42, pp. 2908–2914, Oct. 1994.

[51] Morelli, M., Kuo, C., and Pun, M., "Synchronization techniques for orthogonal frequency division multiple access (OFDMA): A tutorial review," *Proceedings of the IEEE*, vol. 95, no. 7, pp. 1394–1427, July 2007.

[52] Morelli, M. and Mengali, U., "An improved frequency offset estimator for OFDM applications," in *Proc. Communication Theory Mini-Conference*, (Vancouver, BC), pp. 106–109, June 1999.

[53] Myung, H., Lim, J., and Goodman, D., "Peak-to-average power ratio of single carrier fdma signals with pulse shaping," in *IEEE 17th International Symposium on Personal, Indoor and Mobile Radio Communications, 2006*, pp. 1–5, Sept. 2006.

[54] Myung, H. G., Lim, J., and Goodman, D. J., "Single carrier FDMA for uplink wireless transmission," *IEEE Vehicular Technology Magazine*, vol. 1, pp. 30–38, Sept. 2006.

[55] Nion, D. and De Lathauwer, L., "An enhanced line search scheme for complex-valued tensor decompositions. Application in DS-CDMA," *Signal Processing*, vol. 88, pp. 749–755, Mar. 2008.

[56] Ozdemir, M. and Arslan, H., "Channel estimation for wireless OFDM systems," *IEEE Communications Surveys and Tutorials*, vol. 9, no. 2, pp. 18–48, 2007.

[57] Park, B., Cheon, H., Kang, C., and Hong, D., "A novel timing estimation method for OFDM systems," *IEEE Communications Letters*, vol. 7, pp. 239–241, May 2003.

[58] Park, B., Cheon, H., Ko, E., Kang, C., and Hong, D., "A blind OFDM synchronization algorithm based on cyclic correlation," *IEEE Signal Processing Letters*, vol. 11, pp. 83–85, Jan. 2004.

[59] Popovic, B., "Efficient DFT of Zadoff-Chu sequences," *Electronics Letters*, vol. 46, pp. 502–503, Apr. 2010.

[60] Prasad, R., *OFDM for wireless communications systems*. Artech House, 2004.

[61] Pun, M.-O., Morelli, M., and Kuo, C.-C., "Maximum-likelihood synchronization and channel estimation for OFDMA uplink transmissions," *IEEE Transcations on Communications*, vol. 54, pp. 726–736, Apr. 2006.

[62] Reimers, U., "DVB-T: the COFDM-based system for terrestrial television," *Electronics Communication Engineering Journal*, vol. 9, pp. 28–32, Feb. 1997.

[63] Ren, G., Chang, Y., Zhang, H., and Zhang, H., "Synchronization method based on a new constant envelop preamble for OFDM systems," *IEEE Transactions on Broadcasting*, vol. 51, pp. 139–143, Mar. 2005.

[64] Ross, S., *Introduction to probability models*. Academic press, 10^{th} ed., 2009.

[65] Sanguinetti, L. and Morelli, M., "A low-complexity scheme for frequency estimation in uplink OFDMA systems," *IEEE Transactions on Wireless Communications*, vol. 9, pp. 2430–2437, Aug. 2010.

[66] Sayed, A., *Fundamentals of adaptive filtering*. Wiley-IEEE Press, 2003.

[67] Schmidl, T. and Cox, D., "Robust frequency and timing synchronization for OFDM," *IEEE Transactions on Communications*, vol. 45, pp. 1613–1621, Dec. 1997.

[68] Shafik, R. A., Rahman, S., and Islam, R., "On the extended relationships among EVM, BER and SNR as performance metrics," in *International Conference on Electrical and Computer Engineering*, pp. 408–411, Dec. 2006.

[69] Shi, K. and Serpedin, E., "Coarse frame and carrier synchronization of OFDM systems: A new metric and comparison," *IEEE Transactions on Wireless Communications*, vol. 3, pp. 1271–1284, July 2004.

[70] Sidiropoulos, N., Bro, R., and Giannakis, G., "Parallel factor analysis in sensor array processing," *IEEE Transactions on Signal Processing*, vol. 48, pp. 2377–2388, Aug. 2000.

[71] Sidiropoulos, N., Giannakis, G., and Bro, R., "Blind PARAFAC receivers for DS-CDMA systems," *IEEE Transcations on Signal Processing*, vol. 48, pp. 810–823, Mar. 2000.

[72] Speth, M., Fechtel, S., Fock, G., and Meyr, H., "Optimum receiver design for wireless broad-band systems using OFDM. I," *IEEE Transactions on Wireless Communications*, vol. 47, pp. 1668–1677, Nov. 1999.

[73] Speth, M., Fechtel, S., Fock, G., and Meyr, H., "Optimum receiver design for OFDM-based broadband transmission. II. A case study," *IEEE Transactions on Communications*, vol. 49, no. 4, pp. 571–578, Apr. 2001.

[74] Sun, P. and Zhang, L., "Low complexity pilot aided frequency synchronization for OFDMA uplink transmission," *IEEE Transactions on Wireless Communications*, vol. 8, pp. 3758–3769, July 2009.

[75] Tsai, Y.-R., Huang, H.-Y., Chen, Y.-C., and Yang, K.-J., "Simultaneous multiple carrier frequency offsets estimation for coordinated multi-point transmission in OFDM systems," *IEEE Transactions on Wireless Communications*, vol. 12, pp. 4558–4568, Sept. 2013.

[76] Tufvesson, F., Edfors, O., and Faulkner, M., "Time and frequency synchronization for OFDM using PN-sequence preambles," in *Proc. IEEE* 50^{th} *Vehicular Technology Conference*, vol. 4, pp. 2203–2207, Sept. 1999.

[77] Tureli, U., Liu, H., and Zoltowski, M., "OFDM blind carrier offset estimation: ESPRIT," *IEEE Transactions on Communications*, vol. 48, pp. 1459–1461, Sept. 2000.

[78] Valcarce, R. and Mosquera, C., "Maximum likelihood SNR estimation for asynchronously oversampled OFDM signals," in *Proc. IEEE* 9^{th} *Workshop on Signal Processing Advances in Wireless Communications*, (Recife, Brazil), pp. 26–30, July 2008.

[79] van de Beek, J.-J., Sandell, M., and Börjesson, P., "ML estimation of time and frequency offset in OFDM systems," *IEEE Transactions on Signal Processing*, vol. 45, pp. 1800–1805, July 1997.

[80] van de Beek, J., Börjesson, P., Boucheret, M., Landström, D., Arenas, J., Odling, P., Ostberg, C., Wahlqvist, M., and Wilson, S., "A time and frequency synchronization scheme for multiuser OFDM," *IEEE Journal on Selected Areas in Communications*, vol. 17, no. 11, pp. 1900–1914, Nov. 1999.

[81] Wang, C. and Wang, H., "On joint fine time adjustment and channel estimation for OFDM systems," *IEEE Transactions on Wireless Communications*, vol. 8, pp. 4940–4944, Oct. 2009.

[82] Wang, C.-L. and Wang, H.-C., "Optimized joint fine timing synchronization and channel estimation for MIMO systems," *IEEE Transactions on Communications*, vol. 59, pp. 1089–1098, Apr. 2011.

[83] Wang, H. and Yin, Q., "Multiuser carrier frequency offsets estimation for OFDMA uplink with generalized carrier assignment scheme," *IEEE Transactions on Wireless Communications*, vol. 8, no. 7, pp. 3347–3353, July 2009.

[84] Wang, Z., Xin, Y., and Mathew, G., "Iterative carrier-frequency offset estimation for generalized OFDMA uplink transmission," *IEEE Transactions on Wireless Communications*, vol. 8, pp. 1373–1383, Mar. 2009.

[85] Wang, Z. and Giannakis, G., "Wireless multicarrier communications," *IEEE Signal Processing Magazine*, vol. 17, pp. 29–48, May 2000.

[86] "Developing a SISO-OFDM Link Using National Instruments' LabVIEW and Lead User Platform," *National Instruments*, pp. 1–29, latest version published on Mar. 2014.

[87] Yang, B., Letaief, K., Cheng, R., and Cao, Z., "Timing recovery for OFDM transmission," *IEEE Journal on Selected Areas in Communications*, vol. 18, pp. 2278–2291, Nov. 2000.

[88] Yao, Y. and Giannakis, G., "Blind carrier frequency offset estimation in SISO, MIMO, and multiuser OFDM systems," *IEEE Transactions on Communications*, vol. 53, no. 1, pp. 173–183, Feb. 2005.

[89] Yucek, T. and Arslan, H., "Carrier frequency offset compensation with successive cancellation in uplink OFDMA systems," *IEEE Transactions on Wireless Communications*, vol. 6, pp. 3546–3551, Oct. 2007.

[90] Zarikoff, B. and Cavers, J., "Multiple frequency offset estimation for the downlink of coordinated MIMO systems," *IEEE Journal on Selected Areas in Communications*, vol. 26, pp. 901–912, Aug. 2008.

[91] Zarikoff, B. and Cavers, J., "Coordinated multi-cell systems: Carrier frequency offset estimation and correction," *IEEE Journal on Selected Areas in Communications*, vol. 28, no. 9, pp. 1490–1501, 2010.

[92] Zhang, W., Gao, F., Yin, Q., and Nallanathan, A., "Blind carrier frequency offset estimation for interleaved OFDMA uplink," *IEEE Transcations on Signal Processing*, vol. 60, pp. 3616–3627, Jul. 2012.

[93] Zhu, Y. and Ben Letaief, K., "CFO estimation and compensation in single carrier interleaved FDMA systems," in *IEEE Global Telecommunications Conference*, pp. 1–5, Dec. 2009.

[94] Zhu, Y. and Ben Letaief, K., "CFO estimation and compensation in SC-IFDMA systems," *IEEE Transcations on Wireless Communications*, vol. 9, pp. 3200–3213, Oct. 2010.

VITA

Malik Muhammad Usman Gul received his B.E. and M.S. in electrical engineering from the National University of Sciences and Technology in Pakistan in 2007 and 2009, respectively. From August 2008 to December 2009, he worked as a research engineer in the MIMO Research Group at the IQRA University in Pakistan, where he was involved in the development of a MIMO-OFDM test-bed. He received a Fulbright scholarship for doctoral studies in the U.S. and joined Georgia Tech in 2010, where he is currently working towards his Ph.D. degree. He also spent summer of 2011 and 2012 as a research intern in National Instruments, Austin TX where he was involved in design and implementation of synchronization algorithms for LTE and IEEE 802.11ac WiFi networks. His research interests include the design, analysis, and the implementation of detection, synchronization, and channel estimation algorithms for wireless networks.